Near Field Speckles

Doriano Brogioli

November 4, 2008

Chapter 1

Introduction.

Elastic light scattering (LS) has been extensively used to study samples showing a non uniform refraction index on lengthscales from a fraction of a micrometer to a fraction of a millimeter. Basically, a wide laser beam is sent through the sample, and the light scattered at any angle is measured by a detector in the far field. Many phenomena have been studied with this technique; among them, thermodynamical fluctuations of concentration in solutions, of temperature, of pressure, convective instabilities and turbulence, colloids and colloidal gels, systems showing critical opalescence.

The measure of the intensity of the beams scattered by a target is a well known way for analysing physical properties of a sample, and is used in many fields of physics: examples are X ray diffraction in crystallographic analysis and particle scattering by nuclei in the Rutherford experiment. In these examples, as in light scattering, the intensity of the scattered beams gives informations on the square modulus of the Fourier transform of a quantity of interest of the sample, the so called power spectrum, evaluated in the transferred wavevector. In the case of light scattering, the quantity of interest is the refraction index. Since refraction index shows variations due to concentration, temperature and pressure fluctuations, all these quantities can be investigated using light scattering.

In principle, measuring the intensity of the light scattered at an arbitrary small angle allows to obtain informations on arbitrary long wavelength Fourier components of the sample. In facts, the measurement of the intensity of the scattered light becomes more and more difficult as the scattering angle becomes small, mainly due to the stray light, that is the light scattered by the imperfections of the optical system, which is mainly scattered at small angles. Thus light scattering cannot give informations on the features of a sample, if their associated wavelenght is longer than a given value. On the other hand, image forming techniques, such as Schlieren, dark field, phase contrast microscopy, have no limitations on the size of the features they can observe. The limitation of many image forming techniques is the difficulty to quantitatively relate the observed images to the physical properties, mainly when dealing with three dimensional

samples.

In the present work, we describe three new techniques, which allow to measure the scattering intensities, overcoming the difficulties associated to small angles. The first of these techniques, the hOmoyne Near Field Speckles (ONFS), has been presented very recentely [1]; in the present work, we show new results, obtained with a slightly improved optical setup [2]. The other techniques, the hEterodyne Near Field Speckles (ENFS) and the Schlieren-like Near Field Speckles (SNFS) are improvements based on that. The first has been recently patented by us [3, 4]; the second is presented here for the first time. Moreover, in Chapt. 3, we present for the first time a mathematical derivation of the working formulas for the three techniques.

Basically, the experimental setup consists in a wide laser beam passing through the sample; a lens forms an image of a plane at a given distance from the cell on a CCD sensor. The image, in the near field, shows speckles, since it is formed by the stochastical interference of the light coming from a random sample: the electric field has a gaussian probability distribution. We will show that, under suitable conditions, the correlation function of such a field closely mirrors the correlation function of the investigated sample; moreover, in general, from the correlation function of the speckle field we can calculate the scattered intensity.

The lens that forms the image on the CCD focuses the transmitted beam around a given point. In ONFS, a beam stop is placed in that point, in order to dispose of the transmitted beam; in SNFS a blade stops half transmitted beam, along with one half of the scattered light, like in Schlieren technique; in ENFS no opaque element is introduced in the optical system. In ONFS, the CCD sees the speckles given by the interference of the scattered beams with themselves: ONFS is an homodyne technique . In ENFS and SNFS, the speckle field is heterodyned with the much more intense transmitted beam, that acts as a reference beam: the measured intensity is linear in the speckle electric field. We acquire a set of images, from one of the three techniques, by using a CCD camera, connected to a frame grabber; the images are then elaborated by a PC, to obtain $I(\vec{q})$, the scattered intensity as a function of the transferred wavevector, the same information obtained by LS. For each technique, we developed algorithms which allow to evaluate the scattered intensities, including the corrections for the stray light and for the shot and read noise of the CCD camera. The algorithms are described in Chapt. 5 and 6.

We used ONFS and ENFS to measure the scattered intensity of some colloids, and we compared the results with those made by a state-of-the-art classical Small Angle Light Scattering (SALS) device. The agreement is very good, notwithstanding a much simpler and stable layout. In Chapt. 7 we compare ONFS, ENFS and SALS measurements, and discuss the main sources of errors. Scattering intensities measured with ENFS show a better quality; we used this technique to evaluate the diameter distribution of some known colloids, by using an inversion algorithm based on Mie theory. The results are presented in Chapt. 8; this shows that ENFS is a simple and powerful alternative to SALS, suited for industrial applications like particle sizing. Moreover, SNFS has been used

to evaluate the power spectrum of non-equilibrium fluctuations in a free diffusion process, thus showing that such techniques have interesting applications in fundamental physics; results are shown in Chapt. 9.

Chapter 2

Qualitative description of the technique.

The intensity of the light scattered from a spatially disordered sample has a speckled appearance, the speckles being generated by the random interference of the scattered elementary spherical waves. While the study of the one point intensity time correlations has proven very useful, and it has generated the technique of Intensity Fluctuation Spectroscopy (IFS) [5], the measurement of the two point, equal time, intensity space correlation function, that is the size and the shape of the speckles, does not provide any useful information. Indeed the Van Cittert and Zernike theorem states that the *far field* space correlation function depends only on the intensity distribution of the scattering volume, and in no way depends on the physical properties of the sample.

In this chapter we will present qualitative elements showing that for fluctuations the size of the wavelength of light or larger, in the *near field* we obtain a speckle field, that is, a gaussian field; moreover its statistics is directly related to the scattered intensity distribution. We will derive the working formulas for three tecniques, hOmodyne Near Field Speckles (ONFS), hEterodyne NFS (ENFS) and Schlieren-like NFS (SNFS); analogies with the IFS will be pointed out. Advantages with respect to the more conventional Small Angle Light Scattering (SALS) technique will be discussed.

First of all, we will describe ONFS setup; many considerations hold also for ENFS and SNFS. The experimental set-up is very unorthodox, with respect to a conventional SALS device. It consists of a wide laser beam and of a Charge Coupled Device (CCD) detector positioned so to be flooded with light coming from any scattering direction the system can scatter at.

The Van Cittert and Zernike theorem states that the field correlation function is [6]:

$$C_E(\Delta x, \Delta y) = \langle E(x,y)\, E^*(x+\Delta x, y+\Delta y)\rangle = \int\int I(\xi,\eta) exp\left[i\frac{2\pi}{\lambda z}(\xi\Delta x + \eta\Delta y)\right] d\xi d\eta \quad (2.1)$$

where $E(x,y)$ is the field in the observation plane $x-y$, λ is the wavelength and $I(\xi,\eta)$ is the actual intensity distribution of the source in the plane $\xi-\eta$ at a distance z from the observation plane. The theorem holds for sources consisting of point emitters, like atoms. The intensity correlation function $C_I(\Delta x,\Delta y) = \langle I(x,y)\, I(x+\Delta x, y+\Delta y)\rangle$ is then derived by applying the so called Siegert relation [7]:

$$C_I(\Delta x,\Delta y) = \langle I\rangle^2 + |C_E(\Delta x,\Delta y)|^2 \tag{2.2}$$

Equations (2.1) and (2.2) specify that the intensity correlation function is related to the space Fourier transform of the source. In practice, this implies that a source of size D will generate speckles of size $\frac{\lambda}{D}z$ on a screen positioned at a distance z [7].

We will start introducing simple euristic arguments and crude evaluations for the near field speckles of the scattered light. Let us consider the case of a large beam diameter D, impinging onto a sample of particles of diameter d larger than the wavelength of light: see Figure 2.1(a). Most of the power will be scattered in a forward lobe of angular width $\Theta \approx \frac{\lambda}{d}$. Let us consider a small area S, for example a multi-element sensor array, in the immediate vicinity of the scattering volume: see Figure 2.1(b). Let us assume that we can ignore the transmitted beam: we will take care of this problem later on. Although the sample is illuminated over the entire surface of diameter D, the light falling onto the sensing area will come only from a smaller area of diameter D^* . In fact the brightness of the scattering volume will change as a function of the observation angle in a way that mirrors the scattered intensity distribution. Consequently, for the sensing area, the source region from which light is drawn is a circle with a diameter $D^* = \frac{\lambda}{d}z$, z being the distance of the sensing area from the scattering surface; source regions outside do not contribute appreciably. We say that the near field condition is met if $D^* \ll D$. One can then immediately estimate the size of the speckles $d_{sp} = \frac{\lambda}{D^*}z \approx d$, a remarkable result in many respects! The speckles have the size of the particle diameter, and this value does not depend on the distance z from the sample, provided the near field condition $D^* \ll D$. This has to be compared with far field speckles, whose diameter scales linearly with the distance from the source. Also notice that the actual sample thickness does not matter, provided that the near field condition is met, and that the speckle size does not depend on the light wavelength, an unexpected feature for an interference pattern.

Notice that all the above applies under conditions that are more stringent than the usual "near field" condition [8] for a source of size D , namely $\frac{\lambda z}{D^2} \ll 1$. In the present case the condition is $D^* \ll D$ which implies $\frac{\lambda z}{Dd} \ll 1$.

To put things in a more quantitative way, we will determine the near field intensity correlation by first re-writing the Van Cittert and Zernike theorem in a more appropriate form. We notice that Eq. (2.1) may be rewritten in the

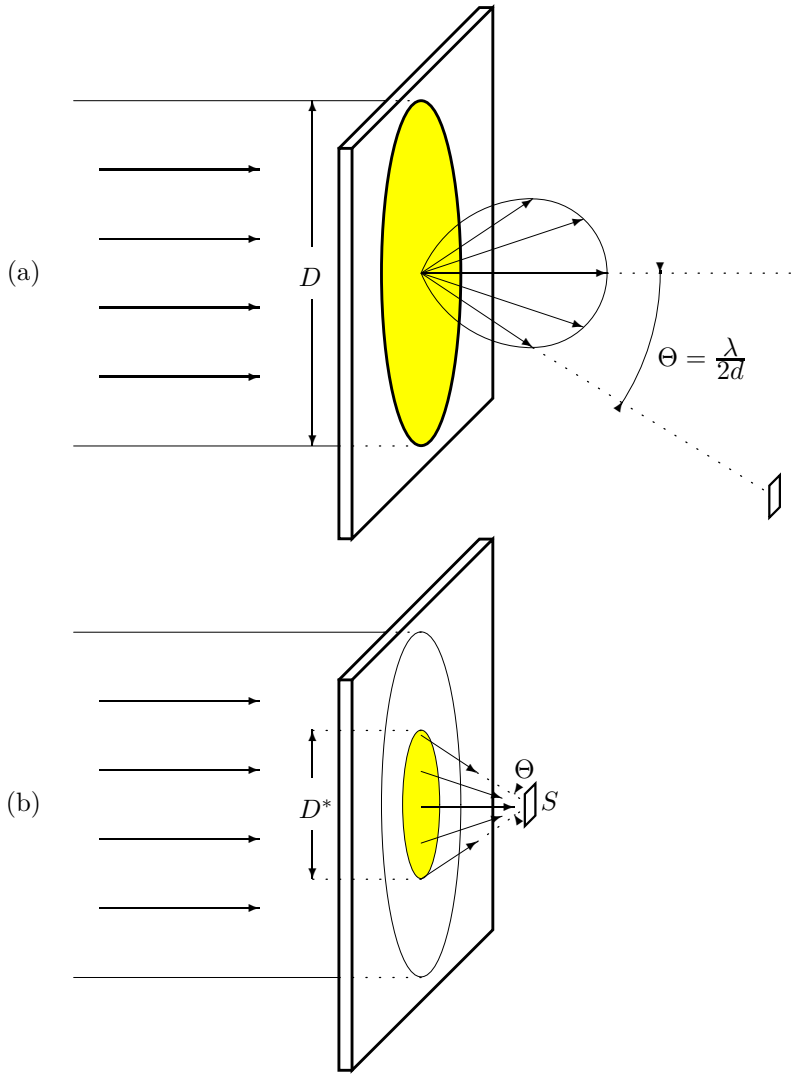

Figure 2.1: (a) Small angle scattering. A beam of diameter D impinges onto a sample composed of particles of diameter d. Any zone within D will scatter light into a lobe of angular width $\Theta = \lambda/d$ (the length of arrows indicates scattered intensity). (b) Same sample, as in part (a). A sensor S close enough to the sample will draw light only from a zone of radius $D^* < D$. Regions outside, even if illuminated by the main beam, do not feed light to S. Notice that again $\Theta = \lambda/d$.

following way:

$$C_E(\vec{r}) = \int I(\vec{q})\, e^{i\vec{q}\cdot\vec{r}} \mathrm{d}\vec{q}, \tag{2.3}$$

where $\vec{r} = (\Delta x, \Delta y)$, and $\vec{q}$ is a vector whose components are $q_x = \frac{2\pi}{\lambda z}\xi$ and $q_y = \frac{2\pi}{\lambda z}\eta$, which equals the scattering wave vector for small scattering angles.

Equation (2.3) is only a different way of writing Eq. (2.1), and $I(\vec{q})$ is the intensity distribution of the source as seen from the observation plane as a function of the scaled angles $(2\pi/\lambda)(\xi/z)$, and $(2\pi/\lambda)(\eta/z)$. As discussed in the introductory remarks, in the very near field $I(\vec{q})$ equals the scattered intensity distribution, which is proportional to the Fourier transform of the sample density correlation function $g(\vec{r}) = \langle \delta l(\vec{r})\, \delta l(0) \rangle$, where δl is the local fluctuation of the particle number density, integrated over the light path. Then, from Eq. (2.2), it follows that:

$$C_I(\vec{r}) = \langle I \rangle^2 \left[1 + |g(\vec{r})|^2 \right]. \tag{2.4}$$

We would like to point out that Eq. (2.4) closely duplicates the well known relation that holds for the IFS $< I(0)I(t) >=< I >^2 [1 + |g(t)|^2]$, where $g(t)$ is the time correlation function (see for example [9]). It should be noted that for some scatterers the Rayleigh Gans approximation is invalid, for example for larger spheres where the Mie theory applies, and therefore the pair correlation function $g(r)$ cannot be extracted from the scattered light. It remains true however that even in those cases the correlation method permits the determination of the scattered intensity distribution $I(q)$, by using the relation:

$$C_I(r) = \langle I \rangle^2 \left[1 + \left| \int I(q)\, e^{i\vec{q}\cdot\vec{r}} \mathrm{d}\vec{q} \right|^2 \right]. \tag{2.5}$$

To determine the spatial intensity correlation of Eq. (2.4), one must first obtain experimentally the instantaneous intensity distribution of the near field scattered light. In order to evaluate the intensity correlation function with reasonable statistical accuracy it is also imperative to gather intensity distributions over a substantial number of points. To this end a CCD is ideal, the number of pixel being larger than 10^5. As we shall see, it actually turns out that one frame is enough for a fair acquisition of the correlation function.

In a previous work [1], some measurements have been performed on a scattering model, an opaque metallic screens with pinholes of 140 and 300 microns chemically etched in random positions. The surface fraction occupied by the pinholes was around 10% and 20% respectively. Experimentally this greatly simplifies the problem, since the scattered field is stationary and also there is no transmitted beam. We call this configuration hOmodyne Near Field Speckles, since the signal is given by the interference of different scattered beams. Being a two dimensional sample, the scattered intensity was simply related to the correlation function of the transparency function $T(x, y)$ with $T = 1$ inside

the pinholes and zero outside [6]. A Helium Neon parallel beam with diameter ($\frac{1}{e^2}$ points) $D = 15$mm was sent onto the samples, and the speckle field was recorded with a CCD at various distances $z = 50$cm, $z = 75$cm and $z = 100$cm [1]. The corresponding values for D^* ranged from 1mm to 4.3mm so that the very near field condition was always met. The rather large dimension of the pinholes was chosen so that the speckles were appreciably larger than the CCD pixel size (typically 9μm). For each type of pinholes, the measurements performed at the three distances showed minute differences. The results are shown in Fig 2.2, where the data are compared with the correlation functions of digitised images of the set of pinholes on the metallic screen [2]. Since in this case the sample is two-dimensional, $g(\vec{r})$ is the correlation function of $T(\vec{x})$. The width and shape of the main peak are fairly well reproduced, in spite of the limited number of frames used (four frames on statistically equivalent samples for each type of pinholes).

While the data obtained with the screens prove that near field speckles do mirror the properties of the scatterers, we feel that to assess the desirability of the technique for realistic applications (for example in colloid physics) measurements had to be taken with particle solutions down in the micron range. In order to do this, three problems had to be solved. The speckles in the near field close to the cell have dimensions around one micron and therefore are too small for the available CCD pixel size. Also, one must dispose of the transmitted beam. Finally, the speckle intensity distribution must be frozen at a given instant.

The first two problems have been solved with the simple optical arrangement shown in Fig. 2.3. A wide parallel beam is sent onto the sample, placed against a large aperture lens of focal length f. A wire is stretched in the focal plane to intercept the main beam. The CCD is placed a distance q away from the lens. The system magnifies the speckle size by a factor $M = (q - f)/f > 1$, and the scattering angles are decreased accordingly. It is illuminating to point out that the technique can be considered as a scaled down version of the classical Hanbury Brown and Twiss [10] experiment where the star intensity distribution is mimicked by the scattered light intensity patch in the focal plane, and the ground based intensity correlation are the CCD intensity correlations. The unavoidable presence of the lens and its finite aperture introduces some complication with respect to the lensless arrangement used for the pinholes. In a previous work [1], the poor numerical aperture of the lens introduced a non-uniform transfer function, which had to be evaluated by measuring a known sample. In the present work, care has been taken in order to avoid such problems.

When the scattered speckles are observed with the CCD in real time, one

[1] For very large objects the near field is not really near, since one must let the diffraction figures from various objects interfere. This leads to the additional condition $D^* = \frac{\lambda}{d} z \gg \delta$, where δ is the typical distance between scatterers.

[2] Experimental correlation functions shown in figure are calculated according to the following procedure. First, the Fast Fourier Transform of the intensity distribution is calculated. Then the result is squared. The auto-correlation is then obtained by anti-transforming the power spectrum.

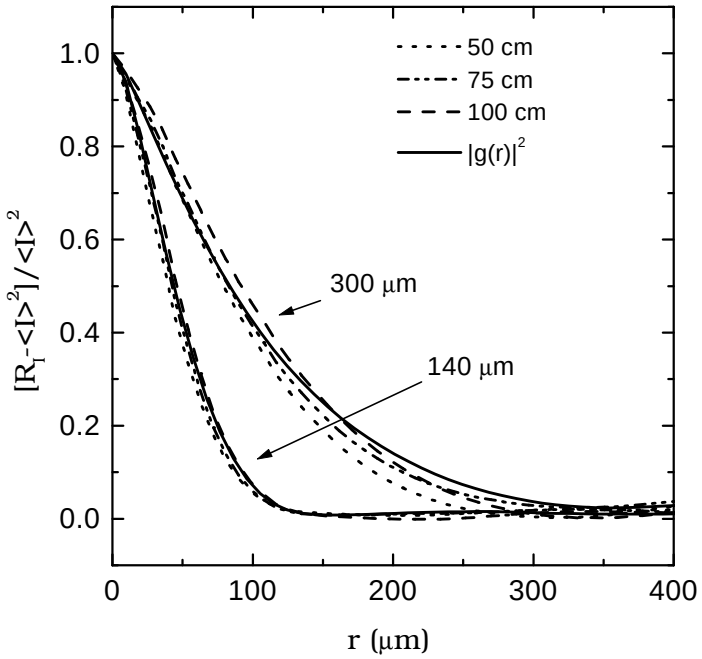

Figure 2.2: Measured intensity auto-correlations as a function of displacement r for two sets of randomly positioned pinholes, of 140μm and 300μm in diameter. For both the samples, measurements at three distances are reported, together with $|g(r)|^2$, calculated from the digitized images of the two samples.

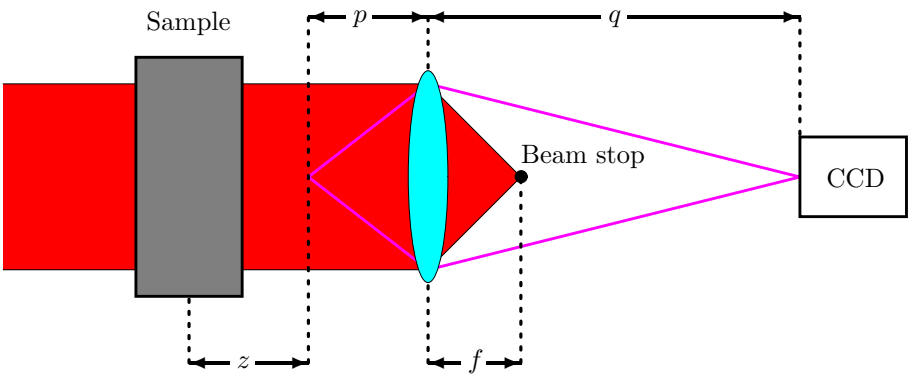

Figure 2.3: Optical layout for ONFS. The main transmitted beam is blocked by a stop in the focal plane. Almost all the scattered light is sent to the CCD.

notices quite vividly that the speckle size changes as the size of the scatterers is changed. Also, for a given sample the speckles boil with the same time constant on the whole screen, the time constant getting larger for samples with larger diameter particles. With regard to the third problem mentioned above, these observations also indicate that even with a conventional CCD and a small power He-Ne laser there is no problem in getting instantaneous pattern distributions. Indeed even for the smallest particles that can be studied with present experimental set-up, with diameters down to 1μm, and assuming diffusive motion, the shortest time constant associated to the smallest scattering wavevector yields $\tau_{min} = 0.125$s, a time long compared with the shortest frame exposure available with standard frame grabbers, typically 1/16000s.

Let us compare the Near Field Speckles technique with the more traditional Small Angle Light Scattering. The essential feature of a scattering layout [11, 12] is that the light scattered at a given angle hits the sensors along a circle of given diameter around the optical axis. We believe that the correlation method of NFS offers some distinct advantages over the scattering technique. First, there is no need for accurate positioning of the CCD, that can be rather casually placed at a distance z from the focal plane (see Fig. 2.3). At variance, in SALS one has to know the precise relation between pixels and scattering angles and this is troublesome when the distance z is changed to select a new particle diameter instrumental range. Also, and more important, SALS is plagued by stray light. To mitigate its effects, one has to rely on blank measurements to be subtracted from raw scattering data. The trouble is that stray light is worst at smaller angles, where the sensing elements are necessarily in small number and crowded close to the optical axis. With the present technique, on the contrary, all the pixels are used in calculating the correlation function for any value of the displacement r and this allows more accurate stray light subtraction; the

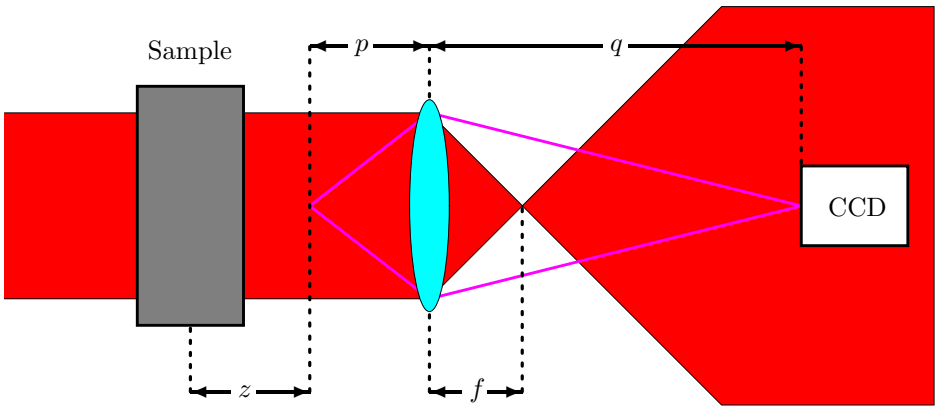

Figure 2.4: Optical layout for ENFS. The main transmitted beam is not blocked by the stop in the focal plane. Both the scattered and the transmitted beams are sent to the CCD.

algorithms to subtract the stray light will be described in Chapter 5.

The results of the measurements on some colloid samples are presented in Chapter 7. The ONFS technique in the present form has only one tight requirement, namely the clean disposal of the transmitted beam that requires accurate focusing and a proper diffraction limited beam stop. It is both conceptually and in practice very simple, and it capitalizes on the high statistical accuracy permitted by the large number of pixels of a CCD and by the good handling capabilities of PCs.

It became soon appearent that the main problem with ONFS comes from the poor statistical quality of the calculated $I(q)$. In Chapter 7 we will show that the statistical quality increases only as the fourth root of the number of processed images. We experimented a different optical setup (ENFS), drawn in Fig. 2.4. In ENFS, there's no beam stop: the main beam is let interfere with the scattered light. This is basically an heterodyne version of NFS, thus we call it hEterodyne Near Field Speckles (ENFS).

Basically, ONFS data processing consists in evaluating the field correlation function $C_E(\vec{r})$ by using Siegert relation (2.2), then evaluating $I(q)$ by applying the inverse Fourier transform to (2.3). In ENFS, we measure the interference between the speckle field of ONFS with the much more intense transmitted beam. We directly measure a quantity linearly related to the field. The intensity correlation function of an ENFS image equals $C_E(\vec{r})$, provided that all the conditions needed by ONFS are met, that is, if the field is circular gaussian. We thus obtain $C_E(\vec{r})$ without the data inversion needed to apply Siegert relation, and this greatly enhances the statistical accuracy of the results.

In Chapter 7 we show a comparison between data taken with ONFS and ENFS; data taken with ENFS are evidently much less noisy. The quality is comparable with the SALS one. This good quality allowed to try a Mie-based

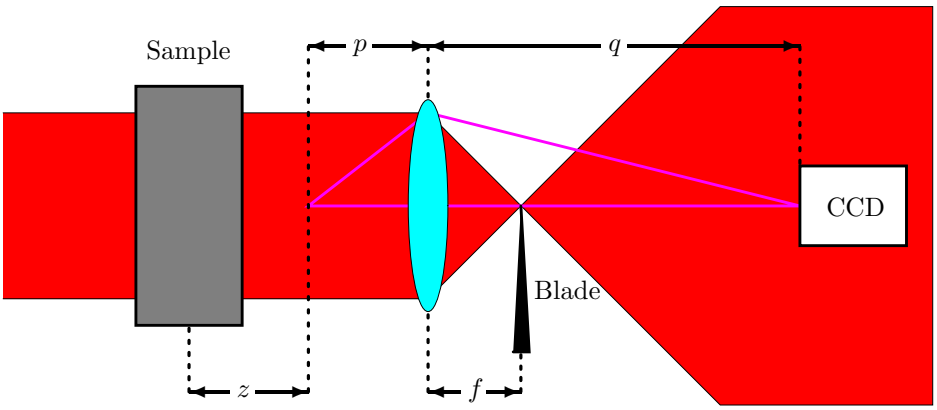

Figure 2.5: Optical layout for SNFS. Part of the transmitted beam is blocked by a blade in the focal plane, along with half of the scattered light. Only one half of the scattered light is sent to the CCD, along with a part of the transmitted beam.

inversion algorithm, to obtain an histogram of the distribution of the diameters of some colloidal samples; the measurements are shown in Chapter 8.

Both ONFS and ENFS are quite sample wasting techniques. They require a sample much bigger than the statistical quality needs. For example, consider a non-equilibrium fluctuation measurement in a free diffusion experiment [13]. The biggest fluctuations we want to measure are about 0.5mm. A good statistical sample should be so big to contain some hundred of the biggest fluctuations: it can be a square with a 5mm side. This is enough for SALS, but not for ONFS nor ENFS. In Chapt. 3 we will show that, if we want to cover two decades in wavevectors, we must use a sample with side $5\text{mm} \cdot 10^2$. To cover two decades, we need a half a meter wide cell, while with SALS we can work with a half a centimeter wide cell! This is not a difficulty for particle sizing applications, but can become a serious problem when we want to analyze many lenghtscales, since NFS is particularly suited for big objects. This problem is essentially due to the fact that big objects need long values of z in order that their scattered field is gaussian; on the other hand, we need a big sample, so that the sensor collect the light scattered at high angles by small particles. This fact is quite unusual, since in general big objects are good subjects for classical microscopy techniques. The difficulty can be easily circumvented, introducing a new instrumental setup, called SNFS: see Fig. 2.5. This setup closely mirrors the Schlieren setup: a blade stops half focused trasmitted beam, along with one half of the scattered light. In the case of a two dimensional sample, we can create an image of it on the CCD sensor, as in classical Schlieren imaging technique. But in the case of three dimensional samples, the smaller objects create a speckle field, while the bigger ones are completely resolved: this technique passes continuously from the deterministic image formation of the big objects,

like in microscopy techniques, to the analysis of stochastical interference patterns of NFS, without the need to know at what lengthscale the passage takes place. We will show that SNFS doesn't require any condition on the position of the focal plane: it can be made as near to the sample as we need; moreover, the dimensions of the sample can be quite small, as in SALS.

SNFS requires an additional element with respect to ENFS, the blade, but it allows easy measurements on many lengthscales, on big objects. We used such a technique to measure the power spectrum of non-equilibrium fluctuations in a free diffusion experiment, described in Chapter 9, thus showing that this technique can be applied to researches in fundamental physics.

Chapter 3

Theory.

In this chapter we describe quantitatively the relations between the scattered intensity and the properties of the field on a given plane. We will derive the transfer function of various techniques based on the light scattering. We will show that, under suitable conditions, the field is gaussian. In this case, we will derive the relation between the power spectra of the NFS images and the scattered intensity.

3.1 Scattered intensity and field power spectrum.

From Maxwell equations, we can derive the wave equation for a transverse component of the electric field in the vacuum [14]:

$$\frac{\partial^2}{\partial t^2} E\left(\vec{x}, z, t\right) = c^2 \left[\frac{\partial^2}{\partial z^2} E\left(\vec{x}, z, t\right) + \nabla_{\vec{x}}^2 E\left(\vec{x}, z, t\right)\right] \tag{3.1}$$

where $\nabla_{\vec{x}}^2$ is the Laplacian oeprator, with respect to the horizontal coordinate $\vec{x}$. Since we are working with a laser, and we consider only elastic scattering, the only temporal frequency involved is kc:

$$E\left(\vec{x}, z, t\right) = E\left(\vec{x}, z\right) e^{-ikct} \tag{3.2}$$

where k is the wave vector. Eq. (3.1) becomes:

$$\frac{\partial^2}{\partial z^2} E\left(\vec{x}, z\right) + \nabla_{\vec{x}}^2 E\left(\vec{x}, z\right) + k^2 E\left(\vec{x}, z\right) = 0 \tag{3.3}$$

We define $E_z\left(\vec{q}\right)$ as the Fourier transform of $E\left(\vec{x}, z\right)$ with respect to $\vec{x}$:

$$\frac{\partial^2}{\partial z^2} E_z\left(\vec{q}\right) = -\left(k^2 - q^2\right) E_z\left(\vec{q}\right) \tag{3.4}$$

The solution is:

$$E_z\left(\vec{q}\right) = E_0\left(\vec{q}\right) e^{i\sqrt{k^2 - q^2}z} \tag{3.5}$$

In order that this solution exists, a condition must be fulfilled:

$$q^2 < k^2, \tag{3.6}$$

This condition is alwais met if we consider only propagating waves.

The quantity $E_z(\vec{q})$ is closely related to the intensity of the light crossing the plane $z = \text{cost}$. Each two-dimensional Fourier mode of amplitude $E_z(\vec{q})$, on a given z, and wavevector $\vec{q}$ is generated by a three-dimensional plane wave of wavevector $[q_x, q_y, k_z]$, where the only value of k_z is obtained by imposing that the wavevector of any plane wave has length k:

$$k_z(q) = \sqrt{k^2 - q^2} \tag{3.7}$$

Given the values of the two-dimensional Fourier modes $E_z(\vec{q})$ on a given $z = 0$, we can evaluate $E(\vec{x}, z)$ for each $\vec{x}$ and z, by using Eq. (3.5) and (3.7). Expressing it by its three-dimensional Fourier transform:

$$E(\vec{q}, k_z) = 2\pi E_0(\vec{q})\,\delta[k_z - k_z(q)] \tag{3.8}$$

Each three-dimensional component with amplitude $E(\vec{q}, k_z)$ of the electric field represents a plane wave travelling in a different direction. We define $S_E(\vec{q}, q_z)$, the two-dimensional power spectrum of $E(\vec{x}, z)$:

$$\langle E_z(\vec{q})\, E_z^*(\vec{q}')\rangle = \delta(\vec{q} - \vec{q}')\, S_E(\vec{q}) \tag{3.9}$$

Light intensity, for each scattering direction, can be defined on the basis of $E(\vec{q}, k_z)$:

$$\langle E(\vec{q}, k_z)\, E^*(\vec{q}', k_z')\rangle = 4\pi^2 \delta(\vec{q} - \vec{q}')\,\delta(k_z - k_z')\,\delta[k_z - k_z(q)]\, I(\vec{q}, q_z) \tag{3.10}$$

where $I(\vec{q}, q_z)$ has been expressed in terms of the transferred wavevector $[q_x, q_y, q_z] = [k_x, k_y, k_z] - [0, 0, k]$. From Eq. (3.7):

$$q_z(\vec{q}) = \sqrt{k^2 - q^2} - k \tag{3.11}$$

Substituting $E(\vec{q}, k_z)$ of Eq. (3.8) in Eq. (3.10), and comparing the result with Eq. (3.9), we can relate the scattered intensity $I(\vec{q}, q_z)$ to the power spectrum of the field $S_E(\vec{q})$:

$$I(\vec{q}, q_z) = S_E(\vec{q}) \tag{3.12}$$

From Eq. (3.12) we notice that $I(q)$ can be measured by evaluating $E_z(\vec{q})$ on any z.

If the sample is isotropic, $I(\vec{q}, q_z)$ depends only on $Q = |q_x, q_y, q_z|$:

$$Q(q) = \sqrt{2}k\sqrt{1 - \sqrt{1 - \left(\frac{q}{k}\right)^2}} \tag{3.13}$$

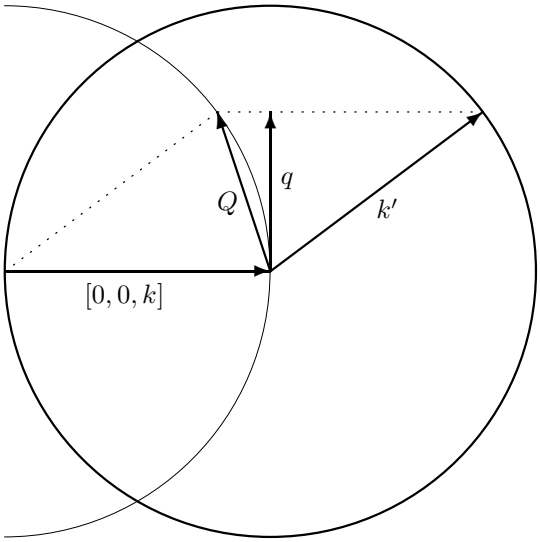

Figure 3.1: Relation between q and Q. Geometrical interpretation of Eq. (3.13)

In this case, Eq. (3.12) can be written in terms on q and Q:

$$I\left[Q\left(q\right)\right] = S_E\left(q\right) \tag{3.14}$$

The geometrical meaning of Eq. (3.13) is explained in Fig. 3.1. For $q \ll k$, Eq. (3.13) can be approximated by $Q\left(q\right) = q$. Moreover, if Rayleigh Gans approximation holds, $I\left(q\right)$ represents the power spectrum of the refraction index of the sample. From these two considerations, we obtain the result that, for scattering on small angles and under Rayleigh Gans condition, the two dimensional correlation function of the electric field is proportional to the correlation function of the light path through the sample.

When performing a far field, small angle scattering measurement, the scattered beams are focused on a screen. In suitable units, each point of the screen has a coordinate q. For small values of the wave vector, q approximates Q', the transferred wavevector. The exact relation is:

$$Q'\left(q\right) = \sqrt{2}k\sqrt{1 - \frac{1}{\sqrt{1 + \left(\frac{q}{k}\right)^2}}} \tag{3.15}$$

Equation (3.13) can be used to correct the results of a Near Field Speckles measurement. Figures 3.1 and 3.2 show the geometrical meaning of equations (3.13) and (3.15). For small values of q, that is $q/k \ll 1$, the two equations can be approximated with $Q = Q' = q$; the error due to this approximation is shown in Fig. 3.3: it's quite small, and it can often be neglected.

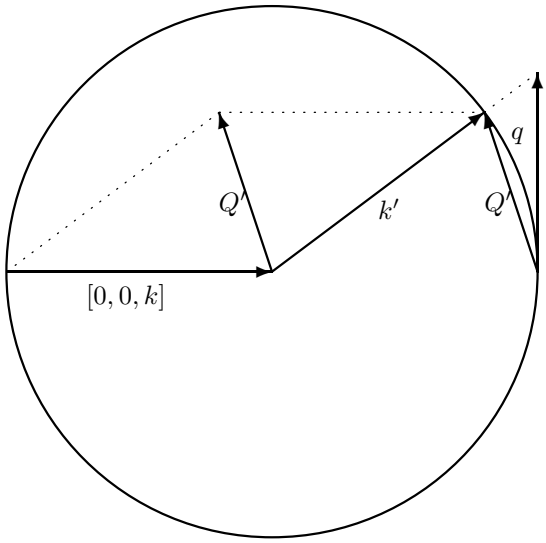

Figure 3.2: Relation between the coordinate q on a screen, in a far field experiment, and the transferred wave vector Q'. Geometrical interpretation of Eq. (3.15)

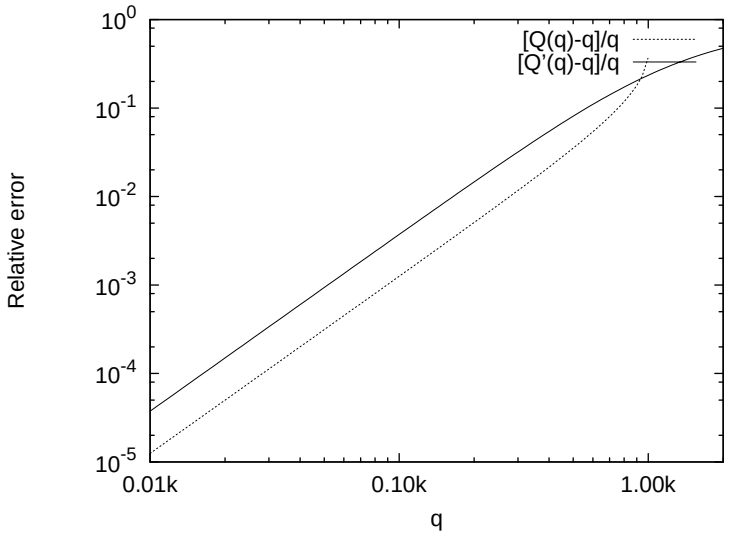

Figure 3.3: Relative error obtained neglecting the non linearity of the ralation between the sample wave vector and the near field wave vector. The graph is obtained from Eqs. (3.13) and (3.15).

3.2 Scattering from a thin sample.

Let us consider a thin sample, with a non homogeneous refraction index, and a light plane wave, moving in the direction of the z axis. For $z = 0$, at the surface of the sample, the field will be:

$$E(\vec{x}, z = 0) = E_0 e^{i\delta l(\vec{x})\, k} \tag{3.16}$$

where $\delta l(\vec{x})$ is the difference between the light path, the integral of the refraction index along z, for a given point $\vec{x}$, and its mean value over the whole sample. If δl is small compared to the light wavelength, we can consider a first order developement:

$$E(\vec{x}, z = 0) = E_0 [1 + i\delta l(\vec{x})\, k] \tag{3.17}$$

Neglecting the higher order terms means that we are neglecting higher order diffracted beams than the first.

Using Eq. (3.5) we can find the field for every value of z:

$$E_z(\vec{x}) = E_0(z) + \delta E_z(\vec{x}) \tag{3.18}$$

where

$$\delta E_z(\vec{q}) = ikE_0(z)\, \delta l(\vec{q})\, e^{i\left(\sqrt{k^2 - q^2} - k\right) z} \tag{3.19}$$

is the scattered field, and

$$E_0(z) = E_0 e^{ikz} \tag{3.20}$$

3.3 Image forming techniques

Microscopy, in its basic form, consists in forming an image of a plane on a device which measures light intensity, such as a photographic film or a CCD sensor. Generally it is used to obtain informations about the intensity of the transmitted light, for example, in the case of an organic tissue, treated by some dye.

If a microscope objective forms the image of a plane on the CCD, the image is given by the interference of the transmitted and the scattered beams. For such an image, the signal can be defined as the difference of the measured intensity $I(\vec{x})$ and the transmitted beam intensity I_0, divided by I_0. We will call this signal $i_{shadowgraph}$, for reasons that will be clear later. We consider the case in which the scattered beams are much less intense than the transmitted one. At the first order in δE, the signal is:

$$i_{shadowgraph}(\vec{x}) = \frac{I(\vec{x}) - I_0}{I_0} = \frac{2}{I_0} \Re [E_0 \delta E^*(\vec{x})] \tag{3.21}$$

and the Fourier transform is:

$$i_{shadowgraph}(\vec{q}) = \frac{1}{I_0} [E_0 \delta E^*(-\vec{q}) + E_0^* \delta E(\vec{q})] \tag{3.22}$$

If the sample is transparent, and we send a plane wave through it, Eq. (3.19) tells us the value of the scattered field:

$$i_{shadowgraph}\left(\vec{q},z\right)=2k\delta l\left(\vec{q}\right)\sin\left[\left(k-\sqrt{k^2-q^2}\right)z\right] \tag{3.23}$$

In order to obtain the previous result, $\delta l\left(\vec{x}\right)$ has been considered real, so that $\delta l^*\left(-\vec{q}\right)=\delta l\left(\vec{q}\right)$.

For $z=0$, that is, if the thin sample is in the focal plane, $i_{shadowgraph}\left(\vec{q},z\right)=0$. The intensity is completely uniform, and bears no informations on the sample.

Many techniques has been developed in order to make phase modulations evident: among them, holography and interferometry. A well known way to make phase modulations evident is the phase contrast microscopy. Basically, this technique consists in changing the phase of the transmitted beam by $\pi/2$. At the first order in δE:

$$i_{phase\,contrast}\left(\vec{x}\right)=\frac{I\left(\vec{x}\right)-I_0}{I_0}=\frac{2}{I_0}\Im\left[E_0^*\delta E\left(\vec{x}\right)\right] \tag{3.24}$$

and the Fourier transform is:

$$i_{phase\,contrast}\left(\vec{q}\right)=\frac{i}{I_0}\left[-E_0^*\delta E\left(-\vec{q}\right)+E_0\delta E^*\left(\vec{q}\right)\right] \tag{3.25}$$

Using Eq. (3.19) to evaluate the scattered field:

$$i_{phase\,contrast}\left(\vec{q},z\right)=2k\delta l\left(\vec{q}\right)\cos\left[\left(k-\sqrt{k^2-q^2}\right)z\right] \tag{3.26}$$

For $z=0$, that is, with the sample in the focal plane:

$$i_{phase\,contrast}\left(\vec{q},z=0\right)=2k\delta l\left(\vec{q}\right) \tag{3.27}$$

Another way to make phase modulations evident is the so called dark field technique. It consists in stopping the transmitted beam. This is accomplished by focusing the transmitted and the scattered beams by a lens, and by removing the transmitted beam by some kind of reflecting or absorbing object. This is an homodyne technique; the signal must be defined as the ratio between the measured intensity $I\left(\vec{x}\right)$ and the intensity of the transmited beam I_0. Since we have only δE:

$$i_{dark\,field}\left(\vec{x}\right)=\frac{I\left(\vec{x}\right)}{I_0}=\frac{\left|\delta E\left(\vec{x}\right)\right|^2}{I_0} \tag{3.28}$$

Equation (3.19), for $z=0$, gives:

$$i_{dark\,field}\left(\vec{x},z=0\right)=k^2\delta l^2\left(\vec{x}\right) \tag{3.29}$$

In Fourier space:

$$i_{dark\,fielf}\left(\vec{q},z=0\right)=\frac{1}{\left(2\pi\right)^2}k^2\int\delta l\left(\vec{q}'\right)\delta l\left(\vec{q}-\vec{q}'\right)\mathrm{d}\vec{q}' \tag{3.30}$$

The Schlieren technique consists in focusing the beams from the sample by a lens; in the focal plane, a blade stops half of the transmitted beam, along with the beams scattered in one half plane. At the first order in δE, the signal is again, like in shadowgraph:

$$i_{Schlieren}\left(\vec{x}\right)=\frac{I\left(\vec{x}\right)-\tilde{I}_0}{\tilde{I}_0}=\frac{2}{\tilde{I}_0}\Re\left[\tilde{E}_0\delta\tilde{E}^*\left(\vec{x}\right)\right] \tag{3.31}$$

where the field $\delta\tilde{E}$ is the scattered field, without one half plane in Fourier space:

$$\delta\tilde{E}\left(\vec{q}\right)=\left\{\begin{array}{ll}\delta E\left(\vec{q}\right) & \vec{q}\cdot\vec{n}<0\\ \delta E\left(\vec{q}\right) & \vec{q}\cdot\vec{n}\geq 0\end{array}\right. , \tag{3.32}$$

$\vec{n}$ is the vector ortogonal to the direction of the blade, $\tilde{I}_0=I_0/2$ and $\tilde{E}_0=E_0/\sqrt{2}$ are the intensity and the field of the trasmitted beam, after the blade. The Fourier transform is:

$$i_{Schlieren}\left(\vec{q}\right)=\frac{\sqrt{2}}{I_0}\left[E_0\delta\tilde{E}^*\left(-\vec{q}\right)+E_0^*\delta\tilde{E}\left(\vec{q}\right)\right] \tag{3.33}$$

Using Eq. (3.32):

$$i_{Schlieren}\left(\vec{q}\right)=\left\{\begin{array}{ll}\frac{\sqrt{2}}{I_0}E_0\delta E^*\left(-\vec{q}\right) & \vec{q}\cdot\vec{n}<0\\ \frac{\sqrt{2}}{I_0}E_0^*\delta E\left(\vec{q}\right) & \vec{q}\cdot\vec{n}\geq 0\end{array}\right. \tag{3.34}$$

Using Eq. (3.19):

$$i_{Schlieren}\left(\vec{q},z\right)=\left\{\begin{array}{ll}\sqrt{2}ik\delta l\left(\vec{q}\right)e^{-i\left(\sqrt{k^2-q^2}-k\right)z} & \vec{q}\cdot\vec{n}<0\\ \sqrt{2}ik\delta l\left(\vec{q}\right)e^{i\left(\sqrt{k^2-q^2}-k\right)z} & \vec{q}\cdot\vec{n}\geq 0\end{array}\right. \tag{3.35}$$

In order to obtain the previous result, $\delta l\left(\vec{x}\right)$ has been considered real, so that $\delta l^*\left(-\vec{q}\right)=\delta l\left(\vec{q}\right)$. For $z=0$, that is, if the thin sample is in the focal plane:

$$i_{Schlieren}\left(\vec{q},z=0\right)=\sqrt{2}ik\delta l\left(\vec{q}\right) \tag{3.36}$$

The factor i means that all the Fourier components of $\delta l\left(\vec{q}\right)$ undergo a rotation of $\pi/2$: a sine-like light path modulation gives a cosine-like intensity modulation.

3.4 Misfocused microscopy and shadowgraph.

Equations (3.23), (3.26) and (3.35) allow to evaluate the evolution of the signals as z, the misfocusing, is increased, for a simple microscope objective, for phase contrast and dark field. It should be noted that we are dealing with images formed by laser light: as z increases, it is possible to recover the original shape of the observed objects; this is completely different from a white light microscope, in which the misfocusing simply smears the images.

Equation (3.30) has not been extended for $z \neq 0$; in all the above mentioned techniques, however, the variation of z strongly influences the relation between the light path $\delta l\left(\vec{q}\right)$ and the signal $i\left(\vec{q}\right)$. This is generally a defect: thick objects, or even thin objects dispersed in a thick volume, are difficult to be analysed. In general, all the above mentioned techniques are applied to samples that are thin, and in the focal plane. No improvement is obtained by misfocusing.

A well known exception is shadograph. Shadowgraph technique consists in sending a plane wave onto a sample, and observing the intensity modulations generated by the sample on a plane placed at a distance z from the sample. Using Eq. (3.23), we can derive the transfer function $T_{shadowgraph}\left(\vec{q},z\right)$ of the shadowgraph technique [15, 16, 17]:

$$T_{shadowgraph}\left(\vec{q},z\right)=2k\sin\left[\left(k-\sqrt{k^2-q^2}\right)z\right]\approx 2k\sin\left(\frac{q^2z}{2k}\right) \tag{3.37}$$

The approximation holds for $q \ll k$. The transfer function is defined as the ratio between the signal and the light path modulation amplitude:

$$i\left(\vec{q},z\right)=T\left(\vec{q},z\right)\delta l\left(\vec{q}\right) \tag{3.38}$$

For $z = 0$, the transfer function vanishes; misfocusing is needed, and is a simple way to make phase modulations evident.

Looking at Eq. (3.26) we can notice that phase contrast transfer function, as a function of z, has a cosinusoidal behaviour:

$$T_{phase\,contrast}\left(\vec{q},z\right)=2k\cos\left[\left(k-\sqrt{k^2-q^2}\right)z\right]\approx 2k\cos\left(\frac{q^2z}{2k}\right) \tag{3.39}$$

When considering opaque objects, with no phase modulations, the transfer functions are exchanged: cosinusoidal for shadowgraph, sinusoidal for phase contrast.

The shadowgraph image is created by the interference between every scattered beam and the transmitted beam; it's always possible, in principle, to find the value of δl, in every point, simply by a deconvolution. Shadowgraph allows the measurement of one component of the field, which, in turns, is the convolution of the light path with a particular function. The absolute intensity modulation of the shadowgraph image is proportional to the mean intensity and to the light path modulation; the constant of proportionality is the the transfer function. The transfer function vanishes for some wave vectors, but has maxima for other ones. At the maxima, the sensibility equals the sensibility of phase contrast and Schlieren techniques.

Now we evaluate the effect of misfocusing on a dark field microscope. We obtain an image of a plane a distance z from the cell. Using Eq. (3.19), we can derive the relation between the light path and the measured intensity, at a given z:

$$i_{dark\,field}\left(\vec{q},z\right)=\frac{1}{\left(2\pi\right)^2}k^2\int\delta l\left(\vec{q}',z\right)\delta l\left(\vec{q}-\vec{q}',z\right)e^{-i\left[\sqrt{k^2-\left(\vec{q}-\vec{q}'\right)^2}-k\right]z}\mathrm{d}\vec{q}' \tag{3.40}$$

This expression reduces to Eq. (3.30) for $z = 0$. At this point, there's no appearent reason to use a misfocused dark field instead of a focused one.

The knowledge of $i_{dark\,field}(\vec{q}, z)$, for every z, can give some informations about the spreading of the scattered light. For the scattering of a single particle, one can measure the intensity on planes with increasing values of z, and calculate how fast the light is diverging. This provides informations both on the position of the particle and on the scattered intensity. For a sample composed by a great number of particles, this cannot be done, and a different, statistical approach must be applied.

For Schlieren technique, from Eq. (3.35):

$$T_{Schlieren}(\vec{q}, z) = \begin{cases} \sqrt{2}ike^{-i\left(\sqrt{k^2-q^2}-k\right)z} & \vec{q}\cdot\vec{n} < 0 \\ \sqrt{2}ike^{i\left(\sqrt{k^2-q^2}-k\right)z} & \vec{q}\cdot\vec{n} \geq 0 \end{cases} \tag{3.41}$$

By evaluating the square modulus of the transfer function, we obtain:

$$\left|T_{Schlieren}(\vec{q}, z)\right|^2 = 2k^2 \tag{3.42}$$

This means that the power spectrum of the electric field is proportional to the power spectrum of the light path, without any dependence on spatial wavelength and misfocusing.

3.5 Scattering measurements by microscopy techniques

By using Eq. (3.12), we can, in principle, evaluate the scattered intensities by measuring the field on a given plane. The above described microscopy techniques allow the determination of some functions of the electric field. Now, we assume that the scattered electric field is generated by a thin sample. From Eq. (3.19), we derive a property of the electric field:

$$\delta E(-\vec{q}) = -\delta E^*(\vec{q})\, e^{2i\left(\sqrt{k^2-q^2}-k\right)z} \tag{3.43}$$

For shadowgraph, we use Eq. (3.22), in order to evaluate the power spectrum S_i of $i(\vec{x})$:

$$S_i(\vec{q}) = \frac{4}{I_0}\sin^2\left[\left(k-\sqrt{k^2-q^2}\right)z\right] S_E(\vec{q}) \tag{3.44}$$

Using Eq. (3.12), we obtain:

$$S_i(q) = \frac{4}{I_0}\sin^2\left[\left(k-\sqrt{k^2-q^2}\right)z\right] I\left[Q(q)\right] \tag{3.45}$$

In order to use shadowgraph to evaluate the scattered intensity, the sample must be out of the focal plane. This technique has some disadvantages: some

wavevectors cannot be seen, since the transfer function vanishes; moreover, if the sample is thick we cannot define a z: the oscillations of the transfer function are smeared, but it could be hard to know quantitatively how much.

For phase contrast, we use Eq. (3.25), in order to evaluate the power spectrum S_i of $i(\vec{x})$:

$$S_i(\vec{q}) = \frac{4}{I_0}\cos^2\left[\left(k - \sqrt{k^2 - q^2}\right)z\right] S_E(\vec{q}) \tag{3.46}$$

Using Eq. (3.12), we obtain:

$$S_i(q) = \frac{4}{I_0}\cos^2\left[\left(k - \sqrt{k^2 - q^2}\right)z\right] I(Q(q)) \tag{3.47}$$

The disadvantages of shadowgraph, as a scattering measurement technique, are also found in phase contrast. Phase contrast has a flat transfer function only if $z = 0$: it's an ideal technique for thin samples.

Dark field doesn't allow to recover any information about the phase of the field. It is not suited to make scattered intensity measurements; a statistical approach, described in the following sections, will give interesting results.

We will describe in Section 3.11 the application of Schlieren technique to the measurement of the scattered intensity.

3.6 Gaussian field generated by the sum of many patterns.

Consider a monodisperse colloid, and the near field scattered light. The field can be decomposed into the sum of the waves coming from the different elements of the colloid. Thus at every distance from the colloid, the field will be given by the sum of many patterns, each randomly placed. An example of this is given in Fig. 3.4 and 3.5. Figure 3.4 shows the pattern: the intensity is linearily dependent on the field $f(\vec{x})$, which we can consider given by the wave scattered by a particle of the colloid. Figure 3.5 shows the sum of the patterns, the function $\rho(\vec{x})$:

$$\rho(\vec{x}) = \sum_{i=1}^{N} f(\vec{x} - \vec{x}_i) \tag{3.48}$$

where the N $\vec{x}_i$ are randomly distributed in a surface of measure S.

Now we will evaluate the P-point correlation functions of the sum of many patterns, $\rho(\vec{x})$. The results will be obteined, first, for fixed particle density $\mathcal{N} = N/S$, and $N \to \infty$; then we will show that, in a suitable limit, the P-point correlation functions, for $P \geq 4$, can be expressed in terms of two-point correlation function, corresponding to the Wick formula. In other words, every connected part of the correlation function developement vanishes: the field becomes gaussian. As a matter of fact, we will prove an extension of the well known central limit theorem.

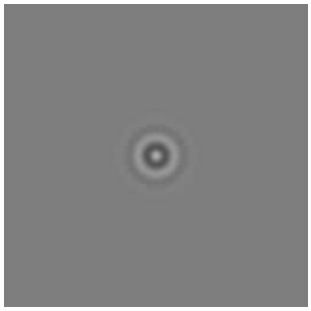

Figure 3.4: Example of the field generated by a particle of the colloid.

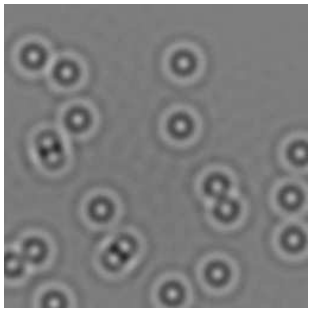

Figure 3.5: Example of the field generated by many particles of the colloid.

In the following, we will consider only functions with a vanishing average value, the other cases being easily obtained from this one. This simplifies the problem, since every odd-P-point correlation function will vanish.

The P-point correlation function of $\rho(\vec{x})$ is:

$$C(\Delta\vec{x}_2,\ldots,\Delta\vec{x}_P) = \langle \rho(\vec{x})\,\rho(\vec{x}+\Delta\vec{x}_2)\ldots\rho(\vec{x}+\Delta\vec{x}_P)\rangle = \frac{1}{S^{N+1}} \sum_{i,j,k,\cdots=1}^{N} \int_S f(\vec{x}-\vec{x}_i)\,f(\vec{x}-\vec{x}_j+\Delta\vec{x}_2)\ldots f(\vec{x}-\vec{x}_k+\Delta\vec{x}_P)\,\mathrm{d}\vec{x}\mathrm{d}\vec{x}_1\ldots\mathrm{d}\vec{x}_N \tag{3.49}$$

The value of the integral does not depend on all the values of the indices $i,j,k,\ldots$, but only on which of them are equal; the sum involves NP terms, but many of them are equal. For example, for $P=4$, the term with $i=1,j=2,k=3,l=4$ is equal to the one with $i=2,j=5,k=7,l=9$, but it is different from the one with $i=1,j=1,k=3,l=4$. The problem is thus to determine in how many ways we can obtain a given configuration.

The calculation can be made more easy using graphs. For evaluating a P-point correlation function, we draw P points on a graph, each one corresponding to one of the points of the correlation function, $0,\Delta\vec{x}_2,\ldots,\Delta\vec{x}_P$. Then, we group the points, so that every set contains an even number of points [1]. Each configuration corresponds to many values of the indices $i,j,k,\ldots$; the number of them is the multiplicity of the graph. Every set corresponds to an operation of integration on a different $\vec{x}_i$. We call G the number of sets; we will have only G integration variables, being the integrand independent on the other $N+1-G$ variables. The integration on these variables gives a factor S^{N+1-G}. Moreover, every integration corresponds to the evaluation of the correlation function $\tilde{C}$ of the single pattern $f(\vec{x})$:

$$\tilde{C}(\Delta\vec{x}_2,\ldots,\Delta\vec{x}_P) = \frac{1}{S}\int f(\vec{x})\,f(\vec{x}+\Delta\vec{x}_2)\ldots f(\vec{x}+\Delta\vec{x}_P)\,\mathrm{d}\vec{x} \tag{3.50}$$

The multiplicity of the graph depends on G; its value is $N(N-1)(N-2)\ldots(N-G+1)$. For $N\to\infty$, we can consider only the leading term N^G.

We can thus describe the rules for evaluating the correlation functions, as the sum of all the graphs. The value of every graph is the product of the factors given by each set. The factor is the product of $\mathcal{N}$ and the correlation function $\tilde{C}$, which correlates all the points in the set.

For example, we evaluate the two-point correlation function (Tab. 3.1) and the four-point correlation function (Tab. 3.2).

For $\mathcal{N}\to\infty$, the leading term in the developement of the correlation function is the one with the higher power of $\mathcal{N}$: it is the one with the higher number of sets. Since sets with an odd number of elements have a vanishing contribution, the greatest number of sets can be obtained only by making sets of

[1] Sets with odd number of points will give vanishing contributions if $f(\vec{x})$ has a vanishing mean value.

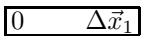

$$C\left(\Delta\vec{x}_1\right) = \mathcal{N}\tilde{C}\left(\Delta\vec{x}_1\right)$$

Table 3.1: Evaluation of the two-point correlation function.

$$C\left(\Delta\vec{x}_1, \Delta\vec{x}_2, \Delta\vec{x}_3\right) =$$

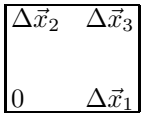

$$\mathcal{N}\tilde{C}\left(\Delta\vec{x}_1, \Delta\vec{x}_2, \Delta\vec{x}_3\right) +$$

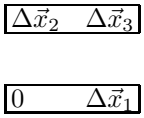

$$\mathcal{N}^2\tilde{C}\left(\Delta\vec{x}_1\right)\tilde{C}\left(\Delta\vec{x}_2 - \Delta\vec{x}_3\right) +$$

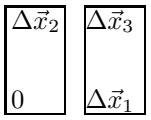

$$\mathcal{N}^2\tilde{C}\left(\Delta\vec{x}_2\right)\tilde{C}\left(\Delta\vec{x}_1 - \Delta\vec{x}_3\right) +$$

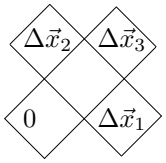

$$\mathcal{N}^2\tilde{C}\left(\Delta\vec{x}_3\right)\tilde{C}\left(\Delta\vec{x}_1 - \Delta\vec{x}_3\right)$$

Table 3.2: Evaluation of the four-point correlation function.

two points. This means that only two point correlation functions of the single pattern $\tilde{C}(\Delta\vec{x})$ contribute to any correlation function $C(\Delta\vec{x}_1, \dots)$ of the sum.

Since $\mathcal{N}$ is dimensional, it is not possible to state if it is small or great. This means that we cannot define, in general, a value of $\mathcal{N}$ so great that the field becomes gaussian. The following heuristic considerations will show that the field is gaussian if $\mathcal{N}A \gg 1$, where A is the area of one pattern, at least if we can define it in some ways. Consider a pattern $f(\vec{x}) = \alpha\chi_A(\vec{x})$. The P-point correlation function of the pattern $f(\vec{x})$, evaluated in $\Delta\vec{x} = 0$, has the value $\tilde{C}(0, \dots)\alpha^P A$. Every graph will have a factor α^P and a factor A^G, where G is the number of sets in the graph. So the factor $\mathcal{N}$ alwais appears multiplied by A. By imposing $\mathcal{N}A \gg 1$, we obtain that the only contributions to the correlation function of the sum of patterns comes from the two point correlation function of the single pattern: all the Wick formulas are valid. In order that $\mathcal{N}A \gg 1$, the mean number of scattering particles inside each area A must be large: many pattern must overlap, in each point.

3.7 Siegert relation for the near field speckles.

Each scatterer of the sample generates a diffraction pattern which, at least in its far field, becomes larger and larger linearly, as the distance z from the screen and the sample is made longer. So, for z longer than a given distance, many diffraction patterns overlap: the Wick formulas should become valid. Unfortunately, the considerations of the previous section cannot be applied directly, since the area the diffraction pattern has not been already defined in a quantitative way.

Now we will prove the Wick formula for the case of Siegert relation, by using the formalism developed in the previous section.

From the results of the previous section, we can evaluate the intensity correlation function of the sum of the patterns, at a given z:

$$\begin{aligned}
\left\langle |E_z(\vec{x})|^2 |E_z(\vec{x}+\Delta\vec{x})|^2 \right\rangle = \\
\mathcal{N}\int \left|\tilde{E}_z(\vec{x})\right|^2 \left|\tilde{E}_z(\vec{x}+\Delta\vec{x})\right|^2 d\vec{x} + \\
\mathcal{N}^2\int \left|\tilde{E}_z(\vec{x})\right|^2 \left|\tilde{E}_z(\vec{y}+\Delta\vec{x})\right|^2 d\vec{x}d\vec{y} + \\
\mathcal{N}^2\int \tilde{E}_z(\vec{x})\,\tilde{E}_z^*(\vec{x}+\Delta\vec{x})\,\tilde{E}_z^*(\vec{y})\,\tilde{E}_z(\vec{y}+\Delta\vec{x})\,d\vec{x}d\vec{y} + \\
\mathcal{N}^2\int \tilde{E}_z(\vec{x})\,\tilde{E}_z(\vec{x}+\Delta\vec{x})\,\tilde{E}_z^*(\vec{y})\,\tilde{E}_z^*(\vec{y}+\Delta\vec{x})\,d\vec{x}d\vec{y}
\end{aligned} \tag{3.51}$$

where $\tilde{E}_z(\vec{x})$ is the field from a single scatterer, at a distance z. Assuming that the phases are random, and considering that the correlation function of any field

does not change with z:

$$\langle I_z(\vec{x})\, I_z(\vec{x}+\Delta\vec{x})\rangle = \mathcal{N}\int \tilde{I}_z(\vec{x})\,\tilde{I}_z(\vec{x}+\Delta\vec{x})\,d\vec{x} + \tag{3.52}$$
$$\mathcal{N}^2\left[\int \tilde{I}_0(\vec{x})\,d\vec{x}\right]^2 + \mathcal{N}^2\left|\int \tilde{E}_0(\vec{x})\,\tilde{E}_0^*(\vec{x}+\Delta\vec{x})\,d\vec{x}\right|^2$$

The first term on the right hand side depends on z: it is the intensity correlation function of the diffraction pattern. Since the diffraction pattern becomes larger as z increases, while the total intensity keeps its value, the intensity correlation function of the diffraction pattern decreases, and vanishes as $z \to \infty$.

In order that Siegert relation holds, for a finite value of z, we must impose that the term with the four point correlation function is negligible compared to the two point ones:

$$\mathcal{N}\int \tilde{I}_z(\vec{x})\,\tilde{I}_z(\vec{x}+\Delta\vec{x})\,d\vec{x} \ll \mathcal{N}^2\left[\int \tilde{I}_0(\vec{x})\,d\vec{x}\right]^2 \tag{3.53}$$

The first term can be substituted by its higher value, the one with $\Delta\vec{x}=0$:

$$\mathcal{N}\frac{\left[\int \tilde{I}_z(\vec{x})\,d\vec{x}\right]^2}{\int \tilde{I}_z^2(\vec{x})\,d\vec{x}} \gg 1 \tag{3.54}$$

The fraction represents the area A covered by the diffraction pattern:

$$\mathcal{N}A \gg 1 \tag{3.55}$$

In order that Siegert relation holds, we need that many particles scatter light inside a single diffraction pattern, that is, any point of the screen must be hit by light coming from many particles. This can be obtained without changing $\mathcal{N}$, but simply increasing z, thus increasing A.

It should be noted that the validity of Vick formulas for a given z does not mean that the field is completely gaussian. For example, we have shown that $\tilde{C}_I^z(\Delta\vec{x}) \to 0$ for $z \to \infty$, where $\tilde{C}_I^z(\Delta\vec{x})$ is the intensity correlation function of the diffraction pattern, defined as $\int \tilde{I}_z(\vec{x})\,\tilde{I}_z(\vec{x}+\Delta\vec{x})\,d\vec{x}$. But this does not imply any uniform convergence. Its integral, $\int \tilde{C}_I^z(\Delta\vec{x})\,d\Delta\vec{x}$, for example, is a constant, and does not vanishes as $z \to \infty$. This means that we can build suitable linear operators, acting on the field, yelding quantities which do not have a gaussian distribution. A dramatic example can be obtained considering the scattering from a two dimensional screen, with many holes of a given shape. As $z \to \infty$, the field meets the Vick formulas ever better. But it is alwais possible to analyze an area, bigger than the diffraction pattern of each hole, and to recover the shape of the holes. This can be done by deconvolving the field by a suitable function: it's the operation made by a lens, which creates an image of the holes. The deconvolution gives any information about the sample,

including the fourth order correlations: the deconvolved field is not gaussian. The gaussianity is only local: once we defined an area, corresponding to the aperture of a lens, there's a distance beyond which we are not able to recover the shape of each hole, and so informations on higher order correlation functions than second order ones are lost.

We can conclude that Eq. (3.55) implies only a local gaussianity; gaussianity is valid only when considering points inside an area small compered with the diffraction pattern of each scatterer. On the other hand, the knowledge of the field on a whole plane allows to recover any information on the correlation function of any order.

3.8 Vanishing of the $\langle EE \rangle$ correlations.

In Eq. (3.51) we neglected the terms like $\int \tilde{E}(\vec{x})\,\tilde{E}(\vec{x}+\Delta\vec{x})\,d\vec{x}$. Such terms should give contributions like $\langle E(\vec{x})\,E(\vec{x}+\Delta\vec{x})\rangle$ in the Vick formulas; we neglected them assuming that the phases are random. In this section we will analyze the conditions under which this happens.

In general, $\langle EE \rangle$ correlations are not negligible. For example, we can consider an opaque screen, with a transmission coefficient dependent on the position, with gaussian distribution. We know that Vick formulas hold. Now, we send a beam through it, and measure the outgoing intensity correlation function, immediately after the screen. Since all the points are in phase, we can assume that the field is real. The Vick formula for the intensity correlation function states that $C_I(\Delta\vec{x}) = \langle I\rangle^2 + 2\,|C_E(\Delta\vec{x})|^2$, due to the not negligible contribution of the term $\langle EE \rangle$, which becomes equal to $\langle EE^* \rangle$. Another example can be found in the theory of shadowgraph: the term $\langle EE \rangle$ is responsible for the oscillations of the transfer function defined in Eq. (3.37).

Now we derive the equations giving the evolution of $\langle EE \rangle$ as z increases. We define:

$$F_z(\Delta\vec{x}) = \int \tilde{E}_z(\vec{x})\,\tilde{E}_z(\vec{x}+\Delta\vec{x})\,d\vec{x} \tag{3.56}$$

The Fourier transform of $F(\Delta\vec{x})$ is:

$$F_z(\vec{q}) = \tilde{E}_z(\vec{q})\,\tilde{E}_z(-\vec{q}) \tag{3.57}$$

We can notice that $F(\vec{q})$ is the power spectrum if $\tilde{E}(-\vec{q})$ is the complex conjugate of $\tilde{E}(\vec{q})$, that is if $E(\vec{x})$ is real. By using Eq. (3.5), we obtain the evolution of $F_z(\vec{q})$:

$$F_z(\vec{q}) = e^{2i\sqrt{k^2-q^2}z}\,\tilde{E}_0(\vec{q})\,\tilde{E}_0(-\vec{q}) \tag{3.58}$$

This gives the evolution equation of $F_z(\vec{q})$:

$$F_z(\vec{q}) = e^{2i\sqrt{k^2-q^2}z}\,F_0(\vec{q}) \tag{3.59}$$

Comparing this equation with Eq. (3.5), we see that $F_z(\vec{q})$ evolves like the electric field $E_z(\vec{q})$, but two times faster than it, as z increases.

The root mean square amplitude of $F_z(\vec{q})$ is a conserved quantity; since $F_z(\vec{x})$ gets larger and larger as z increases, its amplitude must decrease like $1/z$. We can thus define a condition which is enough to ensure that the terms $\langle EE \rangle$ are negligible: the diffraction pattern must be much larger than the correlation lenght. This is implied by Eq. (3.55). The gaussianity condition expressed by Eq. (3.55) is met if many diffraction patterns overlap in every point. This implies that the diffraction pattern of each object must be much larger than the object itself, and than its correlation function, at least if the objects themselves do not overlap.

Some difficulties arise when we consider the power spectrum, or the Fourier transform of $\langle EE \rangle$ terms. As we already explained, the root mean square value of $\langle EE \rangle$ does not depend on z. A Fourier transform, made over a whole plane at a given z, could be divergent, for some values of q, as z increases. For example, we consider a Fourier transform made on a given area S, and we evaluate its mode with wavelength 0, that is, the integral of $F_z(\vec{x})$ over S. It is proportional to S/z. We can consider a square area S, of side $2\pi/q_1$, where q_1 is the wavevector of the longest wavelenght Fourier mode of the square S. So $F_z(\vec{q}=0) \propto 1/q_1^2 z$. Once we selected a q_1, the lowest wavevector we will consider, in order that $\langle EE \rangle$ is negligible with respect to a given value, independent on z, we must impose a $z \propto 1/q_1^2$.

A more quantitative result can be obtained by considering the evaluation of the Fourier transform on S as the evaluation of the Fourier transform on the whole plane, followed by the convolution with the Fourier transform of $\chi_S(\vec{x})$. This is equivalent to considering the discretization of the allowed wavelengths, due to a finite area S. Near a given value of q, the exponential term in Eq. (3.59) makes an oscillation in about k/qz. The discretized intervals are spaced by q_1: if $k/qz \ll q_1$ the oscillations are avereged and vanish. In general, the oscillations will be more visible for small values of q. In order that the oscillations are never visible, $k/q_1 z \ll q_1$: once we have selected q_1, that is the side of S, we must provide that:

$$z \gg \frac{k}{q_1^2}. \tag{3.60}$$

In shadowgraph technique, Eq. (3.60) means that the oscillations of the transfer function are so fast that they cannot be resolved by the sensor, and are thus averaged.

Equation (3.60) has a geometrical interpretation. The vanishing of $\langle EE \rangle$ can be expressed in terms of Fourier modes:

$$\langle E(\vec{q})\, E(-\vec{q}) \rangle = 0 \tag{3.61}$$

The beams, scattered by a modulation with wavevector q, hit the sensor at an angle q/k. Every modulation with wavevector q scatters at two simmetric angles; the resulting modulation on the sensor is thus given by light coming from two different regions, of area S, whose distance is about $2qz/k$. If the distance is longer than $2\pi/q_1$, the side of S, the regions do not overlap: see Fig. 3.6. Equation (3.60) states that we must provide that the regions do not

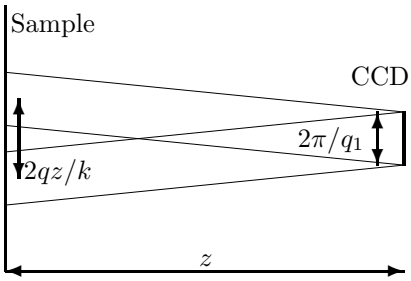

Figure 3.6: Description of the condition of non overlapping of the scattering regions.

overlap. This means that light collected at symmetric angles is not correlated, as required by Eq. (3.61). This condition ensures that the field is gaussian, only if the density of scatterers $\mathcal{N}$ is so that $\mathcal{N}S \gg 1$.

For the scattering from a thin sample, the intensities of the beams scattered at two symmetric angles are equal, and the phases are defined. Since the angles are symmetric, the interference of the scattered beams with the much intense transmitted beam gives two interference patterns, sinusoidal modulations, with the same wavevector, and a given phase. Changing z, the two diffraction patterns change their phase; at some z they sums, and at other values they cancel out. This is the origin of the oscillations in the transfer function of shadowgraph technique, defined in Eq. (3.37). If the condition of Eq. (3.60) is met, the phases of the beams scattered at symmetric directions is random: on average, the transfer function is constant.

The vanishing of the $\langle EE \rangle$ terms can be obtained also by increasing the thickness of the sample. When we pass from the two dimensional, Raman Nath scattering to the three dimensional, Bragg scattering, the correlations between the two beams scattered at the symmetric angles by a given sinusoidal modulation are not preserved. In shadowgraph language, the transfer function oscillations are washed out by superposing many layers, at different z. The thickness of the sample δz must meet the condition $\delta z > k/q_1^2$.

3.9 Homodyne near field speckles.

This technique has been presented very recently [1, 2]. The device for the measurement of the Near Field Speckles is, basically, a misfocused dark field microscope. The transmitted beam is removed, and the image is due only to the light scattered from the sample.

Some of the parameters of the system must be selected: the distance z from the sample to the focal plane of the objective, or from the CCD, if the objective is missing; the diameter D of the sample and of the incident beam; the superficial particle density of the sample. The parameters must be selected on the basis of

the required wavevector range $[q_{min}, q_{max}]$. The ratio q_{max}/q_{min} cannot exceed two decades, due to the finite size and discretization introduced by the CCD sensor. The range $[q_{min}, q_{max}]$ is generally selected in order to cover interesting wavelenghts of the sample: for example, from one tenth to ten diameters of the particles, in the case of the scattering from a monodisperse colloid. Three conditions must be fulfilled.

1. The misfocusing z must be selected in order to meet the condition expressed by Eq. (3.60), with $q_1 = q_{min}$, in order that the correlations $\langle EE \rangle$ vanish:

$$z \gg \frac{k}{q_{min}^2} \tag{3.62}$$

   This condition is stronger than $z \gg k/\left(q_{typ} q_{min}\right)$, where $2\pi/q_{typ}$ is the typical diameter of the particles. Since $2\pi/q_{min}$ is the side L of the images we take, Eq. (3.62) implies that $q_{typ} z/k \gg L$: the diffraction pattern of each particle covers a surface much bigger than the observed one, as required in order that the Fourier transform of the field can be considered gaussian.

2. In order that the field is gaussian, many diffraction patterns must overlap, in each point. Under the condition of Eq. (3.62), in order to fulfill Eq. (3.55), we must only provide that there are many particles in the surface S covered by an image:

$$\mathcal{N} S \gg 1 \tag{3.63}$$

   . For particles suspended in a three dimensional volume, we can define the superficial particle density by multipling the volumetric particle density by the thickness of the cell. In order to fulfill condition (3.63), we can increase the volumetric particle density, or increase the thickness of the sample. Care must be teken in order to avoid multiple scattering.

3. The images we take must collect light scattered at any angle by the sample. The highest wavevector we want to measure is q_{max}; in order that the sensor collect light scattered by that wavevector, coming from any area of the sample, its diameter D must satisfy:

$$D \gg \frac{q_{max}}{k} z \tag{3.64}$$

   This condition ensures that the sensor cannot see the sample boundaries: the sample can be considered as infinite. If the diameter is much less than the one imposed by Eq. (3.64), the speckles are governed by the classical, Van Cittert and Zernike theorem.

Under Eq. (3.62), (3.63) and (3.64), Siegert relation holds:

$$C_I\left(\Delta\vec{x}\right) = \left\langle I\left(\vec{x}\right) I\left(\vec{x} + \Delta\vec{x}\right)\right\rangle = \left\langle I\right\rangle^2 + \left|C_E\left(\Delta\vec{x}\right)\right|^2 \tag{3.65}$$

where the $\langle\cdot\rangle$ is the mean over $\vec{x}$ and $C_E(\Delta\vec{x})$ is the field correlation function. The intensity we measure in a point is not directly connected with any physical part of the sample: each speckle is generate by the superposition of many diffraction patterns.

The measurement of the intensity allows to recover the modulus of the field correlation function through Eq. (3.65). Since $C_E(\Delta\vec{x})$ is the Fourier transform of the power spectrum, which is symmetric and real, $C_E(\Delta\vec{x})$ is also real. Moreover, if we think $C_E(\Delta\vec{x})$ is alwais positive, we can calculate it by extracting a square root. Then, we Fourier transform $C_E(\Delta\vec{x})$, thus obtaining $S_E(\vec{q})$:

$$S_E(q) = \mathcal{F}\left[\sqrt{C_I(\vec{x}) - \langle I\rangle^2}\right](q) \tag{3.66}$$

Using Eq. (3.19), we obtain, for a thin sample:

$$k^2 S_{\delta l}(q) = \frac{1}{\langle I\rangle}\mathcal{F}\left[\sqrt{C_I(\vec{x}) - \langle I\rangle^2}\right](q) \tag{3.67}$$

Using Eq. (3.14), we obtain the scattered intensity:

$$I[Q(q)] = \mathcal{F}\left[\sqrt{C_I(\vec{x}) - \langle I\rangle^2}\right](q) \tag{3.68}$$

The results do not depend on z. The misfocusing z must be enough, in order that the field is gaussian, but its value does not affect the results.

The extraction of the square root of the difference between two experimental data is a dangerous operation, since the difference could be negative. In general, as any other inversion of experimental data, it involves an increase and a distorsion of noise. Chapter 7 provides a detailed description of this problem. This kind of problems are avoided by using ENFS or SNFS, described in Sects. 3.10 and 3.11.

We must notice that Eqs. (3.62) and (3.64) give $D \gg q_{max}/q_{min}^2$. We can think q_{max}/q_{min} as the wavevector dynamic range we want to measure; hopefully it can be about one hundred for spatial measurements. On the other hand, $2\pi/q_{min}$ is of the order of some length of the particles, for example ten times. For example, if we consider 10μm colloids, each image must cover about 100μm. In order to cover two decades in wavelength, we need a D about one hundred times wider: about 1cm. This is not a huge length; moreover, from the industrial point of view, there's no problem in making many acquisitions, with different magnifications and z, for every wavevector range, since each acquisition needs no accurate positioning.

On the other hand, in some cases, for scientific purposes, D should be too wide. This is the case of measurements of non-equilibrium fluctuations, described in Chapt. 9. In this case, we want to evaluate power spectra on two decades in spatial frequencies. The dimension of the largest fluctuations is about one tenth of millimeter: a good statistical sample is about a millimeter large, and the whole sample must be two decades bigger: about 10cm. The building of a Soret cell, or a free diffusion cell, with such an big diameter can be avoided by using SNFS, which will be described in Section 3.11

3.10 Heterodyne near field speckles.

We developed this technique very recently; the device has been patented [3, 4]. The setup for hEterodyne Near Field Speckles measurement is identical to ONFS one, but the beam stop is missing. The transmitted beam is not removed, and the image is due to the interference of the light scattered from the sample with the transmitted beam.

Two parameters of the system must be selected: the distance z from the sample to the focal plane of the objective, or from the CCD, if the objective is missing and the diameter D of the sample and of the incident beam. In ENFS, the superficial particle density of the sample plays no role. The parameters must be selected on the basis of the required wavevector range $[q_{min}, q_{max}]$. The ratio q_{max}/q_{min} cannot exceed two decades, due to the finite size and discretization introduced by the CCD sensor. The range $[q_{min}, q_{max}]$ is generally selected in order to cover interesting wavelenghts of the sample: for example, from one tenth to ten diameters of the particles, in the case of a monodisperse colloid. Two conditions must be fulfilled.

1. The misfocusing z must be selected to meet Eq. (3.62), in order that the correlations $\langle EE \rangle$ vanish. This condition is stronger than $z \gg k/\left(q_{typ} q_{min}\right)$, where $2\pi/q_{typ}$ is the typical diameter of the particles. Since $2\pi/q_{min}$ is the side L of the images we take, Eq. (3.62) implies that $q_{typ} z/k \gg L$: the diffraction pattern of each particle covers a surface much bigger than the observed one, as required in order that the Fourier transform of the field can be considered gaussian.

2. The images we take must collect light scattered at any angle by the sample. The highest wavevector we want to measure is q_{max}; in order that the sensor collect light scattered by that wavevector, coming from any area of the sample, its diameter D must satisfy Eq. (3.64). This condition ensures that the sensor cannot see the sample boundaries: the cample can be considered as infinite. If the diameter is much less than the one imposed by Eq. (3.64), the speckles are governed by the classical, Van Cittert and Zernike theorem.

We can notice that the conditions expressed by Eq. (3.62) and (3.64) must hold for both ONFS and ENFS. On the contrary, in ENFS no condition is imposed on the particle density, in analogy with (3.63), since the field does not need to be gaussian.

In general, Eq. (3.63) is fulfilled by the sample; in that case, the field is gaussian, and the ENFS image represents the interference of a gaussian field with a plane wave. The particle density can be so small that the field is not gaussian; this does not mean that the speckles we see represent real objects in the sample. Each speckle is due to the interference between light scattered by many different particles.

Care must be taken in order to avoid multiple scattering. Since we want avoid multiple scattering, the scattered intensity is small compared to the transmitted

beam intensity: the second order effects in $\delta E/E_0$ can be neglected, and Eq. 3.21 holds.

$$C_i(\Delta\vec{x}) = +\frac{2}{I_0}\Re C_{\delta E}(\Delta\vec{x}) + \frac{2}{I_0^2}\Re\left[E_0^{*2}\left\langle \delta E(\vec{x})\,\delta E(\vec{x}+\Delta\vec{x})\right\rangle\right] \tag{3.69}$$

Under Eq. (3.62), the $\langle EE\rangle$ correlations vanish:

$$C_i(\Delta\vec{x}) = \frac{2}{I_0}\Re C_{\delta E}(\Delta\vec{x}) \tag{3.70}$$

This means that $S_i(q) = \frac{2}{I_0}S_E(q)$. The measurement of the intensity allows to recover the field power spectrum.

Using Eq. (3.19), we obtain, for a thin sample:

$$2k^2 S_{\delta l}(q) = S_i(q) \tag{3.71}$$

Under (3.64), Eq. (3.14) holds. We obtain the scattered intensity:

$$I[Q(q)] = \frac{1}{2}I_0 S_i(q) \tag{3.72}$$

The results do not depend on z. The misfocusing z must be sufficent, in order that the correlations $\langle EE\rangle$ vanish, but its value does not affect the results.

The considerations about the diameter D of the sample hold also for ENFS: Eq. (3.62) and (3.64) give $D \gg q_{max}/q_{min}^2$. This problem has been discussed in Section 3.9. The result is that, in some cases, the sample and the laser beam have to be extremely large. In that cases, SNFS can be used instead of ENFS: that technique will be described in Section 3.11.

Equation (3.72) must be compared with Eq. (3.45), that holds for values of z much less than those imposed by Eq. (3.62). The oscillations in the sensibility of shadowgraph technique come from the non vanishing of $\langle EE\rangle$ correlations, essentially due to the phase relation of the beams scattered at symmetric angles by a thin sample. For example, the zeroes of the transfer function are due to the distructive interference of the symmetrically scattered beams. In ENFS, the phase relation is destroied, because the light that hit the sensor at symmetric angles comes from different regions.

3.11 Schlieren-like near field speckles.

For Schlieren technique, we can use Eq. (3.34), in order to evaluate the power spectrum S_i of the signal $i(\vec{x})$:

$$S_i(\vec{q}) = \begin{cases} \frac{2}{I_0}S_E(-\vec{q}) & \vec{q}\cdot\vec{n} < 0 \\ \frac{2}{I_0}S_E(\vec{q}) & \vec{q}\cdot\vec{n} \geq 0 \end{cases} \tag{3.73}$$

We assume the sample is isotropic, so that $I(\vec{q})$ depends only on $|\vec{q}|$. Using Eq. (3.14):

$$I[Q(\vec{q})] = \frac{1}{2}I_0 S_i(\vec{q}) \tag{3.74}$$

Schlieren technique can alwais be applied to measure the scatterered intensity, no matter how long the misfocusing is. The sample can be thick or thin, in the focal plane or away from it: the result is never affected.

Once the dimension of the image has been selected, in order to observe an interesting range of wavevectors, the diameter of the sample must fulfill the condition expressed by Eq. (3.64), as in ONFS and ENFS, but in this case there's no limitation on z. The diameter will be, in general, sufficient to give a good statistical sample of the particles we are measuring; z will be as small as we can.

In general, for a thick sample, some of the objects will be too small, or too far from the focal plane, to be completely resolved. But their presence will prodece a speckle field, analogous to that of NFS. We will call this technique Schlieren-like Near Fiels Speckles, since it behaves like a true Schlieren technique only for big objects in the focal plane, while for the other cases it allows to measure the statistical properties of a speckle field.

Equation (3.74) must be compared with Eq. (3.45), that holds for values of z much less than those imposed by Eq. (3.62), and without the blade. The oscillations in the sensibility of shadowgraph technique come from the non vanishing of $\langle EE \rangle$ correlations, essentially due to the phase relation of the beams scattered at symmetric angles by a thin sample. In SNFS, the phase relation is destroied, because one of the beams scattered at symmetric angles is stopped.

3.12 Why using NFS instead of classical scattering measurement?

Classical, high angle light scattering works only for scattering angles higher than some degrees. Small angle light scattering (SALS) can measure light scattered by wavelengths of some microns; its main problem is the stray light. The new techniques allow an accurate subtraction of the stray light; in particular, for ENFS and SNFS stray light can be evaluated and subtracted point by point.

All SALS instruments must include some device to stop the transmitted beam, like in ONFS. Moreover, the solid state sensors must be accurately positioned with reference to the focus of transmitted beam. In an industrial instrument, the position of both the beam stop and the sensors must be electronically controlled, in order to correct the deformations due to mechanical stress and temperature dilatations. On the contrary, ENFS has an extremely simple and robust structure, which does not require any adjustment. This makes ENFS suited for industrial applications of light scattering measurement, like particle sizing. In Chapter 8, we will show some particle size measurements performed with ENFS.

In Chapter 9, we will show that SNFS can be used to make a measurement of the power spectrum of the non equilibrium fluctuations in a free diffusion process. Such fluctuations have never been observed by SALS, since they are extremely weak and involve mainly low wavevectors. This shows that NFS

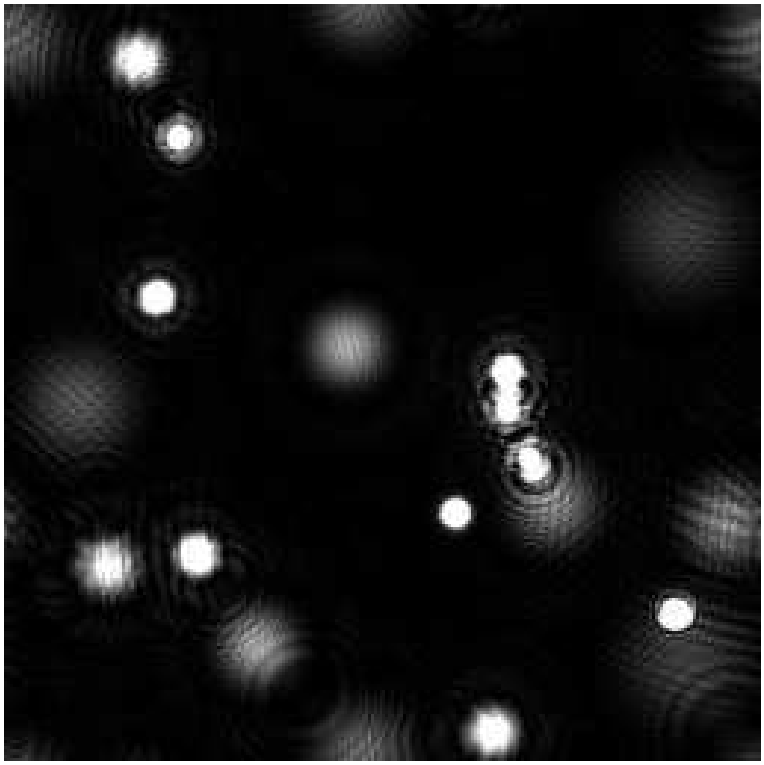

Figure 3.7: Example of dark field image.

techniques can be used to obtain measurements not possible with SALS.

3.13 Why using NFS instead of classical microscopy?

The near scattered field keeps only one feature associated to the observed sample, the correlation function. For example, Figure 3.7 shows a dark field image, and 3.8 shows the corresponding NFS image. The correlation function of the two fields is the same, but looking at the second immage we cannot figure that it comes from a set of discs. With near field scatterig we will never distinguish an amoeba from a paramecium: it is not a microscopy technique. Why using NFS instead of dark field?

The first answer comes from the analysis of Figure 3.7 and 3.8. In Figure 3.7, some of the discs are in the focal plane, other aren't. If we want to analyze a dark field image, we must be able to select the particles which are in the focal plane, and exclude from the analysis all the others. On the contrary, NFS gives informations which are never affected by the misfocusing z: it provides three dimensional informations, and works well for thin samples as well as for thick

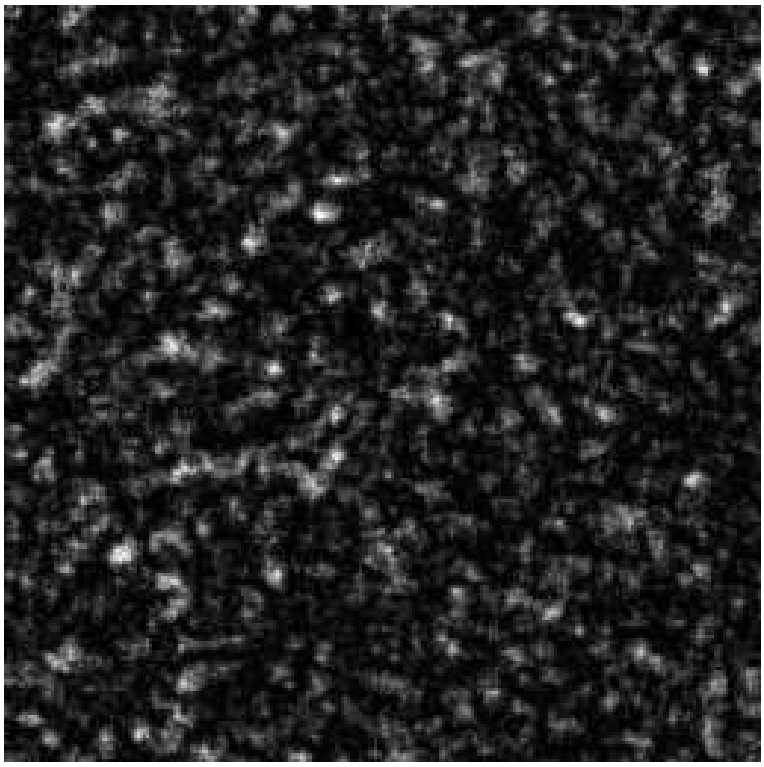

Figure 3.8: Example of Near Field Speckles image.

ones.

If we want to analyze, for example, a colloid by a microscopy technique, we must use a thin sample, in order that the particles can be focused. If the concentration is low, it could be hard to find even one particle. Generally, one microscopic image could show only some particles. On the contrary, NFS can work on thick samples. We can use a given colloid, with any concentration, and put it in a cell so thick that it shows a suitable attenuation.

Another reason leads to use ONFS technique instead of a dark field technique. Dark field image intensity is given by equation 3.29: every calculation based on dark field images will concern the square value of the refraction index fluctuations. In facts, two point correlation functions of the images will represent four point correlation functions of the refraction index fluctuations. We consider a fluid, for which the refraction index fluctuations has a give distribution. We are interested in measuring the two point correlation, but dark field images allow us to work only on four point one. Of course, four point correlation function involves the two point one, but has a non trivial connected contribution. In NFS images, every connected term in correlation functions vanishes: we can measure quantities directly connected with two point correlation functions.

3.14 Meaning of the light path correlation function.

We have shown that NFS allows the measurement of the light scattered in a quite wide range of angles. If Reyleight Gans condition is met, the scattered intensity represents the power spectrum of the sample, evaluated in the transferred wavevector. For the scattering at small angles, the spectrum is evaluated in the direction ortogonal to the incident beam. A measurement of this componet of the spectrum leads, through a Fourier transform, to the correlation function of the light path through the sample:

$$C_{\delta l}\left(\Delta\vec{x}\right)=\int\delta n\left(\vec{x},z\right)\delta n\left(\vec{x}+\Delta\vec{x},z'\right)\mathrm{d}z\mathrm{d}z'\mathrm{d}\vec{x}. \tag{3.75}$$

This quantity is directly accessible from NFS measurements. Its Fourier transform is the power spectrum for $q_z=0$:

$$\begin{aligned}\int C_{\delta l}\left(\Delta\vec{x}\right)e^{-i\vec{q}\cdot\Delta\vec{x}}\mathrm{d}\Delta\vec{x}=\\ \frac{1}{\left(2\pi\right)^6}\int\delta n\left(\vec{q}',q_z'\right)\delta n\left(\vec{q}'',q_z''\right)\\ e^{i\left(\vec{q}'+\vec{q}''\right)\cdot\vec{x}+i\left(\vec{q}''-\vec{q}\right)\cdot\Delta\vec{x}+iq_zz+iq_z'z'}\mathrm{d}\vec{q}'\mathrm{d}\vec{q}''\mathrm{d}\vec{x}\mathrm{d}\Delta\vec{x}.\mathrm{d}q_z'\mathrm{d}q_z''\mathrm{d}z\mathrm{d}z'=\\ \left|\delta n\left(\vec{q},q_z=0\right)\right|^2\end{aligned} \tag{3.76}$$

Through a measurement of the scattered light we can know the power spectrum in the plane perpendicular to the direction of the incident beam. This

means that the light path correlation function bears less informations than the refraction index correlation function, but the light path correlation function is connected to the refraction index correlation function:

$$C_{\delta l}\left(\Delta\vec{x}\right) = \int \delta n\left(\vec{x}, z\right) \delta n\left(\vec{x} + \Delta\vec{x}, z + \Delta z\right) \mathrm{d}\vec{x}\mathrm{d}z\mathrm{d}\Delta z = \int C_{\delta n}\left(\Delta\vec{x}, \Delta z\right) \mathrm{d}\Delta z. \quad (3.77)$$

If the sample is isotropic, its power spectrum depends only on the modulus of the wave vector. If we know the light path correlation function, we can evaluate its Fourier transform, extend it to the three dimensions, and then, appling again the Fourier transform, we obtain the refraction index correlation function. This operation is generally performed by using the well known Abel transform.

Chapter 4

The experimental system.

The whole system is sketched in Fig. 4.1. It consists in the light source, the sample cell and the image forming, capturing and processing system. In the first sections we describe all these parts and the criteria we followed to build our NFS instruments. In Sections 4.7 and 4.8 we describe the three NFS instruments we built.

4.1 The optical system.

The optical system is mainly built using elements supplied by Newport. The optical table is a VH3048 IsoStation. All the elements are mounted on X26 rails, by using CN26 carriers. A picture of the system is shown in Fig. 4.2.

For the experiment descibed in Chapter 9, the optical axis must be vertical. The X26 rails are held in vertical position by mounting them on an X95 rail with suitable carriers: see Fig. 4.3.

4.2 The light source.

The light source we use is a LED laser, coupled to a single mode fiber, supplied by Newport. In Tab. 4.1 we show the data supplied with the LED. Figure 4.4 shows the LED laser and the fiber.

The LED is housed in a Newport 700P temperature controller mount, connected to a temperature controller and a current driver. Since the output wavelenght depends on the temperature, a temperature controller is needed. The LED laser has a built-in monitoring photodiode. The current driver monitors the output power to keep it constant.

A single mode fiber is directly pigtailed to the LED. The other end of the fiber is terminated by an FC/PC connector. It is held by a Newport SL50BM, a gimbal mount for the adjustment of the azimuth and elevation, originally built for mounting mirrors or beam splitters. The beam output by the fiber is diverging; we collimate it by sending it through a lens with a focal of 5cm.

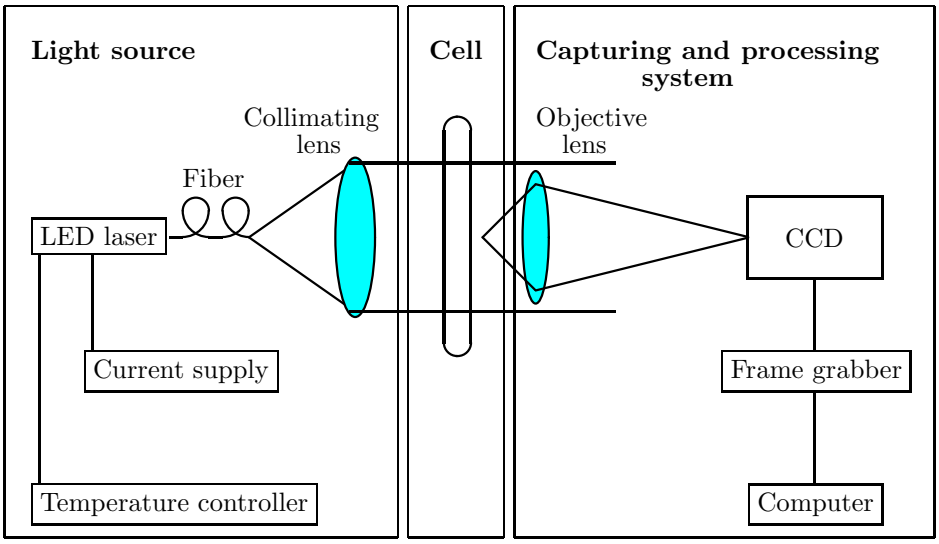

Figure 4.1: The experimental system.

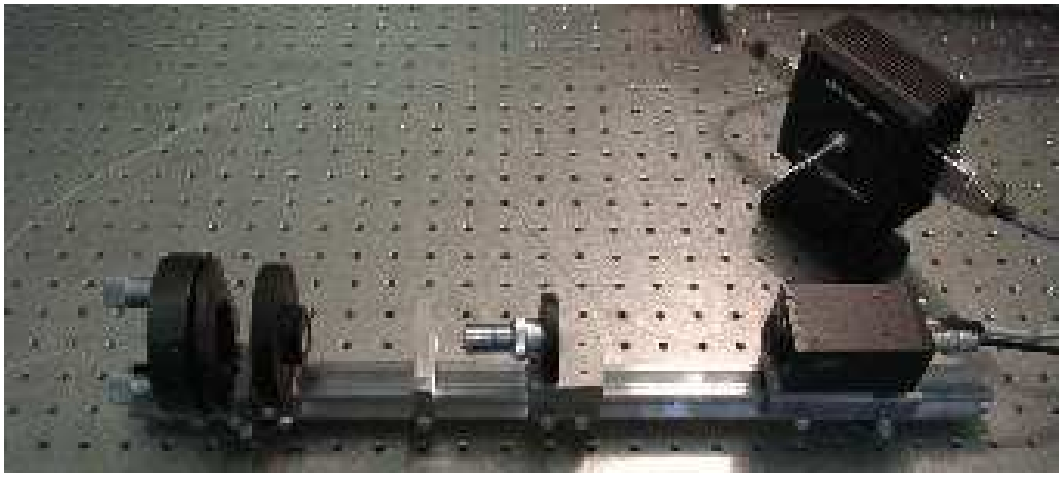

Figure 4.2: Picture of the optical system. From left to right, we can see the adjustable mount that holds the fiber, the collimating lens, the cell, the microscope objective and the CCD camera. In the upper right corner there's the laser mount.

Figure 4.3: A view of the optical system for the experiment described in Chapter 9. All the optical elements are alligned in vertical direction. From the bottom, we see the optic fiber, held by an adjustable mount, the collimating lens, the cell, held by the column on the left, the focusing lens, the blade, the neutral filter, and the CCD camera.

Item code	LD-635-31A
Center wavelength	635nm
Wavelength range	±10nm
Fiber output power	1.2mW
Threshold current	10mA
Operating current	40mA
Rise/fall time	1.5ns
Operating temperature	−10 to 40°C
Fiber core/clad diameter	4/125μm - single mode

Table 4.1: Data of the LED laser.

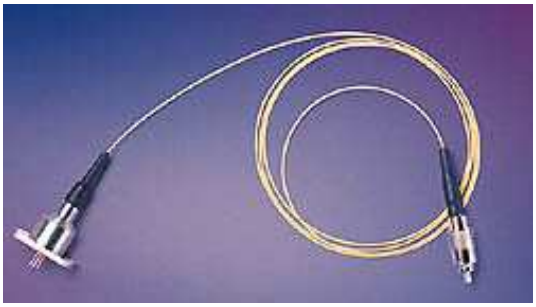

Figure 4.4: The LED laser.

The resulting beam has a diameter of about 2cm. This diameter is enough for our experiments; in general, it must be selected as a function of the wavevector range $[q_{min}, q_{max}]$ we want to measure. For ONFS and ENFS, D, the diameter over which the beam intensity is constant, must be selected in order to fulfill Eq. (3.64). The best choice is:

$$D \gtrapprox 50 \frac{q_{max}}{q_{min}^2} \tag{4.1}$$

For SNFS, the beam must have a diameter which covers a good statistical sample:

$$D \gtrapprox 20/q_{min}. \tag{4.2}$$

Both the adjustment of the direction of the beam and its collimation are not critical operations. The direction of the beam must be adjusted to hit a lens, centered at the optical axis, half a meter away from the fiber end. The collimation is checked by measuring the beam diameter on a screen, near the lens and one meter away. The collimator is shown in Fig. 4.5.

The LED laser has been used in order to test its performance for industrial applications. The LED laser is much more compact and robust than a gas laser; it can operate immediately after it has been powered on and it does not generate too many heat. For these features it is ideally suited for industrial applications. Moreover, the overall cost of a LED laser device included in an industrial product can be made extremely low, as in the case of CD readers, though a laboratory LED laser equipement can cost as much as a classical gas laser. Moreover, the output of a gas laser must be spatially filtered before being used. A spatial filter is a critical component in an industrial equipement, since it must be extremely stable, and must be adjusted by micrometric actuators controlled by sensors, in order to correct the deformations due to heating and mechanical stresses. On the contrary, the single mode fiber output is more uniform than the output of a spatial filter, and requires no adjustment.

4.3 The cell.

The liquid samples we measure are held in a cell; the diameter D must be selected following Eq. (4.1) for ONFS and ENFS, or Eq. (4.2) for SNFS.

For homogeneous samples, like colloids, the thickness must be selected in order to have a suitable attenuation of the main beam, about 1%. For ONFS measurements, the thickness of the cell and the volumetric particle density must fulfill Eq. (3.63); generally this condition is spontaneously met.

For ONFS and ENFS measurements, the parallelism between the windows of the cell is not critical, nor the optical quality of them. Since the measured scattered light comes from different regions of the sample, we must provide that it is homogeneous. This implies that the thickness must be uniform, but an optical quality allignment is far beyond what is needed. On the contrary, SNFS requires optical quality windows: the well known "Foucault test" sees every deformation of the wavefront, no matter if the associated wavelength is long.

Figure 4.5: A view of the collimator and the cell. From the bottom, we see the optic fiber, held by an adjustable mount, the collimating lens, and the cell.

The cells we used are described in detail in Chapters 7 and 9.

4.4 Objective, beam stop and blade.

The objective must form an image of a given plane on the CCD sensor. The magnification M must be selected in order that the required wavevector range $[q_{min}, q_{max}]$ is inside the wavevector range the CCD sensor can measure: about $\left[2 \times 10^3 \mathrm{m}^{-1}, 2 \times 10^5 \mathrm{m}^{-1}\right]$. This means that:

$$\left[\frac{q_{min}}{M}, \frac{q_{max}}{M}\right] \subseteq \left[2 \times 10^3 \mathrm{m}^{-1}, 2 \times 10^5 \mathrm{m}^{-1}\right] \tag{4.3}$$

Moreover, the numerical aperture of the lens must be enough to resolve details as small as the smallest wavelength involved, $2\pi/q_{max}$, or, equivalently, to collect light scattered at an angle q_{max}/k.

In our experiments, we used a 20X microscope objective for high magnification factors, and an achromatic, 10cm focal length doublet for magnification factor around 1. An achromatic doublet has also been tested for high magnification factors, since we do not require the high quality of a microscope objective, nor an extremely wide numerical aperture. Experiments proved no different performances of the doublet compared with the microscope objective, but it was more difficult to obtain the required magnification.

The objective lens must be placed so that it creates an image of a given plane on the CCD sensor. For ONFS and ENFS, the plane must be at a distance z from the sample fulfilling Eq. (3.60). The best choice is:

$$z \approx 25 \frac{k}{q_{min}^2} \tag{4.4}$$

For SNFS:

$$z < \frac{kD}{2q_{max}} \tag{4.5}$$

For ONFS, the transmitted beam, focused by the objective, is stopped by an opaque or reflective element. In microscope objectives, the focal plane is inside, between two groups of lenses: we insert the beam stop through a hole. We tried three kinds of beam stops: a thin wire, a reflective wedge and an absorbing disc impressed by on a photographic film. The wire has a diameter of 70μm; it si stretched in the focal plane and is positioned by micrometric screws. It reflects the light inside the objective, and this could, in principle, increase the stray light. The photographic film we used are high contrast, black and white, 36mm photographic films. The beam stop is circular, but the beam is not completely blocked, thus increasing the stray light. The wedge was obtained by a steel blade; the edge was kept parallel to the optic axis. The upper part, in the direction from which the light comes, was cut at 45° and polished, in order to obtain a surface that reflects the main beam outside the lens mount, through a second hole. A section of the objective lens is shown in figure (4.6). This kind of beam stop is not symmetrical with respect to the optical axis. This

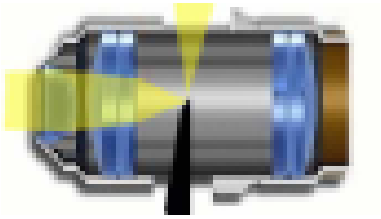

Figure 4.6: Section of the microscope objective and the beam stop.

could increase the difficulty to process the data. During the experiments, all the methods showed to be almost equivalent. Figure 4.7 shows the mount that holds the beam stop.

For SNFS, a blade must be placed in the plane where the transmitted beam is focused. The blade must be extremely sharp: a razor blade is required. We mount it on a system with three micrometric screws, in order to accurately position it in the space. A picture of the Schlieren system is shown in Fig. 4.8.

4.5 CCD sensor.

We used an industrial CCD camera: JAI CV M50. An image is shown in Fig. 4.9; the data are provided in Tab. 4.2.

The output is a standard CCIR; since it is interlaced, an image is alwais formed by two fields acquired with a time delay of 0.04s, although the internal shutter allows to acquire a single frame in 100ns.

The number of pixels and their dimension determine the wavevector range the CCD can directly measure: $\left[2 \times 10^3 \mathrm{m}^{-1}, 2 \times 10^5 \mathrm{m}^{-1}\right]$. Other wavevector ranges can be covered, by creating on image with a suitable magnification factor, but we cannot cover more than two decades.

4.6 The acquisition and elaboration system.

The frame grabber we used is an IC-RGB, from Imaging Technology. It performs an 8 bit digitalization of three standard composite video signals from the CCD cameras. It can be used to acquire simultaneously from two syncronized CCD cameras, for evaluating the intensity correlation function on two different planes, or to acquire from a single camera.

The syncronyzed acquisition from two cameras can be used to evaluate the three dimensional correlation function; the meaning of the three dimensional correlation function is explained in Appendix A.

The software for image elaboration was developed under Linux, written in C language. The drivers and the libraries are the “IC-PCI” provided by “GOM Optical Measurements Techniques”. The algorithms used to process the images are described in Chapt. 5 and 6.

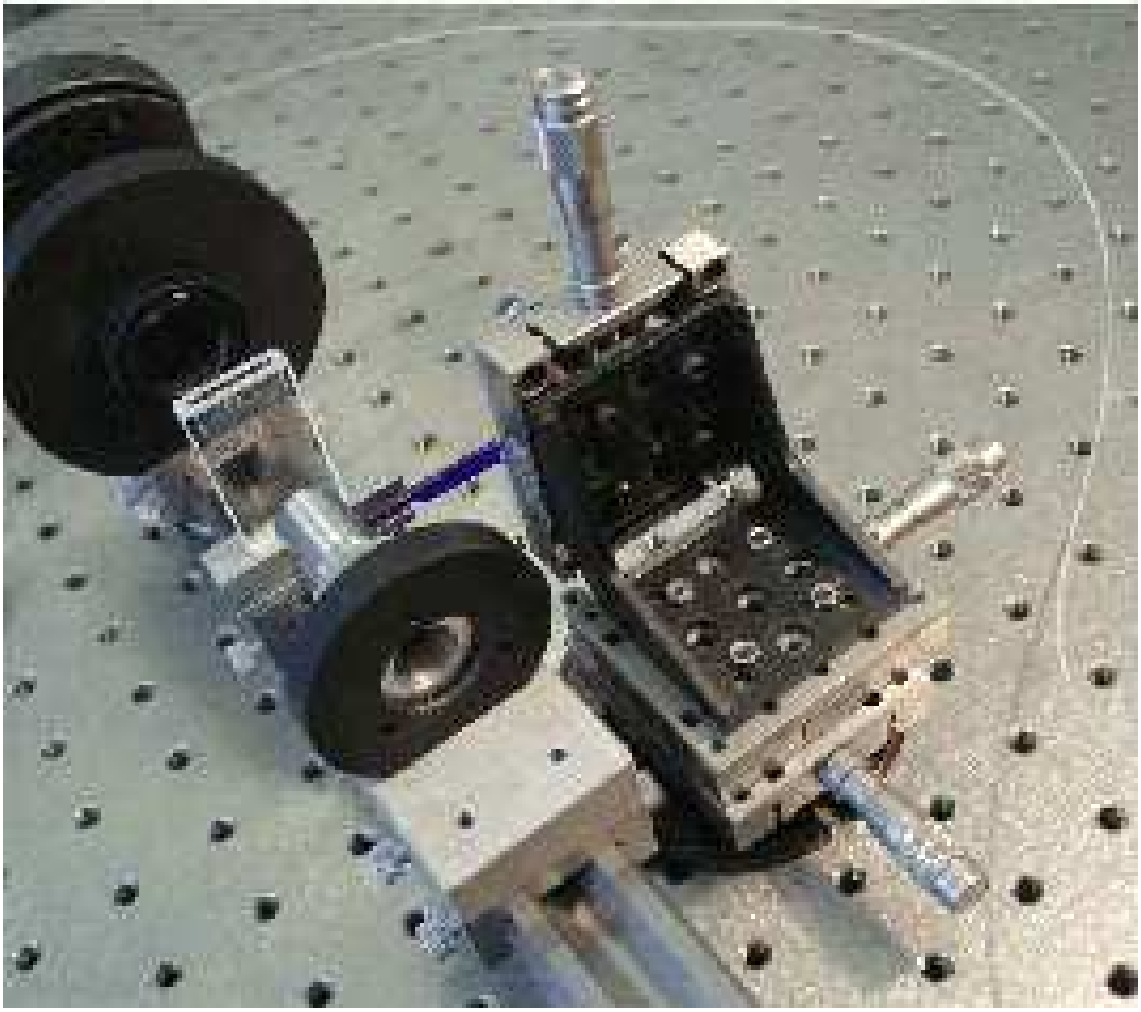

Figure 4.7: Picture of the microscope objective with the beam stop. The beam stop is glued to the blue rod, held by a mount with three micrometric screws, for the adjustment of the position in every direction.

Figure 4.8: A view of the Schlieren system. From the bottom, we see the cell, the focusing lens, the blade, held by a micrometric mount, the neutral filter and the CCD camera.

Specifications	CV-M50C
Scanning system	625 lines 25 frames/s
CCD Sensor	Monochrome 1/2" Hyper HAD IT CCD
Sensing area	6.6mm×4.8mm
Picture elements effective	752×582
Elements in video out	737×575
Cell size	8.6×8.3
Resolution (horizontal)	560 TV lines
Resolution (vertical)	575 TV lines
Sensitivity	0.5 lux, f1.4
Sensitivity peak wave length	500nm
Wave length range	400nm - 675nm (sensitivity > 50%)
S/N ratio	>56dB (AGC off, Gamma 1)
Video output	Composite VBS Signal 1.0 V_{pp}, 75 Ω
Gamma	0.45 - 1.0
Gain	Manual - Automatic
Scanning	2:1 interlace
Accumulation	Field - Frame
Syncronization	Internal, Xtal-generated - External HD/VD - random trigger
HD Sync input - output	4V, 75 Ω
VD Sync input - output	4V, 75 Ω
Trigger input	4V, 75 Ω
Trigger input duration	> HD interval
WEN output (write enable)	4V, 75 Ω
EEN output (exposure enable)	4V, 75 Ω
Pixel clock out (optional)	4V, 75 Ω
Internal shutter	Off,1/100s, 1/250s, 1/500s, 1/1000s, 1/2000s, 1/4500s, 1.10000s
Trigger shutter	1/60,1/100s, 1/250s, 1/500s, 1/1000s, 1/2000s, 1/4500s, 1.10000s
Long time exposures	one field to $+\infty$. Duration between external VD pulses.
Operating temperature	-5°C to +45°C
Humidity	20%-80% non-condensing
Storage temperature	-25°C to +60°C
Storage humidity	20%-90%
Power	12V DC ±10% 2.5W
Lens mount	C-mount
Dimensions	40mm×50mm×80mm
Weight	245g

Table 4.2: Specification of Jai CV M50C camera.

Figure 4.9: Jai CV M50 camera.

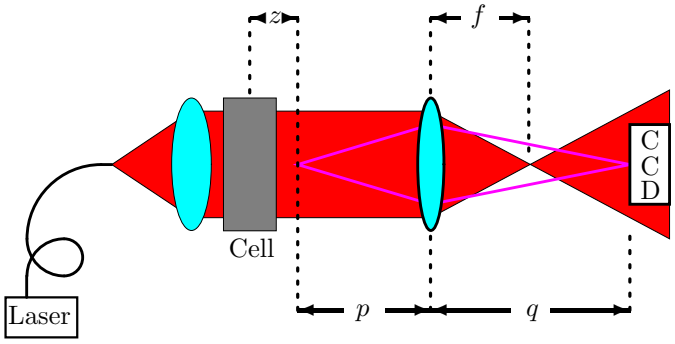

Figure 4.10: The optical setupt for the measurement of scattering from colloids some microns large with ENFS.

4.7 ONFS and ENFS setup for colloid measurements.

The systems are sketched in Figs. 4.10 and 4.11.

The measurements described in Chapters 7 and 8 cover the wavevector range $[q_{min}, q_{max}]$ about $\left[2 \times 10^5 \mathrm{m}^{-1}, 4 \times 10^6 \mathrm{m}^{-1}\right]$. By using Eqs. (4.1) and (4.4), we obtain $D \gtrapprox 5$mm and $z \approx 6$mm. A 2cm beam diameter, obtained with lenses with 25mm diameter, as shown in Fig. 4.2, is enough to ensure that the intensity is constant over the length D. For the measurements described in Chapters 7 and 8, we used larger lenses with 50mm diameter, with a larger beam diameter, in order to ensure a better uniformity, and z was increased acordingly.

Following Eq. (4.3), we obtain the magnification: $M = 20$. We used a 20X microscope objective and numerical aperture of 0.45.

The whole optical system for ENFS is shown in Fig. 4.2.

For ONFS, we insert a beam stop through a hole inside the lens mount. The beam stop and its adjustable mount is shown in Fig. 4.7.

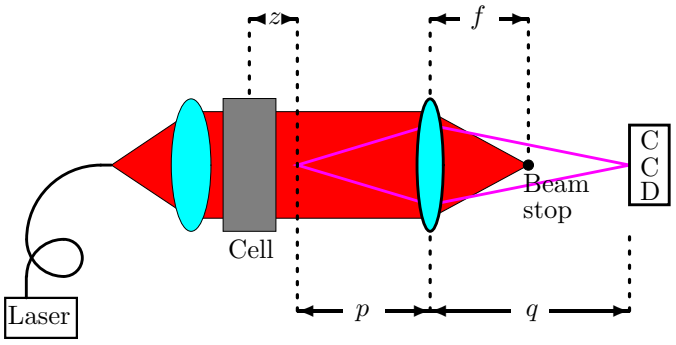

Figure 4.11: The optical setupt for the measurement of scattering from colloids some microns large with ONFS.

4.8 SNFS setup for non equilibrium fluctuation measurements.

The overall system is sketched in Fig. 4.12.

The range $[q_{min}, q_{max}]$ of the fluctuations we measure is about $\left[2 \times 10^3 \mathrm{m}^{-1}, 2 \times 10^5 \mathrm{m}^{-1}\right]$, that is, the fluctuations range from ten microns to some millimeters. By using Eqs. (4.2) and (4.5), we obtain $D \gtrapprox 10\mathrm{mm}$ and $z < 125\mathrm{mm}$. The cell we used, described in Chapter 9, has an internal diameter of about 25mm.

Following Eq. (4.3), we obtain the magnification: $M = 1$. We used an achromatic doublet with a 25mm diameter and focal length $f = 100\mathrm{mm}$. To obtain the required magnification, $p = q = 200\mathrm{mm}$. Since SNFS is affected by small inhomogeneous fluctuations of air temperature, we choose to put the collimating lens and the objective lens as close as possible to the cell, in order to prevent air movements. This resulted in a negative z.

The whole optical system is shown in Fig. 4.3.

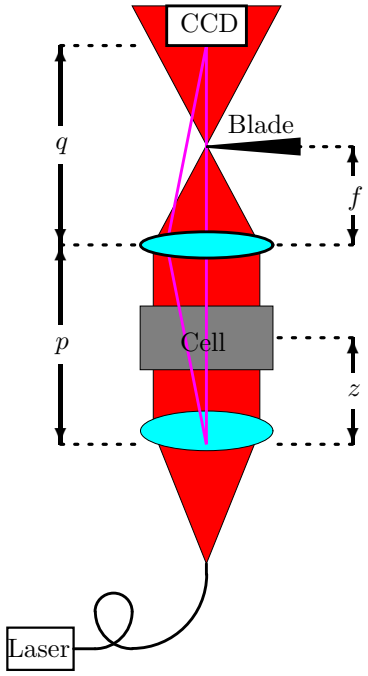

Figure 4.12: The optical setupt for the measurement of non equilibrium fluctuations with SNFS.

Chapter 5

ONFS data processing.

In the chapter 3, we showed that, under some given conditions, the correlation function of ONFS images can be used to derive the intensity of the light scattered by a sample. The calcultions were performed in the ideal case, in which the scattered light comes only from the sample. The presence of non ideal lenses and optical elements introduces an amount of undesired scattered light. This problem is common to every kind of scattering measurement; the undesired light, often referred to as stray light, is generally scattered at small angles.

In standard scattering measurements, the effect of the undesired light is additive. It can be subtracted, since the stray light can be measured by a blank measurement.

Dynamic scattering gives a way to distinguish the effect of the light scattered from elements that evolve with time from stationary ones. If the stray light comes from stationary elements, such as imperfections of the optical elements, its effect is to increase the correlation function, with no dependence on the delay. Thus the time dependent informations on the sample will be given by the bell shaped part of the correlation function, while the pedestal will contain informations on both the statically and dynamically scattered light.

If a blank measurement is possible, a more refined subtraction of the stray light becomes possible [18], provided that the stray light constitutes a speckle field, that is, the field is gaussian. Such a data processing can be extended to ONFS too. In the following sections, we will find a way to subtract the effect of the stray light, first considering an unlimited number of images, taken at different times, and then a finite set of images. Then, we will describe the whole data processing algorithm.

5.1 Effect of the stray light.

From a set of ONFS images $I(\vec{x})$, we can measure the intensity correlation function:

$$C_I(\Delta\vec{x}) = \{\langle I(\vec{x})\, I(\vec{x}+\Delta\vec{x})\rangle\}, \tag{5.1}$$

where $\langle\cdot\rangle$ is the mean over $\vec{x}$, $\{\cdot\}$ is the mean over different images, and the intensity of the images $I(\vec{x})$ is the intensity of the sum of $\delta E(\vec{x})$, the field scattered by the sample, and $E_{SL}(\vec{x})$, the field of the stray light:

$$I(\vec{x}) = |\delta E(\vec{x}) + E_{SL}(\vec{x})|^2 . \tag{5.2}$$

So we obtain:

$$C_I(\Delta\vec{x}) = \left\{ \left\langle \left[|\delta E(\vec{x})|^2 + |E_{SL}(\vec{x})|^2 + \delta E(\vec{x}) E_{SL}^*(\vec{x}) + \delta E^*(\vec{x}) E_{SL}(\vec{x}) \right] \left[|\delta E(\vec{x}+\Delta\vec{x})|^2 + \left| E_{SL}\left(x+ \right. \right. \right. \right. \tag{5.3}$$

Since $\delta E(\vec{x})$ is a random, circular gaussian field, the mean over different images of its odd powers vanishes; since $E_{SL}(\vec{x})$ is static, it can be considered as a costant, with respect to $\{\cdot\}$, the average on the images:

$$\begin{aligned} C_I(\Delta\vec{x}) = {} & \left\{ \left\langle |\delta E(\vec{x})|^2 |\delta E(\vec{x}+\Delta\vec{x})|^2 \right\rangle \right\} + \left\langle |E_{SL}(\vec{x})|^2 |E_{SL}(\vec{x}+\Delta\vec{x})|^2 \right\rangle + \\ & \left\langle \left\{ |\delta E(\vec{x})|^2 \right\} |E_{SL}(\vec{x}+\Delta\vec{x})|^2 \right\rangle + \left\langle |E_{SL}(\vec{x})|^2 \left\{ |\delta E(\vec{x}+\Delta\vec{x})|^2 \right\} \right\rangle + \\ & \langle \{\delta E(\vec{x}) \delta E^*(\vec{x}+\Delta\vec{x})\} E_{SL}^*(\vec{x}) E_{SL}(\vec{x}+\Delta\vec{x}) \rangle + \\ & \langle \{\delta E^*(\vec{x}) \delta E(\vec{x}+\Delta\vec{x})\} E_{SL}(\vec{x}) E_{SL}^*(\vec{x}+\Delta\vec{x}) \rangle . \end{aligned} \tag{5.4}$$

The mean over the images $\{\cdot\}$ equals the mean over $\vec{x}$, $\langle\cdot\rangle$, for the field $\delta E(\vec{x})$:

$$\begin{aligned} C_I(\Delta\vec{x}) = {} & \left\langle |\delta E(\vec{x})|^2 |\delta E(\vec{x}+\Delta\vec{x})|^2 \right\rangle + \left\langle |E_{SL}(\vec{x})|^2 |E_{SL}(\vec{x}+\Delta\vec{x})|^2 \right\rangle + \\ & \left\langle |\delta E(\vec{x})|^2 \right\rangle \left\langle |E_{SL}(\vec{x}+\Delta\vec{x})|^2 \right\rangle + \left\langle |E_{SL}(\vec{x})|^2 \right\rangle \left\langle |\delta E(\vec{x}+\Delta\vec{x})|^2 \right\rangle + \\ & \langle \delta E(\vec{x}) \delta E^*(\vec{x}+\Delta\vec{x}) \rangle \langle E_{SL}^*(\vec{x}) E_{SL}(\vec{x}+\Delta\vec{x}) \rangle + \\ & \langle \delta E^*(\vec{x}) \delta E(\vec{x}+\Delta\vec{x}) \rangle \langle E_{SL}(\vec{x}) E_{SL}^*(\vec{x}+\Delta\vec{x}) \rangle . \end{aligned} \tag{5.5}$$

Since both $\delta E(\vec{x})$ and $E_{SL}(\vec{x})$ are gaussian fields, we can use Siegert relation Eq. (3.65) to express four-point correlation functions in terms of two-point ones.

$$\begin{aligned} C_I(\Delta\vec{x}) = {} & \left\langle |\delta E(\vec{x})|^2 \right\rangle \left\langle |\delta E(\vec{x}+\Delta\vec{x})|^2 \right\rangle + |\langle \delta E(\vec{x}) \delta E^*(\vec{x}+\Delta\vec{x}) \rangle|^2 + \\ & \left\langle |E_{SL}(\vec{x})|^2 \right\rangle \left\langle |E_{SL}(\vec{x}+\Delta\vec{x})|^2 \right\rangle + |\langle E_{SL}(\vec{x}) E_{SL}^*(\vec{x}+\Delta\vec{x}) \rangle|^2 + \\ & \left\langle |\delta E(\vec{x})|^2 \right\rangle \left\langle |E_{SL}(\vec{x}+\Delta\vec{x})|^2 \right\rangle + \left\langle |E_{SL}(\vec{x})|^2 \right\rangle \left\langle |\delta E(\vec{x}+\Delta\vec{x})|^2 \right\rangle + \\ & \langle \delta E(\vec{x}) \delta E^*(\vec{x}+\Delta\vec{x}) \rangle \langle E_{SL}^*(\vec{x}) E_{SL}(\vec{x}+\Delta\vec{x}) \rangle + \\ & \langle \delta E^*(\vec{x}) \delta E(\vec{x}+\Delta\vec{x}) \rangle \langle E_{SL}(\vec{x}) E_{SL}^*(\vec{x}+\Delta\vec{x}) \rangle . \end{aligned} \tag{5.6}$$

We define $\langle \delta I \rangle = \left\langle |\delta E(\vec{x})|^2 \right\rangle$, $\langle I_{SL} \rangle = \left\langle |E_{SL}(\vec{x})|^2 \right\rangle$, $C_{\delta E}(\Delta\vec{x}) = \langle \delta E(\vec{x}) \delta E^*(\vec{x}+\Delta\vec{x}) \rangle$, $C_{SL}(\Delta\vec{x}) = \langle E_{SL}(\vec{x}) E_{SL}^*(\vec{x}+\Delta\vec{x}) \rangle$:

$$\begin{aligned} C_I(\Delta\vec{x}) = {} & \langle \delta I \rangle^2 + |C_{\delta E}(\Delta\vec{x})|^2 + \langle I_{SL} \rangle^2 + |C_{SL}(\Delta\vec{x})|^2 + \\ & 2 \langle \delta I \rangle \langle I_{SL} \rangle + C_{\delta E}(\Delta\vec{x}) C_{SL}^*(\Delta\vec{x}) + C_{\delta E}^*(\Delta\vec{x}) C_{SL}(\Delta\vec{x}) . \end{aligned} \tag{5.7}$$

The result is that the stray light field correlation sums to the scattered field correlation:

$$C_I(\Delta\vec{x}) = (\langle\delta I\rangle + \langle I_{SL}\rangle)^2 + |C_{\delta E}(\Delta\vec{x}) + C_{SL}(\Delta\vec{x})|^2 . \tag{5.8}$$

In order to obtain informations about the correlation of the stray light field, we acquire a great number of images, with different scattered field, and we average them, thus obtaining the correlation function of the mean intensity $\{I(\vec{x})\}$. Then, we measure the correlation function of the mean intensity:

$$C_{\{I\}}(\Delta\vec{x}) = \langle\{I(\vec{x})\}\{I(\vec{x}+\Delta\vec{x})\}\rangle . \tag{5.9}$$

We evaluate the mean intensity $\{I(\vec{x})\}$:

$$\{I(\vec{x})\} = \left\{|\delta E(\vec{x}) + E_{SL}(\vec{x})|^2\right\} = \left\{|\delta E(\vec{x})|^2\right\} + \left\{|E_{SL}(\vec{x})|^2\right\} + \{\delta E(\vec{x}) E^*_{SL}(\vec{x})\} + \{\delta E^*(\vec{x}) E_{SL}(\vec{x})\} . \tag{5.10}$$

Since E_{SL} does not depend on the image:

$$\{I(\vec{x})\} = \left\{|\delta E(\vec{x})|^2\right\} + |E_{SL}(\vec{x})|^2 + \{\delta E(\vec{x})\} E^*_{SL}(\vec{x}) + \{\delta E^*(\vec{x})\} E_{SL}(\vec{x}) . \tag{5.11}$$

Using the gaussian properties of the scattered light:

$$\{I(\vec{x})\} = \langle\delta I\rangle + |E_{SL}(\vec{x})|^2 . \tag{5.12}$$

Now we can evluate the correlation function of the mean intensity:

$$C_{\{I\}}(\Delta\vec{x}) = \left\langle\left[\langle\delta I\rangle + |E_{SL}(\vec{x})|^2\right]\left[\langle\delta I\rangle + |E_{SL}(\vec{x}+\Delta\vec{x})|^2\right]\right\rangle = \langle\delta I\rangle^2 + \langle\delta I\rangle\left\langle|E_{SL}(\vec{x})|^2\right\rangle + \langle\delta I\rangle\left\langle|E_{SL}(\vec{x}+\Delta\vec{x})|^2\right\rangle + \left\langle|E_{SL}(\vec{x})|^2|E_{SL}(\vec{x}+\Delta\vec{x})|^2\right\rangle . \tag{5.13}$$

Using the gaussian properties of the field E_{SL}:

$$C_{\{I\}}(\Delta\vec{x}) = (\langle\delta I\rangle + \langle I_{SL}\rangle)^2 + |C_{SL}(\Delta\vec{x})|^2 \tag{5.14}$$

From eq. (5.12), we can evaluate the mean value of the intensity of the images:

$$\{\langle I\rangle\} = \langle\delta I\rangle + \langle I_{SL}\rangle \tag{5.15}$$

Eq. (5.8), (5.14), (5.15) give some informations about the field correlation of the scattered and stray light. If both the correlation functions are real and positive, the best evaluation of the field correlation function of the scattered field is:

$$C_E(\Delta\vec{x}) = \sqrt{C_I(\Delta\vec{x}) - \{\langle I\rangle\}^2} - \sqrt{C_{\{I\}}(\Delta\vec{x}) - \{\langle I\rangle\}^2} \tag{5.16}$$

5.2 Correction for finite samples.

In order to evaluate the correlation function of the mean intensity, we average a given amount of images, then we evaluate the correlation function of the obtained mean value. Since the number of images we average is finite, the correlation function will not correspond to that of eq. (5.14). For example, if the stray light vanishes, the mean intensity will still present fluctuations, due to the scattered light. These fluctuations vanish as the square root of the number of the averaged images, and consequently the correlation function becomes flat only for infinite samples.

A similar problem arises when working with a stochastic, gaussian variable. If we have N values of the stocastic variable x, distributed with probability $P(x) \propto \exp\left[-(x-x_0)/\left(2\sigma^2\right)\right]$, we find that the best value for x_0 is the mean of the values x, and the best value for σ is the root mean square displacement of the values x from x_0. On the other hand, the average on a finite number of elements will be displaced from x_0 of an amount, vanishing as the square root of the number of the samples N, but so that the root mean square displacement of the data from the mean is alwais smaller than σ. It is thus necessary to use the Bessel correction, dependent on the number of the samples N.

Generally the Bessel correction is obtained in consequence of the "maximum likelihood" condition. This means that, given a set of values of a stochastic variable, and given a family of probability distributions, the parameters of the family must be selected in order to maximize the probability of finding the given data. Another approach is to find a suitable algorithm which gives the values of the parameters, from a set of data. The algorithm will be selected in order that the output values will be distributed around the true ones, with minimum square displacement. For a gaussian distribution, the two approaches give the same result. It is easy to show that, for example for a Heaviside distribution, the maximum likelihood condition fails to obtain the best results.

In our case, the distribution function of the intensity is not gaussian. We will use weak condition, that is, we will look for an algorithm giving values which average to the true ones. In other words: we will try to avoid sistematic erroneous evaluations of the correlation function.

We define $\bar{\cdot}$ as the mean over N samples. In particular $C_{\bar{i}}$ is the correlation function of the averaged N images. To avoid sistematic errors, we must first evaluate $\{C_{\bar{I}}\}$:

$$\{C_{\bar{I}}(\Delta\vec{x})\} = \left\{\left\langle \bar{I}(\vec{x})\,\bar{I}(\vec{x}+\Delta\vec{x})\right\rangle\right\}, \tag{5.17}$$

where the average intensity of N images $\bar{I}$ is given by the sum of the field scattered by the sample $\delta E(\vec{x})$ and the field of the stray light $E_{SL}(\vec{x})$:

$$\bar{I}(\vec{x}) = \frac{1}{N}\sum_n \left|\delta E_n(\vec{x}) + E_{SL}(\vec{x})\right|^2. \tag{5.18}$$

So we obtain:

$$\{C_{\bar{I}}(\Delta\vec{x})\} = \frac{1}{N^2}\sum_{n,m}\left\{\left\langle\left[|\delta E_n(\vec{x})|^2 + |E_{SL}(\vec{x})|^2 + \delta E_n(\vec{x})\,E^*_{SL}(\vec{x}) + \delta E^*_n(\vec{x})\,E_{SL}(\vec{x})\right]\left[|\delta E_m(\vec{x}+\Delta\vec{x})|^2 + \left|E_{SL}\left(x + \right.\right.\right.\right. \tag{5.19}$$

We can follow the calculations performed in Section 5.1 to obtain Eq. (5.8). In this case we obtain:

$$\begin{aligned}
\{C_{\bar{I}}(\Delta\vec{x})\} = {} & \frac{1}{N^2}\sum_{n,m}\left\langle|\delta E_n(\vec{x})|^2\right\rangle\left\langle|\delta E_m(\vec{x}+\Delta\vec{x})|^2\right\rangle + \\
& \frac{1}{N^2}\sum_{n,m}|\langle\delta E_n(\vec{x})\,\delta E^*_m(\vec{x}+\Delta\vec{x})\rangle|^2 + \\
& \left\langle|E_{SL}(\vec{x})|^2\right\rangle\left\langle|E_{SL}(\vec{x}+\Delta\vec{x})|^2\right\rangle + |\langle E_{SL}(\vec{x})\,E^*_{SL}(\vec{x}+\Delta\vec{x})\rangle|^2 + \\
& \frac{1}{N^2}\sum_{n,m}\left\langle|\delta E_n(\vec{x})|^2\right\rangle\left\langle|E_{SL}(\vec{x}+\Delta\vec{x})|^2\right\rangle + \\
& \left\langle|E_{SL}(\vec{x})|^2\right\rangle\frac{1}{N^2}\sum_{n,m}\left\langle|\delta E_m(\vec{x}+\Delta\vec{x})|^2\right\rangle + \\
& \frac{1}{N^2}\sum_{n,m}\langle\delta E_n(\vec{x})\,\delta E^*_m(\vec{x}+\Delta\vec{x})\rangle\langle E^*_{SL}(\vec{x})\,E_{SL}(\vec{x}+\Delta\vec{x})\rangle + \\
& \frac{1}{N^2}\sum_{n,m}\langle\delta E^*_n(\vec{x})\,\delta E_m(\vec{x}+\Delta\vec{x})\rangle\langle E_{SL}(\vec{x})\,E^*_{SL}(\vec{x}+\Delta\vec{x})\rangle\,.
\end{aligned} \tag{5.20}$$

The mean values can be calculated, provided that the two cases, $n = m$ and $n \neq m$ are taken into account:

$$\begin{aligned}
\{C_{\bar{I}}(\Delta\vec{x})\} = {} & \langle\delta I\rangle^2 + \frac{1}{N}|C_{\delta E}(\Delta\vec{x})|^2 + \langle I_{SL}\rangle^2 + |C_{SL}(\Delta\vec{x})|^2 + 2\langle\delta I\rangle\langle I_{SL}\rangle + \\
& \frac{1}{N}C_{\delta E}(\Delta\vec{x})\,C^*_{SL}(\Delta\vec{x}) + \frac{1}{N}C^*_{\delta E}(\Delta\vec{x})\,C_{SL}(\Delta\vec{x})\,.
\end{aligned} \tag{5.21}$$

The result reduces to eq. (5.14) in the limit $N \to \infty$:

$$\{C_{\bar{I}}(\Delta\vec{x})\} = (\langle\delta I\rangle + \langle I_{SL}\rangle)^2 + \frac{N-1}{N}|C_{SL}(\Delta\vec{x})|^2 + \frac{1}{N}|C_{\delta E}(\Delta\vec{x}) + C_{SL}(\Delta\vec{x})|^2\,. \tag{5.22}$$

From eq. (5.8), (5.22) and (5.15) we can evaluate the field correlation function:

$$C_E(\Delta\vec{x}) = \sqrt{C_I(\Delta\vec{x}) - \{\langle I\rangle\}^2} - \sqrt{\frac{N}{N-1}C_{\bar{I}}(\Delta\vec{x}) - \frac{1}{N-1}C_I(\Delta\vec{x}) - \{\langle I\rangle\}^2} \tag{5.23}$$

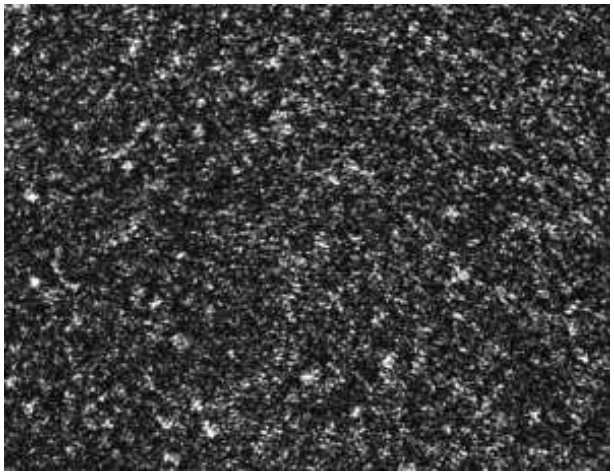

Figure 5.1: Near field intensity of the light scattered by a colloid of 5.2μm.

5.3 Data processing algorithm.

Once the experimental apparatus has been built, as described in Chapter 4, and the sample is placed in it, we acquire one hundred images. The electronic shutter of the CCD and its interlacement time must be so short that no evident evolution of the system happens during the exposure: for the samples we measured, that is colloids some microns large, with brownian movements, and non equilibrium fluctuations in the free diffusion of simple liquids, an interlacement delay of 1/25s is sufficient. Moreover, different images must be completely uncorrelated. For a 10.0μm colloid, images must be grabbed at intervals longer than one minute, if only brownian movements are the source of decorrelation. For the non equilibrium fluctuations we studied, the interval was about one second.

In figure 5.1 and 5.2 we show two typical images of the near field intensity of the light scattered by colloids of 5.2μm and 10.0μm. We can notice the different typical size of the speckles.

For each image, we evaluate the correlation function. This operation is quite fast, since we can use a Fast Fourier Transform (FFT) algorithm. An FFT algorithm allows to evaluate the Fourier tranform of an $M \times N$ matrix, with a number of arithmetic operations proportional to $MN \log(MN)$. By using Perceval relation, we can obtain the correlation function by making an FFT, evaluating the square modulus, and making an Inverse FFT (IFFT). This only requires a number of operation of the order of $MN \log(MN)$. By scanning every value of Δx, and averaging over every $N \times M$ pixels, the number of operations would be of the order of $(MN)^2$. Using FFT, care must be taken in order to correcly evaluate the correlations near the boundarys: FFT assumes periodic boundarys, so the image must be embedded in a bigger matrix, filled with zeroes. Since the FFT is faster if N and M are powers of 2 [19], we used a

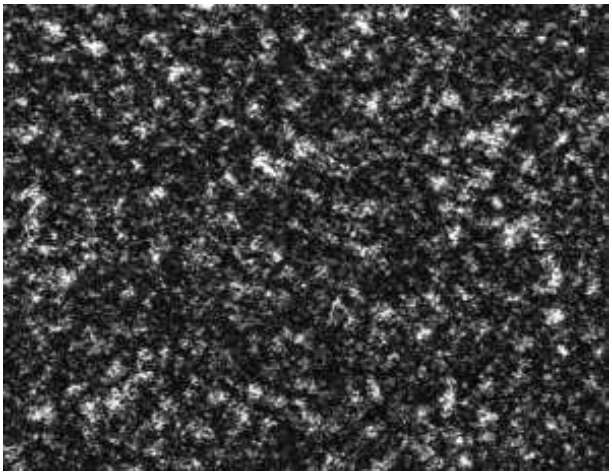

Figure 5.2: Near field intensity of the light scattered by a colloid of 10.0μm.

matrix of 1024×1024 points. After the correlation function has been evaluated, we normalize it, by dividing by the number of independent couples used to evaluate the correlation function.

The correlation functions of every image are averaged, thus obtaining $C_I(\Delta\vec{x})$. Fig. 5.3 and 5.4 show typical graphs of the intensity correlation function $C_I(\Delta\vec{x})$, for a colloid made of polystyrene spheres with diameters of 5.2μm and 10.0μm. We can notice that the correlation function has a maximum at $\Delta\vec{x} = 0$, then decreases, until it reaches the plateau value, about one half the peak value. This behaviour is typical of every speckle field.

Neglecting the stray ligth, we could evaluate the field correlation function by using the Siegert relation, Eq. (3.65):

$$C_E(\Delta\vec{x}) = \sqrt{C_I(\Delta\vec{x}) - \langle I\rangle^2} \tag{5.24}$$

where the mean intensity $\{\langle I\rangle\}$, is obtained by averaging the measured intensity over every pixel of the image and over every image. In Fig. 5.5 and 5.6 are shown typical graphs of the field correlation function, calculated from the intensity correlation function, without any correction for the stray light. The correlation should vanish for $\Delta x \to \infty$, in absence of stray light.

In order to subtract the contribution of the stray light, we evaluate the correlation function of the average of all the images, thus obtaining $C_{\bar{I}}(\Delta\vec{x})$. The evaluation of the correlation function is obtained with the above described algorithm. In Fig. 5.7 and 5.8 are shown typical graphs of the correlation function of the mean intensity, for the two colloids. The graphs are not flat, due to the stray light.

Through Eq. (5.23) we evaluate $C_E(\Delta\vec{x})$, under the hypothesis that both the stray light field and the scattered light field have a real and positive correlation

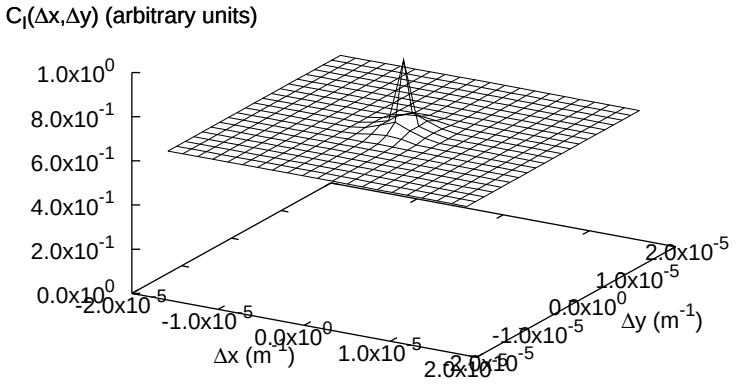

Figure 5.3: Intensity correlation function $C_I(\Delta\vec{x})$, for a colloid made of polystyrene spheres with diameter of 5.2μm

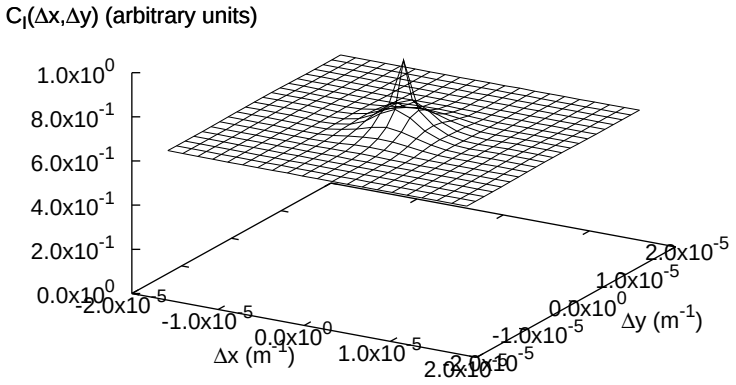

Figure 5.4: Intensity correlation function $C_I(\Delta\vec{x})$, for a colloid made of polystyrene spheres with diameter of 10.0μm

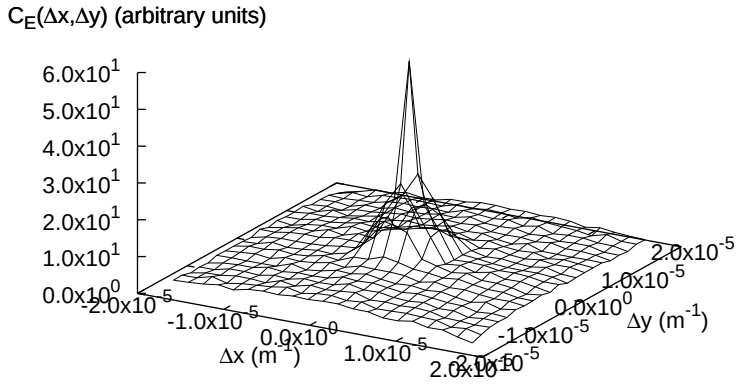

Figure 5.5: Field correlation function $C_E\left(\Delta\vec{x}\right)$, not corrected for the stray light, for the colloid made of polystyrene spheres with diameter of 5.2μm

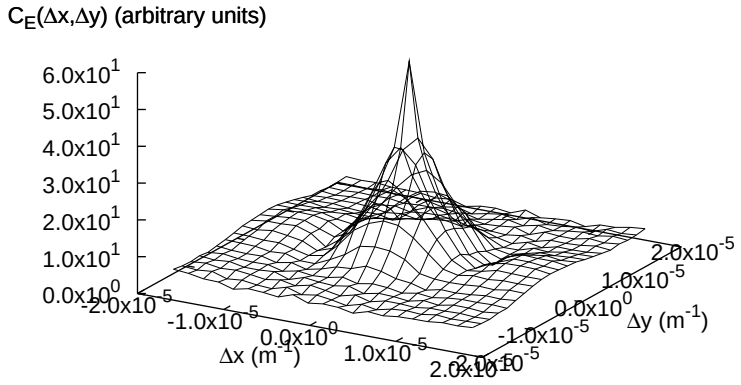

Figure 5.6: Field correlation function $C_E\left(\Delta\vec{x}\right)$, not corrected for the stray light, for the colloid made of polystyrene spheres with diameter of 10.0μm

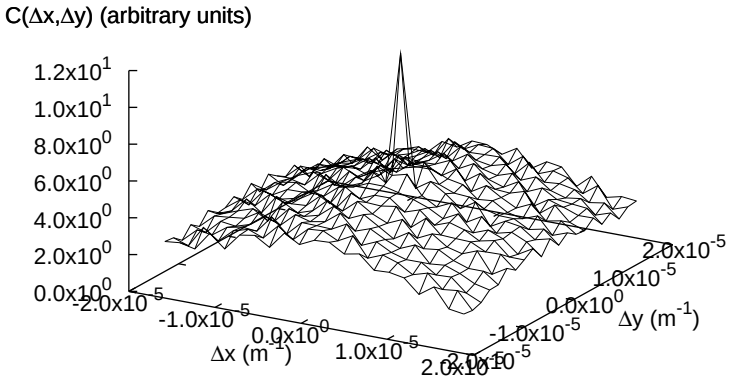

Figure 5.7: Correlation function of the mean intensity $C_{\bar{I}}(\Delta\vec{x})$, for the colloid made of polystyrene spheres with diameter of 5.2μm

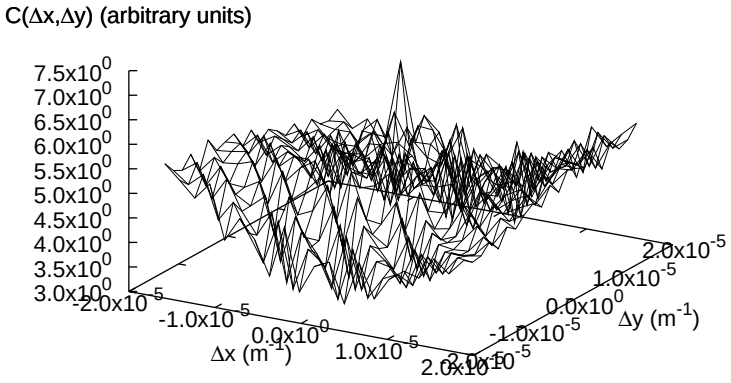

Figure 5.8: Correlation function of the mean intensity $C_{\bar{I}}(\Delta\vec{x})$, for the colloid made of polystyrene spheres with diameter of 10.0μm

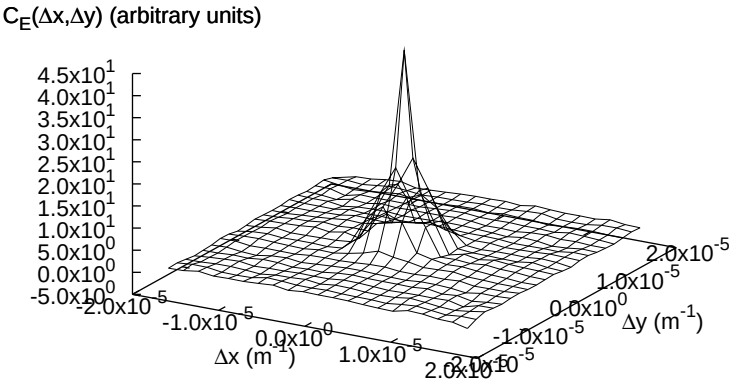

Figure 5.9: Field correlation function $C_E(\Delta\vec{x})$ for the colloid made of polystyrene spheres with diameter of 5.2μm

function. Typical field correlation function, corrected for the stray light using Eq. (5.23), are shown in figure 5.9 and 5.10: we can notice a signitificative increase in the smoothness of the graphs, with respect to Fig. 5.5 and 5.6.

We apply a Fourier tranform to the two dimensional correlation function $C_E(\Delta\vec{x})$, thus obtaining the field power spectrum $S_E(q)$. Since our samples are isotropic, we make an angular average of the power spectra, and represent our data as a function of the modulus q of $\vec{q}$. The scattered intensity $I(q)$ is then obtained by using Eq. (3.14), that is, simply relating each value of the power spectra, with wavelength q to a value of $I(Q)$, where the relation $Q(q)$ is given by Eq. (3.13). In Fig. 5.11 and 5.12 we show the measured $I(q)$.

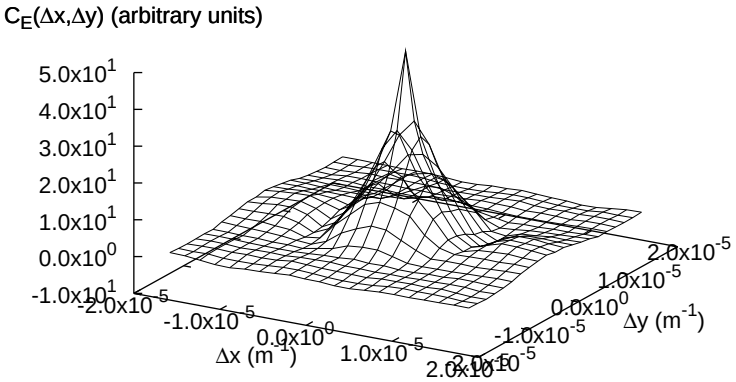

Figure 5.10: Field correlation function $C_E\left(\Delta\vec{x}\right)$ for the colloid made of polystyrene spheres with diameter of 10.0μm

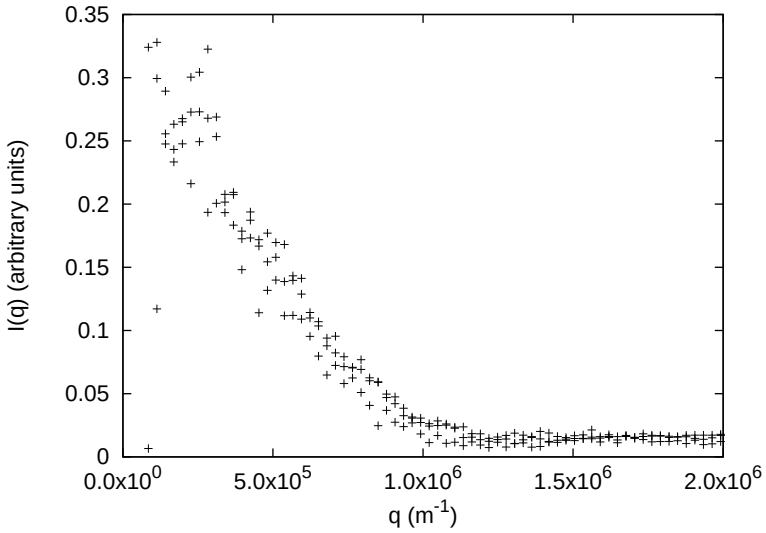

Figure 5.11: ONFS measurement of the scattered intensity of a 5.2μm colloid.

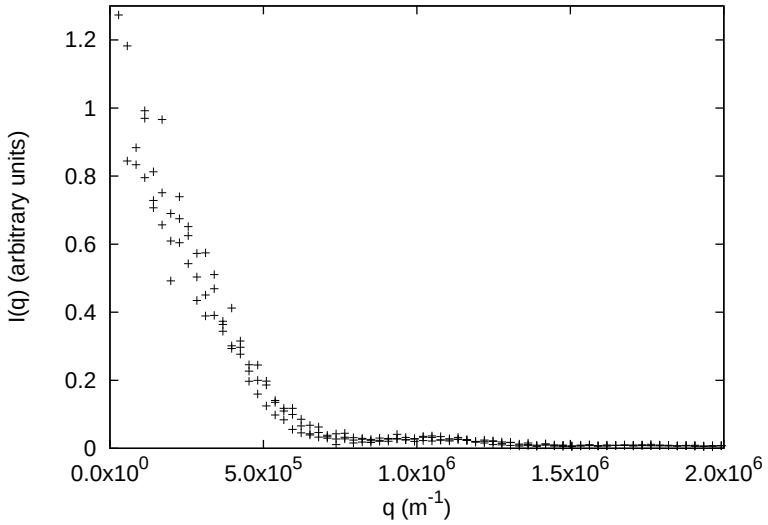

Figure 5.12: ONFS measurement of the scattered intensity of a 10.0μm colloid.

Chapter 6

ENFS and SNFS data processing.

In this chapter we describe the algorithm used to process ENFS and SNFS data, acquired by a CCD, in order to evaluate of the scattered intensity. From a set of images, taken at different times, we are able to subtract the stray light, point by point: this is a noteworthy feature of the heterodyne techniques. The algorithm we describe is similar to the one which has been applied to shadowgraph, and should work for every heterodyne technique.

The algorithm has been applied to SNFS, and the results are shown in Chapter 9; in this chapter, all examples refers to colloid measurements made with ENFS.

6.1 Subtraction of the stray light

As in every heterodyne technique, we measure the overall intensity $I(\vec{x})$, generated by the interference of an object field $\delta E(\vec{x})$ with a more intense reference beam with amplitude E_0. In our case, the object field is generated by the scattered beams, and the reference beam is the transmitted one. We measure the heterodyne signal $i(\vec{x})$:

$$i(\vec{x}) = \frac{I(\vec{x}) - I_0}{I_0}, \tag{6.1}$$

where I_0 is the mean intensity. At first order in $\delta E/E_0$, Eq. (3.22) holds:

$$i(\vec{x}) = 2\frac{\Re[\delta E(\vec{x})]}{E_0}, \tag{6.2}$$

where we have assumed that E_0 is real. Equation (3.72) states that, under the conditions in which NFS works, the power spectrum of $i(\vec{x})$ is the power spectrum of the electric field, the quantity we must measure in order to evaluate the scattered intensities.

We developed an algorithm to subtract the contribution of the stray light, directly on each image, point by point. This is a noteworthy feature of the heterodyne techniques, since in dynamic light scattering and in ONFS the subtraction is possible only on the scattered intensity or on the correlation function, averages of square values. The scattered field can be decomposed into $E_{SL}(\vec{x})$, the stray light field, and $\delta E(\vec{x})$, the field of the light scattered by the sample. Both $E_{SL}(\vec{x})$ and $\delta E(\vec{x})$ are much less intense than E_0, the reference field. At the first order, the resulting intensity is:

$$I(\vec{x}) = E_0^2 + 2E_0 \Re[E_{SL}(\vec{x})] + 2E_0 \Re[\delta E(\vec{x})] \tag{6.3}$$

In many cases, $\delta E(\vec{x})$ fluctuates in time and is correlated only on finite delays. On the contrary, stray light comes mainly from hard surfaces, and does not change as times go on. This is the case of the samples we studied. The spatial average of a scattered field is alwais wanishing; this property, along with the absence of correlation on different images, says that the average over many images of $\delta E(\vec{x})$ vanishes.

In order to separate the contribution of the stray light, we average $I(\vec{x})$ over many different images. Since the phase of $\delta E(\vec{x})$ is random, its mean vanishes:

$$\{I(\vec{x})\} = E_0^2 + 2E_0 \Re[E_{SL}(\vec{x})]. \tag{6.4}$$

We use the symbol $\{\cdot\}$ for the mean over many samples, and the symbol $\langle\cdot\rangle$ for the mean over $\vec{x}$. The fluctuation $I(\vec{x}) - \{I(\vec{x})\}$ does not depend on $E_{SL}(\vec{x})$:

$$I(\vec{x}) - \{I(\vec{x})\} = 2E_0 \Re[\delta E(\vec{x})]. \tag{6.5}$$

Because of the conservation of the total intensity during the scattering process, by averaging $\{I(\vec{x})\}$ over the whole plane, we obtain I_0:

$$\langle\{I(\vec{x})\}\rangle = E_0^2 = I_0. \tag{6.6}$$

We can now evaluate the heterodyne signal $i(\vec{x})$, subtracting the the stray light contribution:

$$i(\vec{x}) = \frac{I(\vec{x}) - \{I(\vec{x})\}}{\langle\{I(\vec{x})\}\rangle}. \tag{6.7}$$

6.2 Correction for finite samples.

The quantity $\{I(\vec{x})\}$ should ideally be evaluated by averaging infinite images. We obtain a good evaluation of it by averaging a great number N of images $I_n(\vec{x})$, typically one hundred:

$$\bar{I}(\vec{x}) = \frac{1}{N}\sum I_n(\vec{x}) \approx \{I(\vec{x})\} \tag{6.8}$$

From this evaluation, we obtain $i(\vec{x})$:

$$i_n(\vec{x}) = \frac{I_n(\vec{x}) - \bar{I}(\vec{x})}{\langle\bar{I}\rangle} \tag{6.9}$$

The average value $\bar{I}(\vec{x})$, evaluated over a given number of images, is sistematically different from the true mean value, in the direction that reduces the evaluation of the root mean square displacement from the mean. This problem is analogous to the one that leads to the so called Bessel correction for the evaluation of the variance σ of a stochastic variable, from the knowledge of a finite number of stochastic values.

We evaluate the correlation function of $i_n(\vec{x})$ for each n, then we average them, thus obtaining $C_i(\Delta\vec{x})$. Now we want to evaluate $\{C_i(\Delta\vec{x})\}$, that is the mean value over infinite samples, in order to correct systematic errors:

$$\{C_i(\Delta\vec{x})\} = \frac{1}{\left\langle \bar{I} \right\rangle^2} \left\{ \frac{1}{N} \sum_{n=0}^{N} \left\langle \left[I_n(\vec{x}) - \frac{1}{N} \sum_{m=0}^{N} I_m(\vec{x}) \right] \left[I_n(\vec{x}+\Delta\vec{x}) - \frac{1}{N} \sum_{m=0}^{N} I_m(\vec{x}+\Delta\vec{x}) \right] \right\rangle \right\} \tag{6.10}$$

The symbol $\langle\cdot\rangle$ means the average over $\vec{x}$. We can write$\bar{I}(\vec{x}) + \delta I(\vec{x})$ instead of $I_n(\vec{x})$:

$$\{C_i(\Delta\vec{x})\} = \frac{1}{\left\langle \bar{I} \right\rangle^2} \left\{ \frac{1}{N} \sum_{n=0}^{N} \left\langle \left[\delta I_n(\vec{x}) - \frac{1}{N} \sum_{m=0}^{N} \delta I_m(\vec{x}) \right] \left[\delta I_n(\vec{x}+\Delta\vec{x}) - \frac{1}{N} \sum_{m=0}^{N} \delta I_m(\vec{x}+\Delta\vec{x}) \right] \right\rangle \right\} \tag{6.11}$$

Evaluating the products:

$$\begin{aligned} \{C_i(\Delta\vec{x})\} \quad = \quad & \frac{1}{\left\langle \bar{I} \right\rangle^2} \frac{1}{N} \sum_{n=0}^{N} \{\langle \delta I_n(\vec{x})\, \delta I_n(\vec{x}+\Delta\vec{x}) \rangle\} - & (6.12) \\ & \frac{1}{\left\langle \bar{I} \right\rangle^2} \frac{1}{N^2} \sum_{n,m=0}^{N} \{\langle \delta I_n(\vec{x})\, \delta I_m(\vec{x}+\Delta\vec{x}) \rangle\} - \frac{1}{\left\langle \bar{I} \right\rangle^2} \frac{1}{N^2} \sum_{n,m=0}^{N} \{\langle \delta I_m(\vec{x})\, \delta I_n(\vec{x}+\Delta\vec{x}) \rangle\} & (6.13) \\ & \frac{1}{\left\langle \bar{I} \right\rangle^2} \frac{1}{N^3} \sum_{n,m,l=0}^{N} \{\langle \delta I_m(\vec{x})\, \delta I_l(\vec{x}+\Delta\vec{x}) \rangle\} & (6.14) \end{aligned}$$

Since $\bar{\delta I} = 0$:

$$\{C_i(\Delta\vec{x})\} = \frac{N-1}{N} \frac{1}{\left\langle \bar{I} \right\rangle^2} \{\langle \delta I(\vec{x})\, \delta I(\vec{x}+\Delta\vec{x}) \rangle\} \tag{6.15}$$

Now we can use Eq. (6.5):

$$\{C_i(\Delta\vec{x})\} = \frac{N-1}{N} C_E(\Delta\vec{x}) \tag{6.16}$$

The correlation function evaluated on N samples is proportional to the correlation function evaluated for $N \to \infty$. The poportionality constant is the same of the well known Bessel correction.

6.3 ENFS data processing.

Once the experimental apparatus has been built, as described in Chapter 4, in the absence of the sample, the CCD should be illuminated in a quite uniform

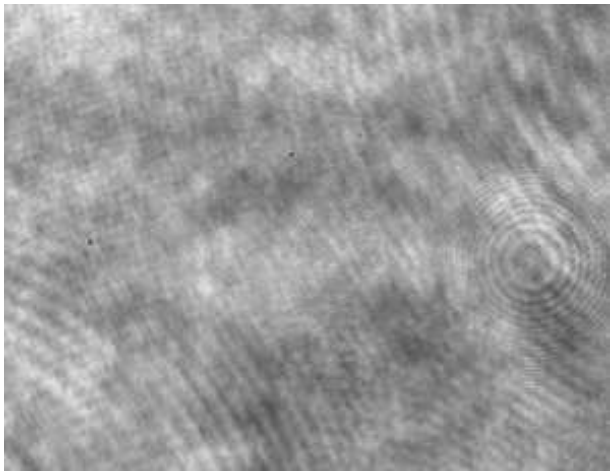

Figure 6.1: Background image.

way. As a matter of fact, the illumination is never completely uniform, primarily because of the interference of the main beam with stray light. A typical image is shown in Fig. 6.1. We can easily see some sets of concentric circles, each due to reflections inside a lens, along with speckle patterns properly due to stray light.

When the the sample is placed in the right position, we acquire about one hundred images for each measurement. The electronic shutter of the CCD and its interlacement time must be so short that no evident evolution of the system happens during the exposure: for the samples we studied, an interlacement delay of 1/25s is sufficient. Moreover, different images must be completely uncorrelated. For a 10μm colloid, images must be grabbed at intervals longer that one minute, if only brownian movements are the source of decorrelation, while for the non equilibrium fluctuations we studied the images can be taken at intervals of 1s. In figure 6.2 and 6.3 we show two typical ENFS images, generated by the interference of the main beam with the light scattered by colloids of 5.2μm and 10.0μm. The images show a mean intensity, modulated by the interference with the speckle pattern. We can notice the different typical size of the speckles. The set of concentric circles can be seen yet: the stray light will be removed with the following step.

Once the images $I_n(\vec{x})$ have been acquired, they are averaged, in order to evaluate $\bar{I}(\vec{x})$ and $\langle \bar{I} \rangle$. By using Eq. (6.7), we evaluate $i(\vec{x})$, the heterodyne signal. Figures 6.4 and 6.5 show the heterodyne signal: since $i(\vec{x})$ is negative, for some points, a constant intensity has been added. The images thus simply represent the ENFS images, cleaned from stray light and optical imprefections.

The heterodyne signal of each image is then elaborated in order to obtain its

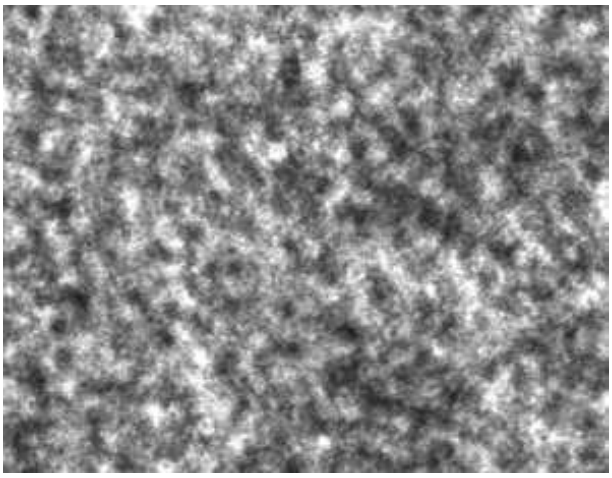

Figure 6.2: ENFS image of a 10.0μm colloid.

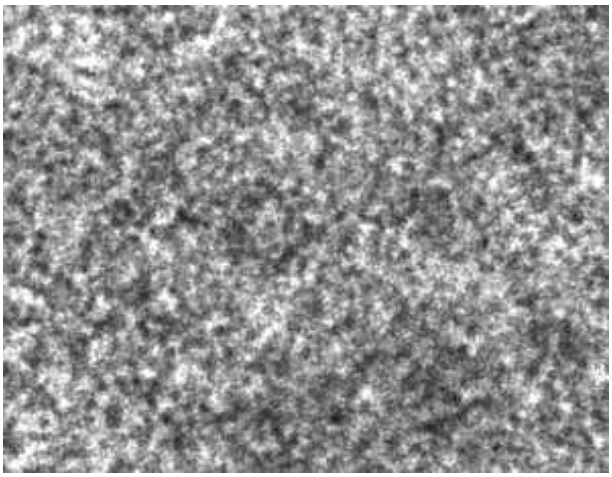

Figure 6.3: ENFS image of a 5.2μm colloid.

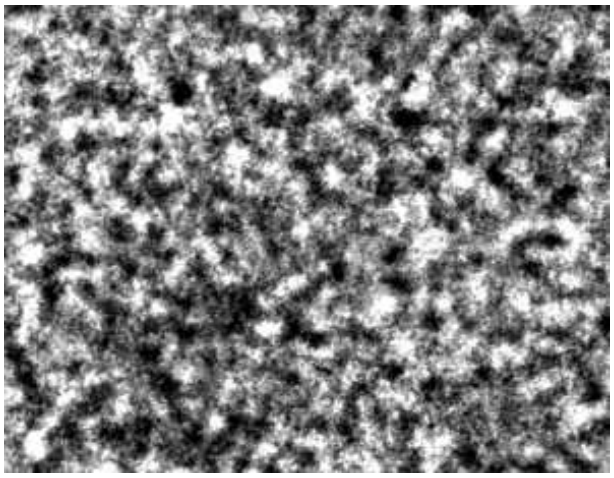

Figure 6.4: ENFS signal of a 10.0μm colloid.

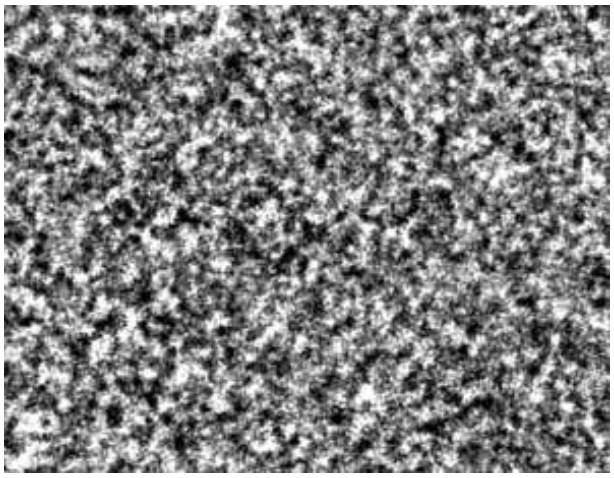

Figure 6.5: ENFS signal of a 5.2μm colloid.

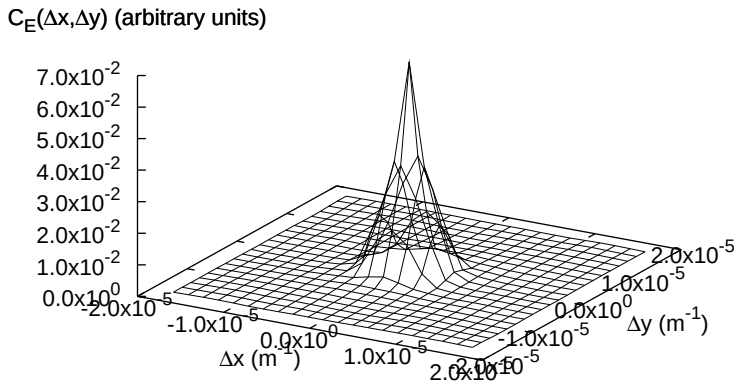

Figure 6.6: ENFS measurement of the field correlation function, for a 5.2μm colloid.

power spectrum. Simple Fourier transforming of the signal would be uncorrect, due to border effects. First of all, we evaluate the correlation function. This operation is quite fast, since we can use a Fast Fourier Transform (FFT) algorithm. An FFT algorithm allows to evaluate the Fourier tranform of an $M \times N$ matrix, with a number of arithmetic operations proportional to $MN \log(MN)$. By using Perceval relation, we can obtain the correlation function by doing an FFT, evaluating the square modulus, and doing an Inverse FFT (IFFT). This only requires a number of operation of the order of $MN \log(MN)$. By scanning every value of Δx, and averaging over every $N \times M$ pixels, the number of operations would be of the order of $(MN)^2$. Using FFT, well known tricks can be used, in order to correct the boundary effects [19]. Figure 6.6 and 6.7 show the correlation functions thus evaluated.

The correlation function evaluated following the above described algorithm suffers from shot and read noise, that is, for the noise due to the CCD light measurement and acquisition systems. Since such a noise is not correlated to the speckle field due to scattered light, the noise correlation function sums to the speckle correlation function. In order to evaluate the noise correlation function, we acquire a set of about one hundred images, before putting the sample in the system. Then, we apply the above described algorithm to the images, and obtain the correlation function of the noise signal. Figure 6.8 shows the correlation function of the noise signal. We can notice a marked peak in 0, quite narrow, representing the correlation inside a row, and a correlation between lines spaced by two pixels, due to interlacing. The correlation function of the noise signal is

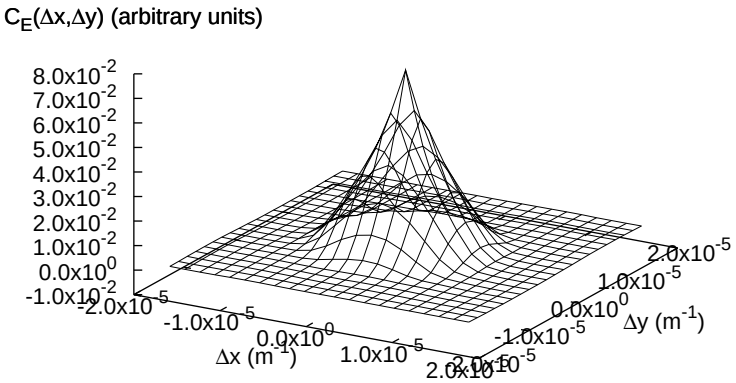

Figure 6.7: ENFS measurement of the field correlation function, for a 10.0μm colloid.

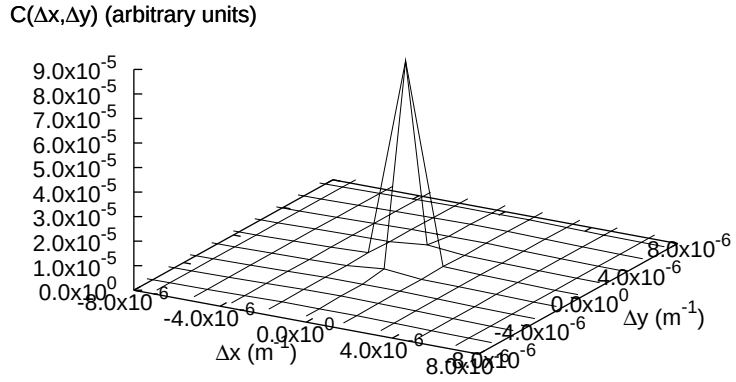

Figure 6.8: Correlation function of the shot and read noise.

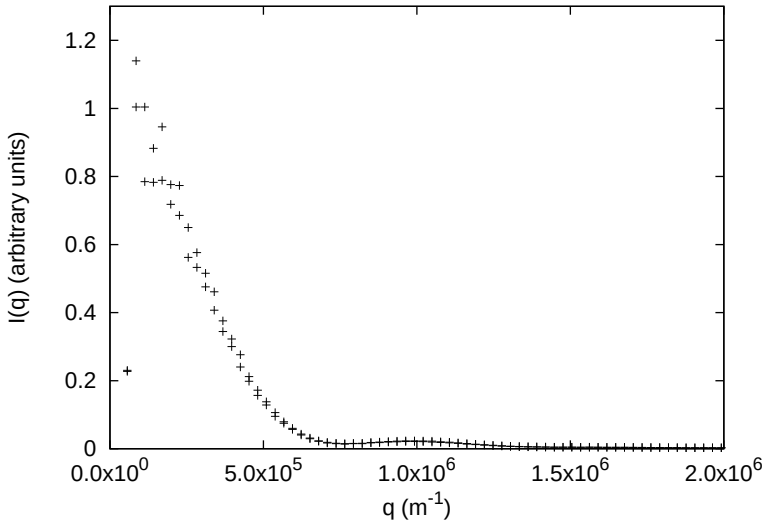

Figure 6.9: ENFS measurement of the scattered intensity of a 10.0μm colloid.

then subtracted by the overall correlation function.

Once the correlation function has been evaluated, through an FFT we obtain the field power spectrum $S_E(q)$. Since our samples are isotropic, we make an angular average of the power spectra, and represent our data as a function of the modulus q of $\vec{q}$. The scattered intensity $I(q)$ is then obtained by using Eq. (3.14), that is, simply relating each value of the power spectra, with wavelength q to a value of $I(Q)$, where the relation $Q(q)$ is given by Eq. (3.13). In Fig. 6.9 and 6.10 we show the measured $I(q)$.

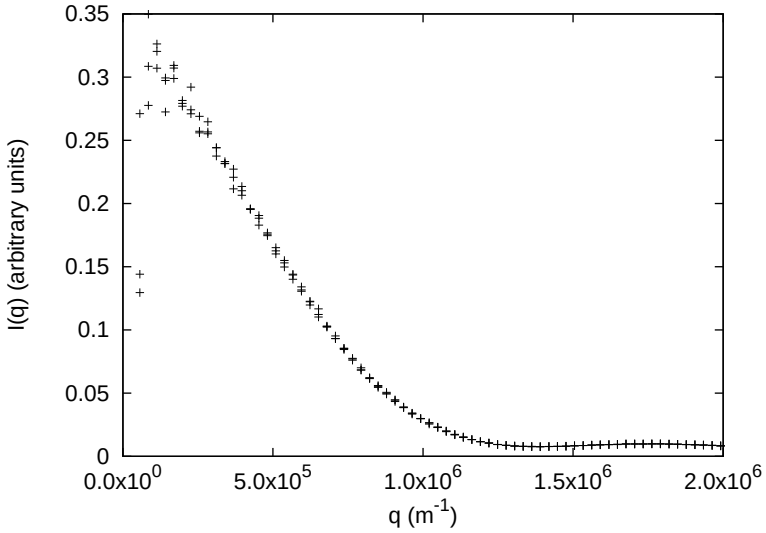

Figure 6.10: ENFS measurement of the scattered intensity of a 5.2μm colloid.

Chapter 7

Performances of ONFS and ENFS on two colloidal samples.

In this chapter we describe ONFS and ENFS measurements we made on two colloids and discuss the results. The optical setup has already been described in Sections 4.7.

7.1 The samples.

The samples we used are monodisperse colloids made of polystyrene spheres suspended in water. In order to avoid sedimentation, we used a mixture of water and heavy water with a weigh fraction of about 0.5. The diameters of the two colloids we used are $5.2\mu\text{m} \pm 0.5\mu\text{m}$ and $10.0\mu\text{m} \pm 0.3\mu\text{m}$, whose polydispersity is negligible. The diameters are quite large, since NFS gives advantages with respect to classical LS for small wavevectors.

The colloids we measured are held in a cell with plane parallel windows. The diameter is about 4cm, since the sample and the beam intensity must be uniform on a length D, where D is given by Eq. (3.64). The thickness is about 2mm. We selected the tickness and the particle concentration in order to have a suitable attenuation of the main beam, about 1%. For ONFS measurements, the thickness of the cell and the volumetric particle density are enough to fulfill Eq. (3.55).

The liquid is held between the two windows by an O-ring; the parallelism between the windows is not critical, nor the optical quality of them. Since the measured scattered light comes from different regions of the sample, we must provide that it is homogeneous. This implies that the thickness must be uniform, but an optical quality allignment is far beyond what is needed.

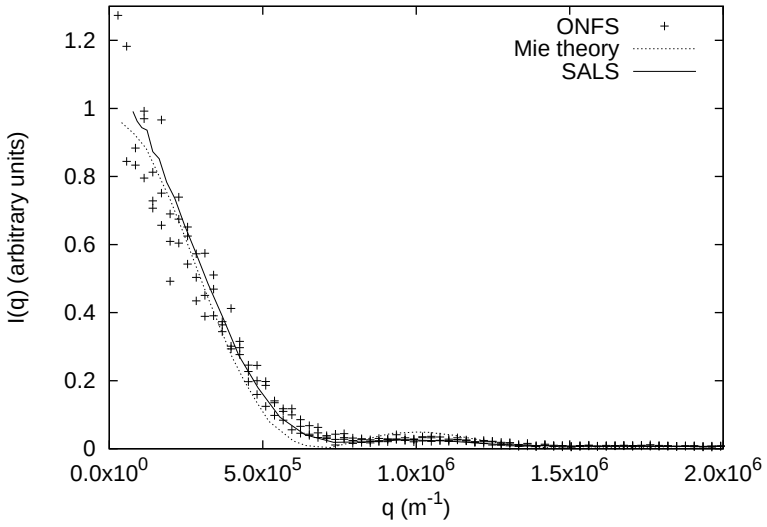

Figure 7.1: ONFS measurement of the 10.0μm colloid. A SALS measurement and a theoretical evaluation based on Mie theory are shown.

7.2 Measurements.

In Fig. 7.1, 7.2 and 7.3 are shown the results of ONFS measurement. The same samples have been analyzed also by a SALS instrument; the results are shown in the graphs.

In Fig. 7.4, 7.5 and 7.6 are shown the results of ENFS measurement. The same samples have been analyzed also by a SALS instrument; the result is shown in the graphs.

Both ONFS and ENFS measurements agree with the SALS measurement, but ONFS gives less accuracy.

7.3 What is the main source of error?

The ONFS data processing is based on Siegert relation; the correlation function is evaluated by Eq. (5.23). First, we average the correlation functions of each image. The error in the evaluation of the intensity correlation decreases as the square root of the number of the samples, and this dependence is intrinsic in the stochastical nature of the technique. Then, we evaluate the field correlation function, by extracting the square root of the difference between the mean intensity correlation and the square mean intensity. Thus we obtain a quantity which converges to the field correlation function as the fourth root of the number of samples.

On the contrary, ENFS gives directly the correlation function without any

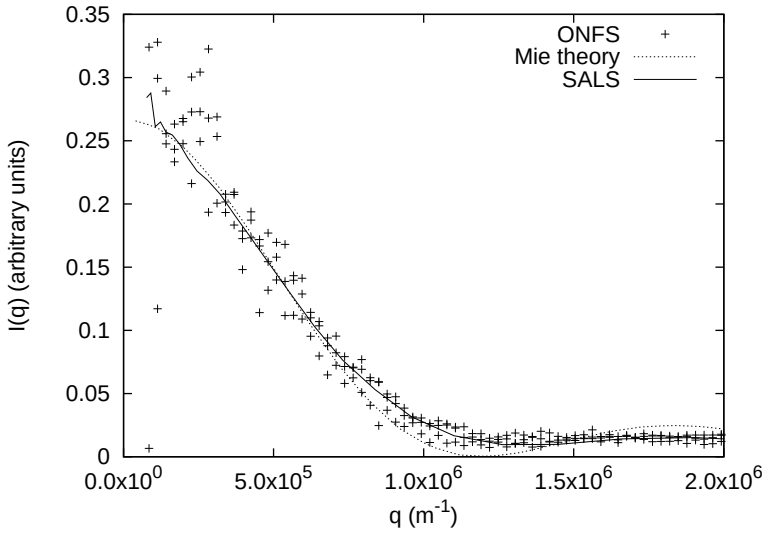

Figure 7.2: ONFS measurement of the 5.2μm colloid. A SALS measurement and a theoretical evaluation based on Mie theory are shown.

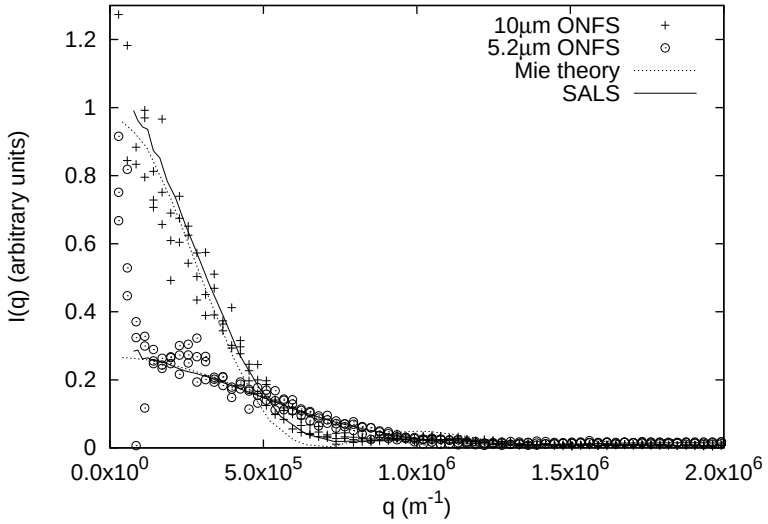

Figure 7.3: ONFS measurements of the two colloids. SALS measurements and theoretical evaluations based on Mie theory are shown.

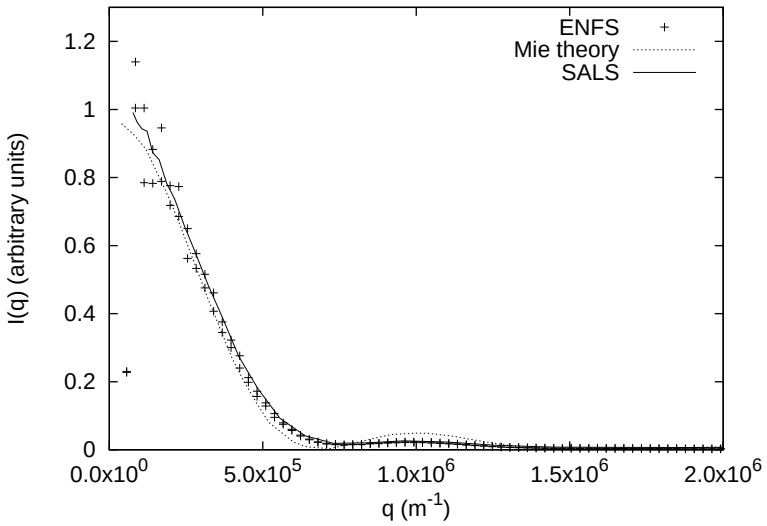

Figure 7.4: ENFS measurement of the 10.0μm colloid. A SALS measurement and a theoretical evaluation based on Mie theory are shown.

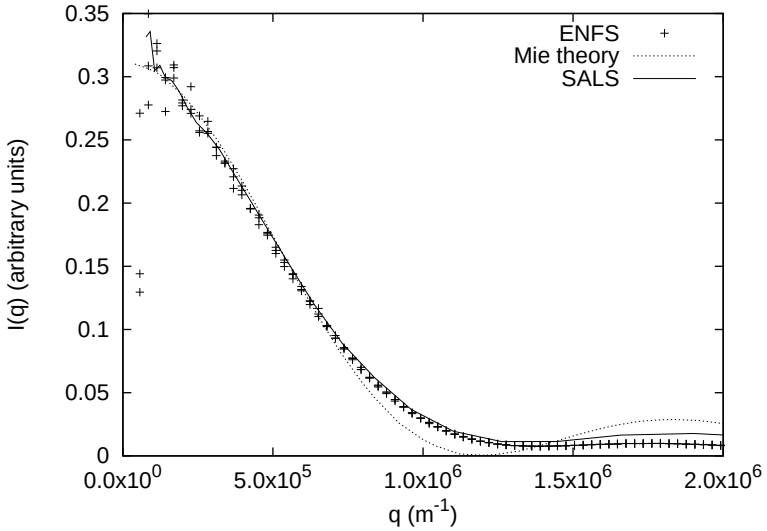

Figure 7.5: ENFS measurement of the 5.2μm colloid. A SALS measurement and a theoretical evaluation based on Mie theory are shown.

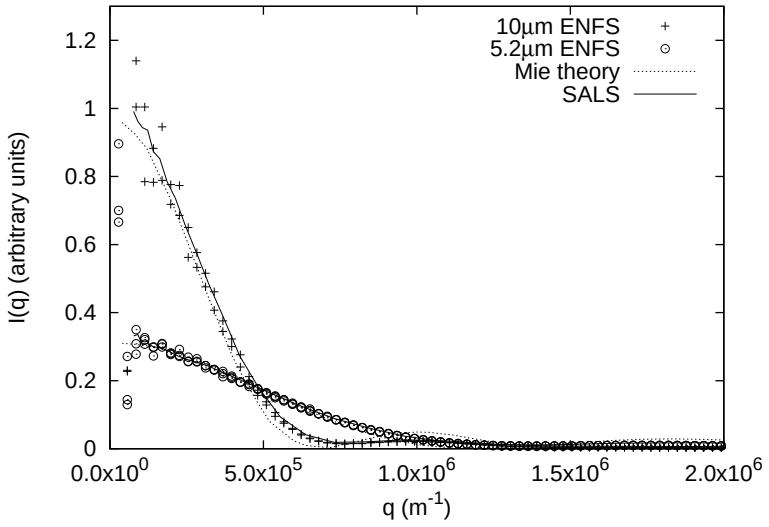

Figure 7.6: ENFS measurements of the two colloids. SALS measurements and theoretical evaluations based on Mie theory are shown.

extraction of square root. We can notice that the plateau of Fig. 6.6 and 6.7 are more plain than in Fig. 5.9 and 5.10. The noise on the plateau is then spread across all the power spectrum when the Fourier transform is performed.

The situation is worst than in dynamic light scattering. The reason is that we are working in two dimensions: in order that the power spectrum can be evaluated, the correlation function must approach 0 faster than $1/r^3$, while in one dimension, it must be faster than $1/r^2$. We can perform an angular mean, but we gain only a term $r^{-1/2}$.

These considerations should explain why ONFS data are much less accurate than ENFS and SALS ones: the problem is the slow statistical convergence as the number of samples increases. In order to test this explanation, we performed some numerical simulations. We used the SALS data to simulate a power spectrum. We created one hundred random fields, with gaussian probability and the given power spectrum. We obtained the homodyne and heterodyne signals, thus creating images similar to the ones we acquired during the experiments. Last, we processed the data with the above described algorithms. The simulations are only affected by the statistics: they are virtually free from any experimental error. In Fig. 7.8 and Fig. 7.7 we present, respectively, the results for the ONFS and ENFS simulations. They look quite similar to the corresponding experimental measurements of Fig. 7.6 and 7.3. This confirms that the main source of error, for our ONFS measurements, is the poor statistical quality of the samples. Since the quality increases as the fourth power of the number of the samples, we cannot make ONFS measurements better than ENFS ones, un-

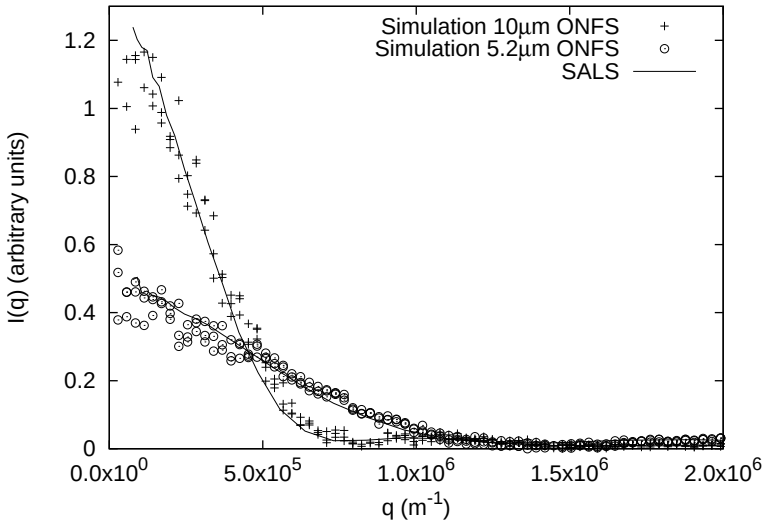

Figure 7.7: Simulations of ONFS measurements of the two colloids. SALS measurements are also shown.

less we process at least one million images: this is, for the moment, impossible.

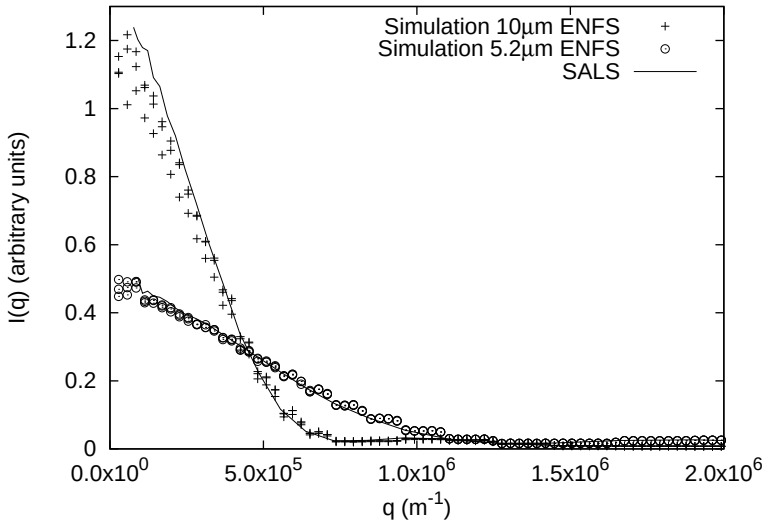

Figure 7.8: Simulations of ENFS measurements of the two colloids. SALS measurements are also shown.

Chapter 8

Particle sizing with ENFS.

One of the most important applications of Light Scattering technique, from the industrial point of view, is particle sizing. Industrial particle sizers generally include some sensors, which measure the scattered intensity $I(q)$, both at small and high angles. Generally, a mechanical system makes the powder or the colloid flow in a cell, so that a good statistical sample can be obtained. An algorithm, based on Mie theory, tries to find the distribution of particle diameters, which best fits the measured scattered intensity.

In order to asses the reliability of ENFS applied to particle sizing, we analyzed some mixtures of two colloids. We prepared two colloidal solution of polystyrene spheres. In order that the density of the solvent matches the density of the colloid, we used a solution of equal volumes of water and heavy water: the colloid was quite stable, and did not sediment evidently over some hours. The diameters of the two colloids are $5.2\mu\text{m} \pm 0.5\mu\text{m}$ and $10.0\mu\text{m} \pm 0.3\mu\text{m}$ (samples A and B). The refraction index of the polystyrene is 1.59, while the solvent has the refraction index of water, 1.33. Then, we prepared three mixtures of them, respectively with volume fractions of 1:1, 1:2, 2:1 of samples A and B. The scattered intensity was measured both with ENFS and a state-of-the-art SALS instrument. The data are presented in Figs. 8.1, 8.2, 8.3, 8.4, 8.5

We define α and β the volume fractions of samples A and B in each mixture; the scattered intensity of the mixture with a given α and β is $I_{\alpha,\beta}(q)$. The scattered intensities $I_{\alpha,\beta}(q)$, obtained for the three mixtures, are compared with the scattered intensities $I_A(q)$ and $I_B(q)$ of the two samples A and B. We evaluate the values of α' and β' for which $I_{\alpha,\beta}(q) \approx \alpha' I_A(q) + \beta' I_B(q)$, by looking for the minima of the mean square deviation:

$$\begin{cases} \alpha' = \dfrac{\sum_q I_{\alpha,\beta}(q) I_A(q) \sum_q I_B^2(q) - \sum_q I_{\alpha,\beta}(q) I_B(q) \sum_q I_A(q) I_B(q)}{\sum_q I_A^2(q) \sum_q I_B^2(q) - \left[\sum_q I_A(q) I_B(q)\right]^2} \\ \beta' = \dfrac{\sum_q I_{\alpha,\beta}(q) I_B(q) \sum_q I_A^2(q) - \sum_q I_{\alpha,\beta}(q) I_A(q) \sum_q I_A(q) I_B(q)}{\sum_q I_A^2(q) \sum_q I_B^2(q) - \left[\sum_q I_A(q) I_B(q)\right]^2} \end{cases} \tag{8.1}$$

The values of α' and β' are the measured colloid concentrations, and must be compared with α and β. Table 8.1 shows the measured values, α' and β',

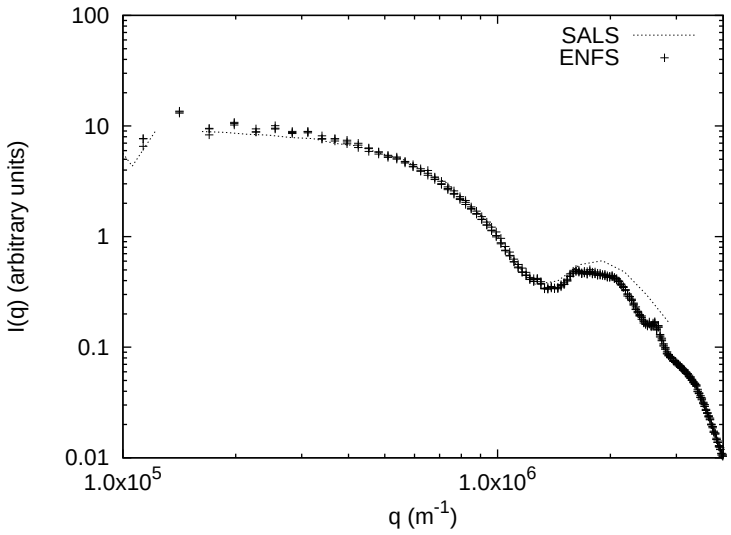

Figure 8.1: Scattered light intensity measurement of a 5.2μm colloid (sample A).

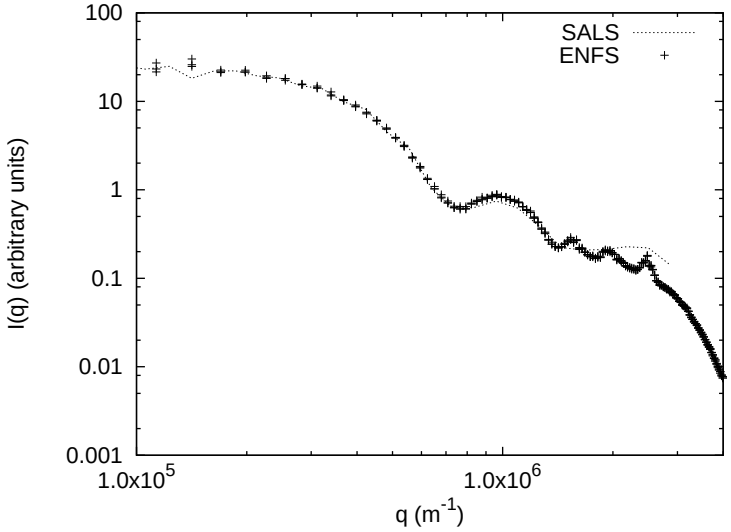

Figure 8.2: Scattered light intensity measurement of a 10.0μm colloid (sample B).

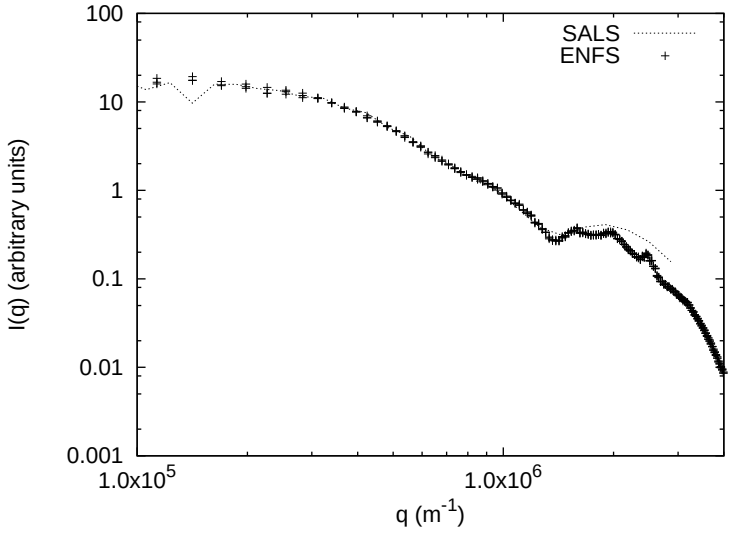

Figure 8.3: Scattered light intensity measurement of a mixture of the two samples. Volume fractions: 1/2 A, 1/2 B

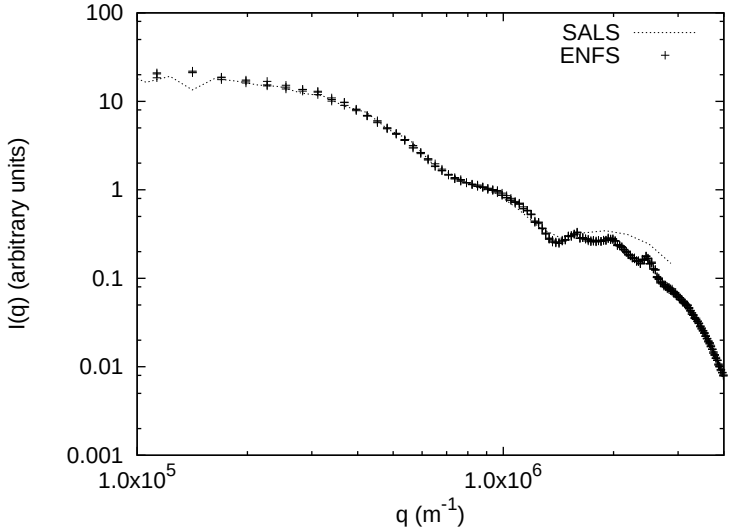

Figure 8.4: Scattered light intensity measurement of a mixture of the two samples. Volume fractions: 1/3 A, 2/3 B

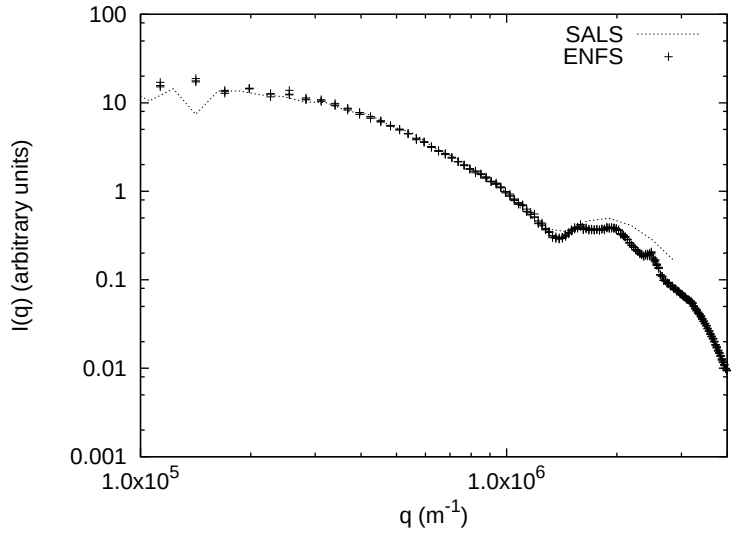

Figure 8.5: Scattered light intensity measurement of a mixture of the two samples. Volume fractions: 2/3 A, 1/3 B

Measured α',β'	Actual α,β
$0.52A, 0.46B$	$1/2A, 1/2B$
$0.69A, 0.32B$	$2/3A, 1/3B$
$0.31A, 0.68B$	$1/3A, 2/3B$

Table 8.1: Measured and actual values of volume concentrations of colloid A and B in the three mixtures.

compared with the actual ones, α and β. The agreement is quite good: this shows that ENFS is suited for particle sizing.

The scattering data has been analyzed by an inversion algorithm based on Mie theory. Mie theory allows to evaluate the scattered intensity $I(q)$ generated by a given diameter distribution $\rho(d)$ of dielectric spheres; the inversion algorithm looks for the distribution $\rho(d)$ which gives the best approximation to the measured $I(q)$. The results are shown in Figs. 8.6 and 8.7. Two peaks are quite evident: they are centered on the diameters of $5\mu m$ and $10\mu m$. The small peak centered around 8μm in the histogram of Sample A corresponds to the scattering of the dymers: the colloid is partially aggregated. The height of the peaks in Fig. 8.7 change accordingly to the fraction of the samples A and B in the mixture.

It should be noticed that ENFS measures the intensity of the scattered beams with reference to the main beam. This allows to evaluate the particle concen-

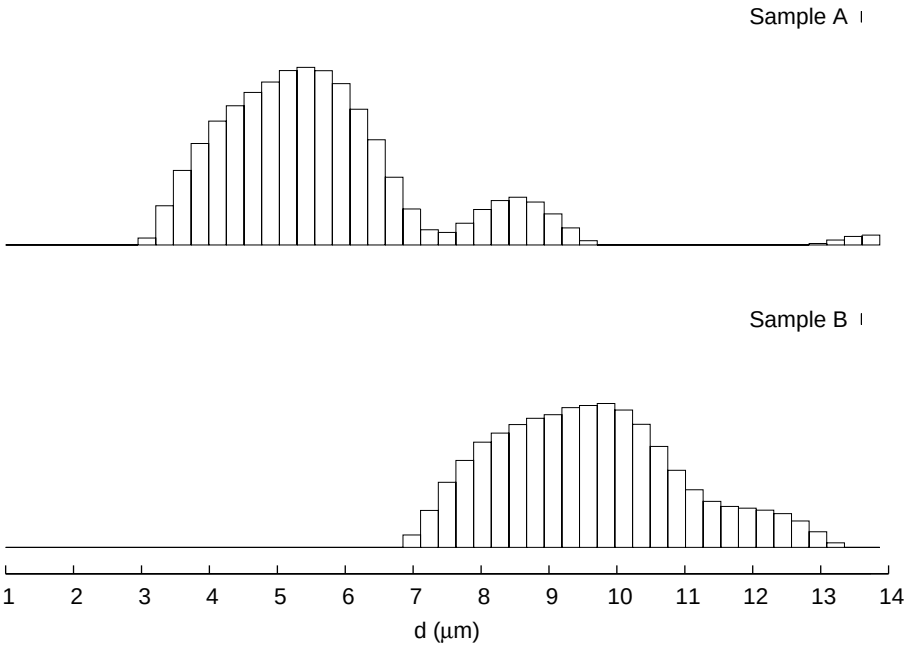

Figure 8.6: Diameter distribution of the two colloidal samples measured by ENFS, obtained by an inversion algorithm based on Mie theory. The height of the bars is proportional to the intensity of light scattered by the particles in the range covered by the horizontal extension of the bar. Sample A is a 5.2μm colloid, and sample B is a 10μm colloid. The two peaks are evident. Sample A shows a small peak centered around 8μm: it corresponds to the scattering of the dymers.

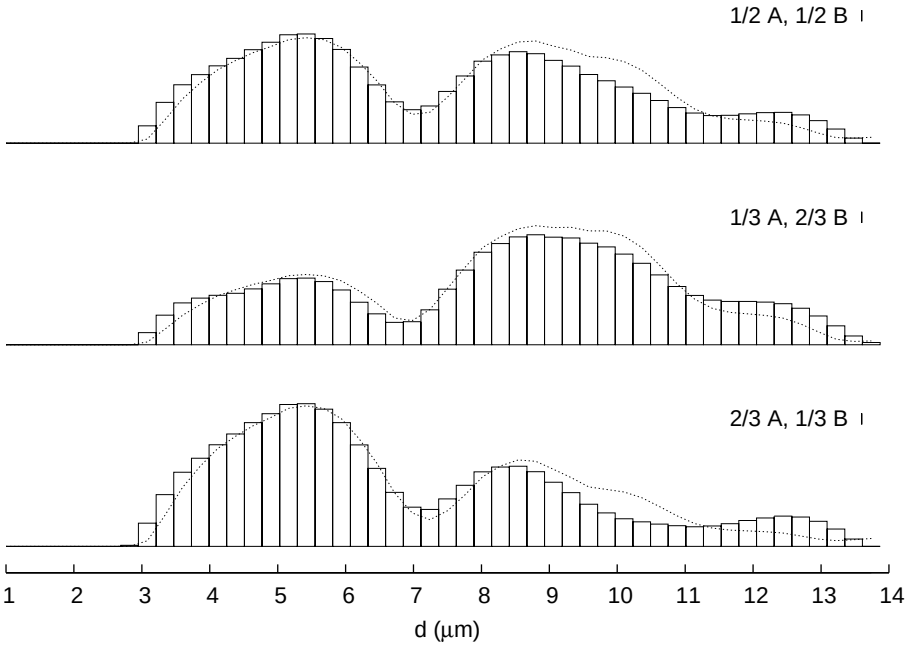

Figure 8.7: Diameter distribution of the mixtures of colloidal samples, measured by ENFS, obtained by an inversion algorithm based on Mie theory. The height of the bars is proportional to the intensity of light scattered by the particles in the range covered by the horizontal extension of the bar. The dotted curves are obtained by combining the values measured for samples A and B, shown in Fig. 8.6 with coefficients given by the volume fractions of the two samples.

tration, and not only the relative concentration of different particles. This is accomplished by using a single sensor; on the contrary, with SALS, the transmitted and the scattered beams must be measured by independent sensors, because the intensities are generally extremely different. This difference comes from the fact that SALS sensors measure the intensity of scattered beams, while ENFS measures the interference of them. For example, consider a sample that generates a single scattered beam, whose intensity is 1/10000 than the transmitted one. For SALS, we need two sensors, one for measuring the scattered beam and one for the transmitted beam, and they require an accurate calibration. A single sensor could be used without calibration, but its dynamic range should cover 4 decades, and in this range it should be quite linear. For ENFS, the interference of the two beams generates a modulation of about 1/100. A single CCD array can easily measure such a modulation.

Chapter 9

Non-equilibrium fluctuations in a free diffusion experiment studied with SNFS

In this chapter, we describe a measurement of the power spectrum of the nonequilibrium fluctuations that arise during a free diffusion experiment. In Sect. 9.1 we discuss the origin of such fluctuations; in Sect. 9.2 we describe the physical system we studied; the results are shown in Sect. 9.3. The optical setup has been already described in Sect. 4.8.

9.1 Nonequilibrium fluctuations in free diffusion processes.

Diffusion is the fundamental mass transfer mechanism in many natural and technological processes. The diffusive transport can be interpreted by the simple molecular random walk model. A more refined description requires the understanding of direct interaction between the diffusing particles and possibly hydrodynamic interactions. Both types of interactions may produce appreciable changes in the magnitude of the effective diffusion coefficient D but, at any extent, diffusion is believed to give rise to an intimate and homogeneous remixing on matter. The general belief is that while the process occurs over quite microscopic distances, nothing peculiar should occur at any other lengthscale, except the molecular one where the random molecular diffusion takes place.

It has been recently shown that, quite unexpectedly, gigant fluctuations are present during the diffusive remixing of two miscible phases of a binary mixture not too far from its critical point [13]. A fluctuating hydrodynamic description

has been developed [20], which indicates that gigant nonequilibrium fluctuations should be present during the diffusive remixing of fluids in general; moreover, it has been shown that the fluctuations can be considered the origin of the whole Fick flow [21].

The presence of the fluctuations has been detected experimentally during the free diffusive remixing occurring in ordinary liquid mixtures and in macromolecular solutions [22, 23]. The measurements concerned an ordinary, low molecular weight liquid mixture, an aqueous solution of a low molecular weight solid, a polymer solution and a protein solution, thus giving evidence that these anomalous fluctuations are a universal feature associated with spontaneous diffusion across a macroscopic gradient.

A free diffusion experiment begins filling a cell with the two liquids, with the denser solution in the lower part to avoid convective instability. The two horizontal layers are initially separated by a fairly sharp meniscus. As soon as the two liquids came into contact, the diffusive remixing begins, and the meniscus repidly becomes smeared. The concentration profile inside the sample, initially a step function as a function of the height z, gradually evolves into an s-shaped function [24], until eventually, after a few days, the concentration becomes uniform throughout the sample.

During the free diffusion process described above, intense fluctuations arise. Their power spectrum $S(\vec{q})$, with $\vec{q}$ in the horizontal direction, is given by:

$$S(q) = S_0 \frac{1}{1 + \left[\frac{q}{q_{RO}}\right]^4}. \tag{9.1}$$

The roll-off wave vector q_{RO} is given by:

$$q_{RO} = \sqrt[4]{\frac{\beta g \nabla c}{\nu D}} \tag{9.2}$$

where g is the gravity acceleration, ν is the kinematic viscosity, D is the diffusion coefficient, and $\beta = \frac{1}{\rho}\frac{\partial \rho}{\partial c}_{p,T}$ is the solutal expansion coefficient, a quantity that increases as increases the mismatching of the two liquids. The gradient ∇c can be assumed roughly connstant in the region between the fluids, where diffusion takes place, and vanishes outside. The sample-dependent prefactor in Eq. (9.1) is given by:

$$S_0 = K_B T \left(\frac{\partial n}{\partial c}\right)^2 \frac{\Delta c}{\rho \beta g} \tag{9.3}$$

where Δc is the total concentration difference across the sample.

The power spectrum $S(q)$ dislpays a q^{-4} power low divergence at large wave vectors, $q \gg q_{RO}$, and a saturation at a constant value at small wave vectors, $q \ll q_{RO}$. The q^{-4} power low is interpreted as the result of of the coupling of velocity fluctuations with concentration fluctuations, while the saturation is due to a stabilizing effect of gravity on long wavelength fluctuations.

Moreover, the roll-off wave vector where the transition between the two regimes occurs gets smaller as $\beta g \nabla c$, and the the low wave vector value of the

power spectrum S_0 is roughly constant as free diffusion takes place, since the concentration near the upper and lower windows of the cell are initially constant.

The nonequilibrium concentration fluctuations are originated from the coupling of velocity fluctuations with concentration fluctuations, due to the presence of a macroscopic concentration gradient. This can be understood by simple naive arguments, discussed in detail in [20] and [25]. Suppose that a small parcel of fluid of linear size a undergoes a velocity fluctuation. This fluctuation will displace the parcel until the viscous drag will stop it in a time given approximately by $\tau_{visc} = a^2/\nu$, ν being the kinematic viscosity. If the displacement of the parcel occurs in a direction parallel to the macroscopic concentration gradient, the parcel will be surrounded by fluid with different concentration. The life time of this concentration fluctuation is $\tau_{diff} = a^2/D$, and is much larger than the viscous time τ_{visc}, as $D \ll \nu$. Thus, in the presence of a macroscopic gradient, the effect of a short living velocity fluctuation is to induce a long lasting concentration fluctuation. Once a concentration fluctuation has been created, two mechanisms may contribute to its relaxation: diffusion and buoyancy. If the spatial extent of the fluctuation is small, then the fluctuation will soon disappear due to diffusion. This mechanism gives rise to the q^{-4} divergence of the static power spectrum at high wavevectors. As the wavevector increases, the velocity fluctuation lives for a shorter time, and can displace the parcel of a smaller amount, and this gives a factor q^{-2}; moreover, the displaced parcel will be dissipated as q^{-2}. However, if the fluctuation is large enough, the buoyancy force acting on it will be able to restore the fluctuation in the layer of fluid having the same density in a time shorter than the diffusive one. This gives rise to the frustration of the q^{-4} divergence at smaller wavevectors.

9.2 The cell.

We have investigated the free diffusion process that takes place when two miscible fluids are brought in contact, the mixing between adjoining regions being kept as little as possible before a measurement sequence. The liquid sample we used was an aqueous solution of glycerol, with a weight fraction of 0.3. It was diffused into pure water. The cell was filled with the two liquids, with the denser solution in the lower part to avoid convective instability. The two horizontal layers are initially separated by a fairly sharp meniscus. As SNFS is an image forming technique, at least for big objects, we were able to thoroughly check the sample for spurious disturbances at the interface before starting collecting data. As soon as the two liquids came into contact, diffusion takes place, and the nonequilibrium fluctuations arise.

The main difficulty is to fill the cell, keeping the interface between the two liquids as regular as possible. We used a Flowing Junction Cylindrical Cell (FJCC), a prototype developed for the study of nonequilibrium fluctuations in microgravity [26]. From Eq. (9.2) we see that the roll off depends on the intensity of g, the gravitational acceleration. As g decreases, gravity acts at increasingly shorter wavevectors, and the divergence of fluctuations at small q

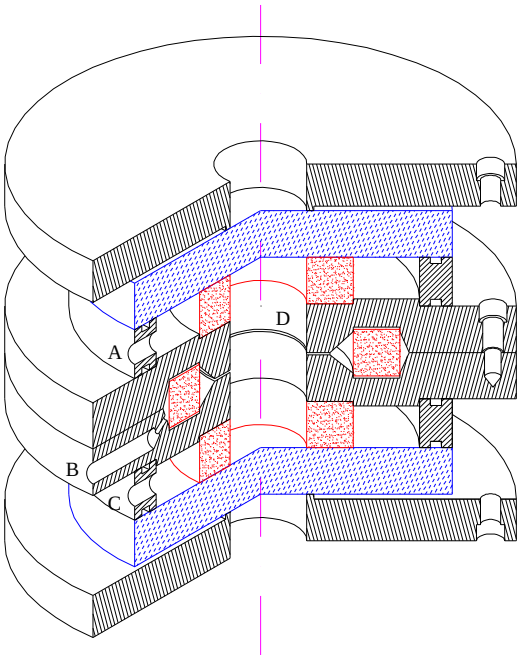

Figure 9.1: The Flowing Junction Cylindrical Cell, developed for measurements of non equilibrium fluctuations in free diffusion experiments in microgravity. The gray parts are made of perspex. The glass windows are blue in the drawing. The two liquids are injected through the holes: water in hole A and a solution of water and glycerol in hole C. They fill, respectively, the upper and the lower part of the cell. The two liquids come into contact in the middle of the cell, and the solution they form flows through the slit D and is extracted from the hole C. The porous rings, red in the drawing, make the flow more regular.

becomes more evident. From Eq. (9.3) we see that the intensity of the power spectrum for small wave vectors increases linearily in $1/g$. This divergence of the intensity of fluctuations on g will be studied in an experiment performed on the Intarnational Space Station. A drawing of the prototype cell is shown in Fig. 9.1; a picture can be seen in Fig. 9.2. Two pipes feed the cell with the two liquids, in the present study water and a solution of water and glycerol, with a small pressure. The liquids enter in two ring-shaped chambers, from which they flow in the cylindrical cell passing throug porous elements. The flow is quite symmetric, due to the presence of the porous rings. The two liquids fill the cell, water on the top and glycerol on the bottom; they come into contact in the middle of the cell, and are pushed out the cell through a circular slit. The outgoing liquid is collected in a third chamber, passes through another porous

Figure 9.2: A picture of the Flowing Junction Cylindrical Cell.

ring, and is collected by a pipe.

The FJCC can be filled also in microgravity, since it is based on the flow of liquids. However, gravity greatly simplifies this task: since the denser fluid is in the lower part of the cell, big fluctuations, created by macroscopic motions, relax due to buoyancy, while small fluctuations disappear quickly due to diffusion.

9.3 Results.

Although low angle light scattering techniques are very suitable to study long range correlated fluids, their sensitivity is hampered by the divergence of stry light at small wave vectors. The data presented in [22, 23] were collected by using the shadowgraph projection technique. Shadowgraphy has traditionally been used to obtain a qualitative mapping of inhomogeneities in the index of refraction. However, very recently the technique has been reintroduced as a powerful quantitative tool to assess the features of long wavelength fluctuations in fluids [15, 16].

The main problem of shadowgraph is the oscillatory behaviour of its transfer function: see Eq. (3.37). The scattering intensities around the zeroes of the transfer function cannot be measured: for example, in Fig. 3 of [22], the values of $S(q)$ are missing for $q \approx 2 \cdot 10^4 \mathrm{m}^{-1}$. Moreove, the region in which the zeroes are too frequent cannot be considered in the data analysis. The overall wavevector range covered about one decade.

We measured the scatterig intensities at different times after the beginning of the diffusion process. The power spectra measured with SNFS are shown in Fig. 9.3. They show the q^{-4} divergence and the saturation for small wavevectors. The roll off wavevector is about $10^4 \mathrm{m}^{-1}$, and is compatible with the value given by Eq. (9.2)

The data cover about two decades in wavevectors: about ten times the range covered with shadowgraph. The quality must be compared with data shown in Fig. 2 of [13], obtained with SALS on a similar, but quite peculiar system: the wavevector range covered by SNFS is slightly more wide. Moreover, it should be noticed that SALS gives no reliable results for the present system, that is for the nonequilibrium fluctuations in the free diffusion of simple fluids, due to stray light, since the scattering is weak and the wavelength associated to the process is quite long. The results we present are the best obtained for such a system up to now.

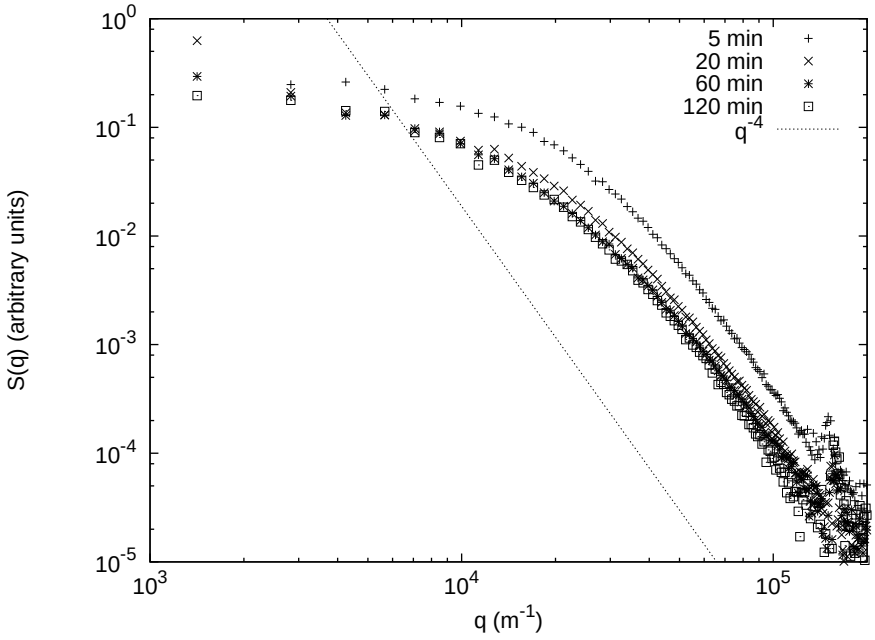

Figure 9.3: Measured power spectrum of non equilibrium fluctuations in the free diffusion process of glycerol in water.

Appendix A

Three dimensional intensity correlation function.

The speckle field generated by a stocastic sample is formed by speckles extending in both the orthogonal and parallel direction with respect to the direction of propagation of the wave. The intensity measured in a plane perpendicular to the direction of propagation varies as the plane is moved; small movements of the plane will give small variations in the intensities. As a matter of facts, the speckles appear and disappear as the plane is moved. This allows us to speack of the three dimensional appearence of the speckles. We will show that the speckles are elongated in the direction of the propagation of the light. If the diamer is α times a wave length λ, their length is α^2 times λ.

In the following sections, we will show that the three dimensional correlation function of the intensity of the scattered light gives more informations than the two dimensional one; in some cases it is possible to determine the sign of the field correlation function, thus determining it completely. Moreover, in analogy to the quadratic relation between the diameter and length of a speckle, the longitudinal frequencies should be related to the square root of the frequencies of the sample: measuring the longitudinal correlations should double the dynamic of the system.

A.1 Evolution equation of the field correlation.

For $q \ll k$, Eq. (3.5) can be approximated by:

$$E_z(\vec{q}) = E_0(\vec{q})\, e^{ikz} e^{-i\frac{q^2}{2k}z} \tag{A.1}$$

In this approximation, neglecting the phase term $\exp(ikz)$, the field follows a Schröedinger equation:

$$i\frac{\partial}{\partial z}E(\vec{x}, z) = -\frac{1}{2k}\nabla^2 E(\vec{x}, z) \tag{A.2}$$

The three dimensional field correlation is defined as follows:

$$C_E\left(\Delta\vec{x},\Delta z\right)=\frac{1}{S}\int_S E\left(\vec{x},z\right)E\left(\vec{x}+\Delta\vec{x},z+\Delta z\right)\mathrm{d}\vec{x}\mathrm{d}z \tag{A.3}$$

In order to obtain an evolution equation for $C\left(\Delta\vec{x},\Delta z\right)$, as Δz increases, we evaluate the first derivative of the correlation function:

$$\frac{\partial}{\partial\Delta z}C_E\left(\Delta\vec{x},\Delta z\right)=\frac{1}{S}\int_S E\left(\vec{x},z\right)\frac{\partial}{\partial\Delta z}E\left(\vec{x}+\Delta\vec{x},z+\Delta z\right)\mathrm{d}\vec{x}\mathrm{d}z \tag{A.4}$$

Using eq. (A.2):

$$\frac{\partial}{\partial\Delta z}C_E\left(\Delta\vec{x},\Delta z\right)=\frac{1}{S}\int_S E\left(\vec{x},z\right)\frac{i}{2k}\nabla^2 E\left(\vec{x}+\Delta\vec{x},z+\Delta z\right)\mathrm{d}\vec{x}\mathrm{d}z \tag{A.5}$$

The operator ∇ acts on the first argument of $E\left(\vec{x},z\right)$, thus it can be considered as acting on $\Delta\vec{x}$:

$$\frac{\partial}{\partial\Delta z}C_E\left(\Delta\vec{x},\Delta z\right)=\frac{i}{2k}\nabla^2_{\Delta\vec{x}}\frac{1}{S}\int_S E\left(\vec{x},z\right)E\left(\vec{x}+\Delta\vec{x},z+\Delta z\right)\mathrm{d}\vec{x}\mathrm{d}z \tag{A.6}$$

This proves that the evolution equation for $\left(\Delta\vec{x},\Delta z\right)$, as Δz increases, is a Schröedinger equation:

$$i\frac{\partial}{\partial\Delta z}C_E\left(\Delta\vec{x},\Delta z\right)=-\frac{1}{2k}\nabla^2 C_E\left(\Delta\vec{x},\Delta z\right) \tag{A.7}$$

This equation can easily be solved in Fourier space:

$$C_E\left(\vec{q},z\right)=C_E\left(\vec{q},z=0\right)e^{-i\frac{q^2 z}{2k}} \tag{A.8}$$

We can now extend eq. (3.65) to the three dimensional case:

$$C_I\left(\Delta\vec{x},\Delta z\right)=\left\langle I\left(\vec{x},z\right)I\left(\vec{x}+\Delta\vec{x},z+\Delta z\right)\right\rangle=\left\langle I\right\rangle^2+\left|C_E\left(\Delta\vec{x},\Delta z\right)\right|^2 \tag{A.9}$$

A.2 Gaussian speckles.

In this section we consider gaussian speckles, and we evaluate their three dimensional correlation function.

Far field speckles are often generated by scattering a gaussian beam, so that the far field speckles have a gaussian correlation function. We consider gaussian speckles in near field, since the case is analitically solvable, and involves some calculations used in quantum mechanics.

The field correlation function of the scattered light, in the plane orthogonal to z, is gaussian:

$$C_E\left(\Delta\vec{x},\Delta z=0\right)=Ce^{-\frac{\Delta\vec{x}^2}{2\sigma^2}}. \tag{A.10}$$

In the Fourier space:

$$C_E\left(\vec{q}, \Delta z = 0\right) = 2\pi\sigma^2 C e^{-\frac{1}{2}\sigma^2 q^2}. \tag{A.11}$$

Using eq. (A.8):

$$C_E\left(\vec{q}, z\right) = 2\pi\sigma^2 C e^{-\frac{1}{2}\sigma^2 q^2 - i\frac{q^2 z}{2k}}. \tag{A.12}$$

Coming back to real space:

$$C_E\left(\vec{x}, z\right) = C\frac{\sigma^2}{\sigma^2 + iz/k} e^{-\frac{x^2}{2\left(\sigma^2 + iz/k\right)}}. \tag{A.13}$$

Now we evaluate the modulus of the field correlation function, the quantity needed in eq. (A.9) to determine the intensity correlation function:

$$\left|C_E\left(\vec{x}, z\right)\right|^2 = C^2\frac{\sigma^4}{\sigma^4 + z^2/k^2} e^{-\frac{x^2\sigma^2}{\sigma^4 + z^2/k^2}}. \tag{A.14}$$

We can now evaluate the intensity correlation function for $\vec{x} = 0$:

$$C_I\left(\vec{x} = 0, z\right) = C^2\left(1 + \frac{\sigma^4}{\sigma^4 + z^2/k^2}\right), \tag{A.15}$$

and for $z = 0$:

$$C_I\left(\vec{x}, z = 0\right) = C^2\left(1 + e^{\frac{x^2}{\sigma^2}}\right). \tag{A.16}$$

While the transverse correlation function follows a gaussian law, the longitudinal one is a Lorentzian, The diameter of the speckles is about σ, while their length is $\sigma^2 k$.

A.3 Determination of the sign of the field correlation function.

The power spectrum, that is $C_E\left(\vec{q}, z = 0\right)$, is real. If the sample is isotropic, it is symetric with respect to the origin, and then the correlation function $C_E\left(\vec{x}, z = 0\right)$ is real. The knowledge of the intensity correlation function with $\Delta z = 0$ gives the absolute value of the field correlation function. The sign of the field correlation function does not affect the intensity correlation function with $\Delta z = 0$, but it can affect its value for $\Delta z \neq 0$.

In figure A.1 and A.2 we see an example of this effect. The figures show the graphs of the square correlation functions. The first is such that $C_E\left(x, \Delta z = 0\right) =$

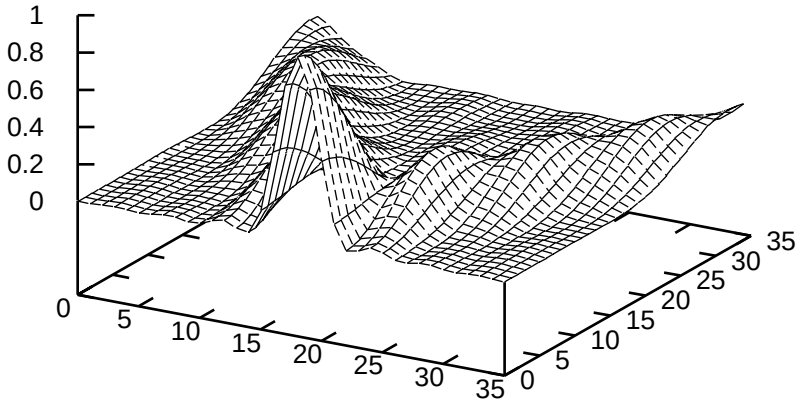

Figure A.1: Comparison between two square correlation functions. $C_E\left(x, \Delta z = 0\right) = \sin\left(x\right)/x$

$\sin\left(x\right)/x$; in the second, the correlation function has the same absolute value, but alwais positive sign, for $\Delta z = 0$. For $\Delta z = 0$ the square correlation functions are equal; their evolution for other values of Δz are different. We can explain this fact considering the evolution of the positive and negative parts of the correlation function. The two parts evolve, and overlap, as Δz increases. The interference of the two parts depends on the initial phase.

The sign of the correlation function is alwais possible, in principle. The presence of errors could limit this possibility.

A.4 Longitudinal correlation.

We want to derive the field correlation along the z axis. We consider its Fourier transform:

$$C_E\left(\Delta\vec{x} = 0, q_z\right) = \frac{1}{\left(2\pi\right)^2}\int C_E\left(\vec{q}, z\right) e^{-iq_z z}\mathrm{d}\vec{q}\mathrm{d}z \tag{A.17}$$

Using eq. (A.8):

$$C_E\left(\Delta\vec{x} = 0, q_z\right) = \frac{1}{\left(2\pi\right)^2}\int C_E\left(\vec{q}, z = 0\right) e^{-i\frac{q^2 z}{2k} - iq_z z}\mathrm{d}\vec{q}\mathrm{d}z \tag{A.18}$$

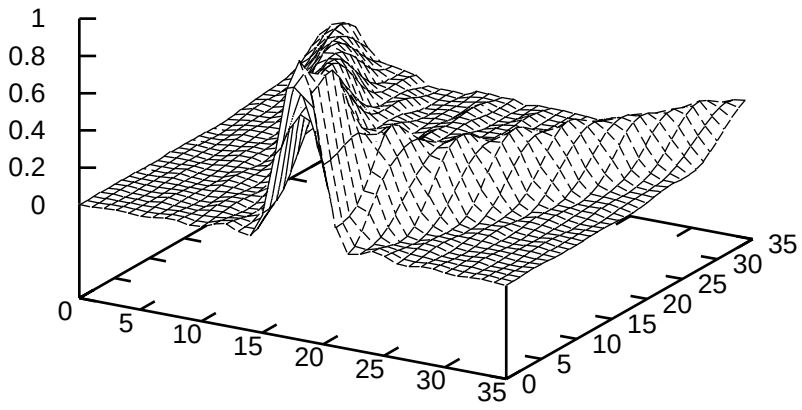

Figure A.2: Comparison between two square correlation functions. $C_E\left(x, \Delta z = 0\right) = \left|\sin\left(x\right)/x\right|$

The integration over z gives a Dirac delta:

$$C_E\left(\Delta\vec{x}=0,q_z\right)=\int C_E\left(\vec{q},z=0\right)\delta\left(\frac{q^2}{2k}+iq_z\right)\mathrm{d}\vec{q} \tag{A.19}$$

In radial coordinates:

$$C_E\left(\Delta\vec{x}=0,q_z\right)=\int C_E\left(q,\varphi,z=0\right)q\delta\left(\frac{q^2}{2k}+iq_z\right)\mathrm{d}q\mathrm{d}\varphi \tag{A.20}$$

If the sample is isotropic:

$$C_E\left(\Delta\vec{x}=0,q_z\right)=2\pi\int C_E\left(q,z=0\right)q\delta\left(\frac{q^2}{2k}+iq_z\right)\mathrm{d}q \tag{A.21}$$

The integral can be evaluated:

$$C_E\left(\Delta\vec{x}=0,q_z\right)=2\pi C_E\left(\sqrt{2kq_z},z=0\right)\sqrt{2kq_z} \tag{A.22}$$

The dynamic of an instrument measuring the longitudinal correlation function is twice that obtained with the transversal one. This facts closely mirrors the quadratic relation between the diameter and the length of the speckles.

Appendix B

Definitions

Fourier transform:

$$f(q) = \int f(x)\, e^{-iqx} \mathrm{d}x \tag{B.1}$$

Inverse Fourier transform:

$$f(x) = \frac{1}{(2\pi)^n} \int f(q)\, e^{iqx} \mathrm{d}q \tag{B.2}$$

Convolution:

$$\begin{array}{l} g(x) = |f(x)|^2 \\ g(q) = \frac{1}{(2\pi)^n} \int f(q')\, f^*(q'-q)\, \mathrm{d}q' \end{array} \tag{B.3}$$

NFS Near Field Scattering
ONFS hOmodyne Near Field Scattering
ENFS hEterodyne Near Field Scattering
SNFS Schlieren-like Near Field Scattering
LS Light Scattering
SALS Small Angle Light Scattering
IFS Intensity Fluctuation Spectroscopy
CCD Charge Coupled Device

Bibliography

[1] Marzio Giglio, Marina Carpineti, and Alberto Vailati. Space intensity correlations in the near field of the scattered light: a direct measurement of the density correlation function $g(r)$. *Phys. Rev. Lett.*, 85:1416, 2000.

[2] Marzio Giglio, Marina Carpineti, Alberto Vailati, and Doriano Brogioli. Near-field intensity correlations of scattered light. *Applied Optics*, 40(24):4036–4040, August 2001.

[3] Marzio Giglio, Alberto Vailati, and Doriano Brogioli. Procedimento per la misurazione di proprietà di particelle immerse in un corpo e relativa apparecchiatura. Italian patent no. TO20001000588, 18/06/2001.

[4] Marzio Giglio, Doriano Brogioli, and Alberto Vailati. Heterodyne technique for the measurement of near field speckles. unpublished.

[5] G. B. Benedek. Polarization, matter and radiation. In *the Jubilee Volume in honor of Alfred Kastler*. Presses Universitaire de France, Paris, 1969.

[6] J. W. Goodman. *Introduction to Fourier Optics*. McGraw-Hill Book Company, New York, 1968.

[7] J. C. Dainty. *Laser Speckle and related phenomena*. Springer-Verlag, Berlin, 1975.

[8] A. Yariv. *Quantum Electronics*. Wiley, New York, 1967.

[9] B. Berne and R. Pecora. *Dynamic Light Scattering*. Wiley, New York, 1974.

[10] R. Hanbury and R. Q. Twiss. *Nature*, 178:1046, 1956.

[11] M. Carpineti, F. Ferri, M. Giglio, E. Paganini, and U. Perini. Salt-induced fast aggregation of polystyrene latex. *Phys. Rev. A*, 42:7347, 1990.

[12] F. Ferri. Use of a charge coupled device camera for low-angle elastic light scattering. *Rev. Sci. Instrum.*, 68:2265, 1997.

[13] Alberto Vailati and Marzio Giglio. Giant fluctuations in diffusion processes. *Nature*, 390:262–265, 1997.

[14] John David Jackson. *Classical electrodynamics*. John Wiley & Sons, London, 1962.

[15] Mingming Wu, Guenter Ahlers, and David S. Cannell. Thermally induced fluctuations below the onset of Rayleigh-Bénard convection. *Phys. Rev. Lett.*, 75(9):1743–1746, August 1995.

[16] John R. de Bruyn, Eberhard Bodenschatz, Stephen W. Morris, Steven P. Trainoff, Yuchou Hu, David S. Cannell, and Guenter Ahlers. Apparatus for the study of Rayleigh-Bénard convection in gases under pressure. *Rev. Sci. Instrum.*, 67(6):2043–2067, June 1996.

[17] Doriano Brogioli. Fluttuazioni giganti in un processo di diffusione in liquidi semplici. Master's thesis, Università degli studi, Milano, May 1998.

[18] Luca Cipelletti and D. A. Weitz. Ultra-low-angle dynamic light scattering with a CCD-camera based on multi-speckle, multi-tau correlator. *Rev. Sci. Instrum.*, 70:3214, 1999.

[19] William H. Press, William T. Vatterling, Saul A. Teukolsky, and Brian P. Flannery. *Numerical recipes*. Cambridge University Press, Cambridge, 1992.

[20] Alberto Vailati and Marzio Giglio. Nonequilibrium fluctuations in time-dependent diffusion processes. *Phys. Rev. E*, 58(4):4361–4371, october 1998.

[21] Doriano Brogioli and Alberto Vailati. Diffusive mass transfer by nonequilibrium fluctuations: Fick's law revisited. *Phys. Rev. E*, 63:012105, 2001.

[22] Doriano Brogioli, Alberto Vailati, and Marzio Giglio. Universal behaviour of nonequilibrium fluctuations in free diffusion processes. *Phys. Rev. E*, 61:R1–R4, january 2000.

[23] Doriano Brogioli, Alberto Vailati, and Marzio Giglio. Giant fluctuations in diffusion processes. *J. Phys.*, 12:39–46, february 2000.

[24] E. L. Cussler. *Mass transfer in fluid systems*. Cambridge Univerity Press, Cambridge, 1997.

[25] D. A. Weitz. Diffusion in a different direction. *Nature*, 390:233, 1997.

[26] Fabrizio Croccolo. Nuova cella flowing junction per lo studio di processi di diffusione libera in microgravità. Master's thesis, Università degli studi, Milano, September 2001.

Contents

List of Figures

List of Tables